CORA Cork Open Research Archive
Cartlann Taighde Oscailte Chorcaí

Title	Tropospheric aerosol detection over Southern Ireland using a backscatter Raman lidar
Authors	McAuliffe, Michael A. P.
Publication date	2012-12
Original Citation	McAuliffe, M. A. P. 2012. Tropospheric aerosol detection over Southern Ireland using a backscatter Raman lidar. PhD Thesis, University College Cork.
Type of publication	Doctoral thesis
Link to publisher's version	http://library.ucc.ie/record=b2070249
Rights	© 2012, Michael A. McAuliffe - http://creativecommons.org/licenses/by-nc-nd/3.0/
Download date	2026-11-15 16:17:34
Item downloaded from	https://hdl.handle.net/10468/996



UCC
University College Cork, Ireland
Coláiste na hOllscoile Corcaigh



Tropospheric aerosol detection over Southern Ireland using a backscatter Raman lidar

A thesis submitted to the
Department of Physics,
National University of Ireland, Cork,

for the degree of
doctor of philosophy

by

M. A. P. McAuliffe

December 2012
Head of the Department: Prof. John McInerney
Supervisor: Dr. Albert. A. Ruth

Table of Contents:

Abstract 5

Acknowledgements 6

Acronyms 7

1. Introduction 8

1.1. Aerosol Influence on the Atmosphere 8

1.1.1. Effects on the Radiation Balance 8

1.1.2. Influence on Air Quality and Visibility 10

1.2. Remote Sensing of Aerosol - Light Detection and Ranging (lidar) 11

1.3. Aerosol Remote Sensing in Ireland 13

1.4. EARLINET (European Aerosol Research lidar Network) 13

1.4.1. ACTRIS (Aerosols, Clouds, and Trace gases Research InfraStructure) Network 15

1.5. Thesis Objectives 16

2. Elastic and Inelastic scattering theory and the lidar equations 17

2.1. Theory of Rayleigh and Raman Scattering 17

2.2. Lidar Retrievals 21

2.2.1. The Klett method 23

2.2.2. The Raman method 24

3. UCLID design and experimental procedures 26

3.1. UCLID setup 26

3.2. Internal lidar checkup procedures 31

3.2.1. Overlap function 31

3.2.2. Telecover Test 35

3.2.3. Rayleigh fit 39

3.2.4. Zero bin measurement 44

4. Results and Discussion 46

4.1. Climatology measurements 46
4.2. Volcanic ash event – Eyjafjallajökull 57
4.3. Saharan dust events 73
5. Conclusion 103
References 105

Declaration of Originality

I hereby declare that this thesis and the work reported herein was composed by and originated entirely from me. Information derived from the published and unpublished work of others has been acknowledged in the text and references are given in the list of sources.

_____

Abstract

Lidar is an optical remote sensing instrument that can measure atmospheric parameters. A Raman lidar instrument (UCLID) was established at University College Cork to contribute to the European lidar network, EARLINET. System performance tests were carried out to ensure strict data quality assurance for submission to the EARLINET database. Procedures include: overlap correction, telecover test, Rayleigh test and zero bin test. Raman backscatter coefficients, extinction coefficients and lidar ratio were measured from April 2010 to May 2011 and February 2012 to June 2012. Statistical analysis of the profiles over these periods provided new information about the typical atmospheric scenarios over Southern Ireland in terms of aerosol load in the lower troposphere, the planetary boundary layer (PBL) height, aerosol optical density (AOD) at 532 nm and lidar ratio values. The arithmetic average of the PBL height was found to be 608 ± 138 m with a median of 615 m, while average AOD at 532 nm for clean marine air masses was 0.119 ± 0.023 and for polluted air masses was 0.170 ± 0.036. The lidar ratio showed a seasonal dependence with lower values found in winter and autumn (20 ± 5 sr) and higher during spring and winter (30 ± 12 sr). Detection of volcanic particles from the eruption of the volcano Eyjafjallajökull in Iceland was measured between 21 April and 7 May 2010. The backscatter coefficient of the ash layer varied between 2.5 $Mm^{-1}sr^{-1}$ and 3.5 $Mm^{-1}sr^{-1}$, and estimation of the AOD at 532 nm was found to be between 0.090 and 0.215. Several aerosol loads due to Saharan dust particles were detected in Spring 2011 and 2012. Lidar ratio of the dust layers were determine to be between 45 and 77 sr and AOD at 532 nm during the dust events range between 0.84 to 0.494.

Acknowledgements

Firstly, I would like to thank my supervisor, Dr Andy Ruth, for giving me the chance to do this project and for all the support, patience and kindness he gave during my graduate studies, as well as his academic advice.

Secondly, thanks to all the staff of the Physics department including past and present members of the Laser Spectroscopy Group that I had the pleasure to work with. I would like to thank the staff of the mechanical workshop, Joe Sheehan, Christy Roche and John Lucey for the many hours of work they offered for the construction of the dome and components used in the lidar.

Thirdly, my family and friends deserve my thanks for their support and help, specifically my wife, Sandra, who was always there for me especially during the writing of this thesis and my parents for their support and encouragement throughout my life.

Fourthly, my sincere thanks go to Ronny Engelmann, Ina Mattis and Ulla Wandinger, from the IfT Leipzig LIDAR group, for their advice and assistances during the development stages of the project. Volker Freudenthaler from Ludwig-Maximilians-University, for listening to my optical design problems and providing constructive feedback. Gelsomina Pappalardo, Istituto di Metodologie per l'Analisi Ambientale, for her encouragement to proactively interact with several EARLINET member sites.

Finally, I wish to acknowledge the support by IRCSET for providing a PhD fellowship under the EMBARK initiative and SFI for funding the establishment of UCLID through research grant 05/RFP/EEB011.

Acronyms

ACTRIS: Aerosols, Clouds, and Trace gases Research InfraStructure Network

AERONET: Aerosol Robotic Network

AOD: Aerosol optical depth

CALIOP: Cloud-Aerosol lidar with Orthogonal Polarization

CALIPSO: Cloud-Aerosol Lidar and Infrared Pathfinder Satellite Observations

CCN: Cloud condensation nuclei

DIAL: Differential-absorption lidar

DREAM: Dust Regional Atmospheric Model

EARLINET: European Aerosol Research Lidar Network

EARLINET-ASOS: European Aerosol Research lidar Network - Advanced Sustainable Observation System

ECMWF: European Centre for Medium-range Weather Forecast

EUSAAR: European Supersites for Atmospheric Aerosol Research

FOV: Field of view

FWHM: Full width at half maximum

GALION: Global Atmosphere Watch Aerosol Lidar Observation Network

GAW: Global Atmosphere Watch

GAWSIS: Global Atmospheric Watch Station Information System

GDAS: Global Data Assimilation System

GOME: Global Ozone Monitoring Experiment

HYSPLIT: Hybrid Single-Particle Lagrangian Integrated Trajectory

IF: Interference filter

MetUN: Met Office Unified

MODIS: Moderate Resolution Imaging Spectroradiometer

NAAPS: Navy Aerosol Analysis and Prediction System

NAME: Numerical Atmospheric-dispersion Modelling Environment

NOGAPS: Navy Operational Global Atmospheric Prediction System

NWP: Numerical Weather Prediction

PBL: Planetary boundary layer

PM: Particulate matter

PMT: Photomultiplier tube

SCIAMACHY: Scanning Imaging Absorption Spectrometer for Atmospheric Chartography

VAAC: Volcanic Ash Advisory Centres

1. Introduction

1.1. Aerosol Influence on the Atmosphere

1.1.1. Effects on the Radiation Balance

Global radiative effects of aerosol on the climate are still largely uncertain. The largest uncertainties in the ability to predict future climate change are associated with uncertainties in the distribution and properties of aerosol and clouds and their interactions, as well as with limitations in how aerosol and clouds are represented in global climate models [1]. Aerosol *scatter* sunlight back into space [2] and (potentially) lead to negative radiative forcing of the earth-atmosphere system counterbalancing the greenhouse effect. Light *absorption by aerosol particles* however warms the atmosphere, which can influence the atmospheric stability and suppress cloud formation [3]. Since water droplets form on aerosol particles [4], changes in aerosol concentration and in their character can alter cloud properties and precipitation leading to an influence on the heat content in the atmosphere. The net impact of these competing cooling and warming effects on the climate depends on the altitude of the aerosol layers. Therefore, vertically resolved measurements of physical and optical properties of particles are of great interest for long term climatological studies. The magnitude of the radiative effect of each aerosol type depends on their compositions, size, distribution, concentration, surface properties and refractive indies [5, 6]. Different aerosol types have distinct properties that influence the Earth's atmosphere differently. Generally one distinguishes between primary and secondary aerosol. Primary aerosol particles are injected into the troposphere, and secondary aerosol particles form within the troposphere [7]. Desert dust and volcanic mineral emission and some types of marine aerosol are examples of primary aerosol. Particles produced by condensation of gases or (photo)chemical radical reactions in the atmosphere result in secondary aerosol particles [7]. Primary aerosol tend to be larger, > 1 µm in diameter and are termed "coarse" particles as opposed to "fine" particles which are dominated by secondary aerosol with typical diameters between 0.1 and 1 µm.

The following aerosol types are subject to lidar observations – their influence on radiative forcing mechanisms will be briefly outlined:

- Marine aerosol
- Soot particles
- Mineral dust
- Sulfate droplets

Marine aerosol are classified as sea salt particles which are produced at the ocean surface by the bursting of air bubbles resulting from entrainment of air induced by wind stress [8]. Upon bursting, these bubbles produce film and jet drops [9] and are most concentrated in the breaking of waves. Sea salt particles are important light scatterers, contributors to cloud condensation nuclei, and provide large surface areas for heterogeneous atmospheric reactions [7]. The longer sea salt particles remain in the atmosphere the more the particles are exposed to SO_2, thus converting the particle to a sulfate [7]. Sea salt aerosol effects on the global climate are generally localised because the particles are large and usually short-lived and thus are transported only over short distances [10]. Direct radiative forcing due to marine aerosol is generally negligible, but the indirect radiative forcing due to cloud formation is estimated to range from -0.3 to -1.8 W/m^2 [11]. The creation of marine particles is relatively insensitive to climate change variables and tends to only affect regions close to the source.

Soot particles represent a type of aerosol generally referred to as black carbon which is commonly based on the agglomeration of polycyclic aromatic hydrocarbon or heterocyclic structures, generated in incomplete combustion processes of fossil fuel in domestic and industrial applications. Due to its significant light absorption properties black carbon is known to cause strong radiative heating of the atmosphere [12]. The wavelength dependent light-scattering efficiency due to soot aerosol particles are dominant at most latitudes, but absorption can dominate at high latitudes, especially over highly reflective snow or ice covered surfaces [10]. Myhre et al. [13] estimate the direct radiative forcing due to soot particles to be +0.16 W/m^2.

Mineral particles describe desert dust produced in arid regions. Mineral dust is a major contributor to the aerosol optical depth and is known to play a role in climate forcing [14-17] through effective scattering of shortwave radiation and absorption of both UV and IR radiation [6]. Typically mineral particle diameters are dependent on the distance travelled from the source, far from the source region, diameters are between 1 to 3 μm and larger sizes (up to several hundred μm) are observed closer to the source [6]. The

hygroscopicity of mineral dust varies over a wide range, depending on the type of mineral coating and the degree of coating with soluble material [18]. The presence of soluble coatings enhances the ability of the mineral dust particles to act as cloud condensation nuclei (CCN). Haywood et al. [11] estimate the radiative forcing due to mineral dust to vary widely from +0.09 to -0.42 W/m^2. The rate of dust emission into the atmosphere is quite sensitive to global changes, since increases of temperature and wind speeds would cause more soil erosion.

Sulfate droplets are used to describe particles of sulfate which form from the combustion of fossil fuels and biomass [19]. Sulfates are one of the main cooling aerosol which have a negative radiative forcing effect [10, 20, 21], and are thought to be the most important scatterers of solar radiation on a global scale. Sulfate particles are hygroscopic materials and cause an increase of CCN leading to more cloud formation [7]. Sulfate can mix with other aerosol species causing their hygroscopic behaviour and optical properties to change [22, 23] and result in diminished cooling. Myhre et al. [13] estimate the direct radiative forcing due to sulfate to be -0.32 W/m^2.

1.1.2. Influence on Air Quality and Visibility

Atmospheric aerosol particles can also profoundly influence the environment. Dust, smoke, and haze locally impair visibility and health in both urban and rural regions. The harmful respiratory health effects of certain mineral and anthropogenic particles are well documented and have led to a standard for air quality control implemented by the European Commission under the Air Quality Directive in 2008 [24]. Under EU Air Quality Directive, particulate matter (PM) is monitored for health effects. PM, also known as particle pollution, is a mixture of very small particles and liquid droplets. There are two standards of PM- PM_{10} and $PM_{2.5}$. PM_{10} refers to coarse particles such as those found near roadways and dusty industries, they are classified as larger than 2.5 μm and smaller than 10 μm in diameter. $PM_{2.5}$ refers to fine particles such as those found in smoke and haze, they are classified as 2.5 μm in diameter and smaller. These particles can be directly emitted from sources such as forest fires, or they can form (photo)chemically from gaseous pollutants in the emission from power plants, industrial factories vehicle exhausts and household burning fossil fuel.

1.2. Remote Sensing of Aerosol - Light Detection and Ranging (lidar)

The vast majority of information on the atmosphere and its dynamic is based on research involving remote sensing technology. Ground based atmospheric remote sensing techniques, such as radar [25], light detection and ranging (lidar) [19], photometers [26], ceilometers [27] are complementing air- and space-borne instruments with multi spectral detection (e.g. NASAs MODIS satellite [28], SCIAMACHY [29, 30] and GOME [31]) to improve our understanding of the global composition and dynamics of the Earth's atmosphere. Lidar has been used to investigate the turbulent processes [32, 33] and the diurnal cycle of the planetary boundary layer [34]. Lidars monitoring PM_{10} and $PM_{2.5}$ have been used within Europe to study the relationship between AOD and $PM_{2.5}$ [35]. Rodríguez et al. [36] and Querol et al. [37] discuss the contribution to PM_{10} levels caused by Saharan dust in Southern and Eastern Spain and the Mediterranean Basin, respectively. Meteorological phenomena such as frontal passages [38] and hurricanes [39] were also studied. A single lidar instrument can only provide atmospheric data locally. It is imperative that individual atmospheric remote sensing stations, be it lidar, photometer or ceilometer stations, collaborate to provide long-term observational data relevant to climate and air quality research on a regional or even global scale. This was one of the primary motivations for the establishment of a Raman lidar system at University College Cork, Ireland [40]. The Cork system (named UCLID) was setup to contribute to the 'European Aerosol Research Lidar Network' (EARLINET see section 1.3) [41-43] and was recently included as a regional station to GAWSIS (Global Atmospheric Watch Station Information System). An event like the eruption of Eyjafjallajökull in Spring 2010 illustrates the benefit of a large scale network for the provision of near real-time information on major atmospheric events [41-44].

Generally one can distinguish between five basic lidar techniques that have been developed to monitor different properties of the atmosphere. They are elastic-backscatter lidar [45], Raman lidar [46], Doppler lidar [32], differential-absorption lidar (DIAL) [47] and fluorescence (resonance) lidar [48]. Doppler lidar is used to measure the radial velocity of particles [49, 50] and molecules [51, 52] carried by the wind to determine the component of the wind velocity within the line of sight of the lidar [53]. The most common application of Doppler lidar is to deliver statistics on wind speeds over a large area for potential sites for the establishment of wind turbine farms. The

DIAL technique is used for high sensitivity detection of atmospheric gases such as SO_2, NO_2, NH_3, HCl, CO and Hg [54-56]. The technique involves emitting light at two wavelengths into the atmosphere. At one wavelength the light is absorbed by the gas species of interest as opposed to the light at the second wavelength [19]. The differential absorption between the two lightwaves (detected through the emission from the gas species of interest) is a measure of the concentration of that species as a function of altitude. Water vapour and temperature can also be observed using the DIAL technique [57]. Resonance fluorescence lidar is used to study the upper mesosphere / lower thermosphere at altitudes between 80 and 110 km [48]. The laser wavelength is tuned to the resonance absorption wavelength of a specific molecular species whose resonant backscatter cross section is measured in order to determine its density. Elastic backscatter lidars were used to investigate cloud and aerosol layers since the early 1960s [58]. It has only been due to the establishment of networks of aerosol lidars such as the Asian Dust Network [59] and EARLINET [41-43], that quantitative studies of atmospheric aerosol properties can be performed on a larger scale.

Air-borne [60] and space-borne [61] lidar systems allow regional and global monitoring of atmospheric constituents, specifically, CALIPSO measurements [62, 63] will be used to support arguments presented in this thesis. CALIPSO was launched in April 2006. The satellite is in a non geostationary orbit at an altitude of 705 km a.s.l. The satellite has a 16 day repeat cycle using a sun synchronous polar orbit (i.e. the satellite precesses about the earth at the same rate that the earth orbits the sun). The primary instrument on board the CALIPSO satellite is a Cloud-Aerosol lidar with Orthogonal Polarization (CALIOP) utilizing a Nd:YAG laser with a frequency doubler which produces linearly polarized light at 1064 nm and 532 nm. The instrument provides global polarization lidar measurements. In addition to CALIOP, CALIPSO carries two passive sensors, (i) a wide field CCD visible sensor and (ii) an infrared imaging radiometer. Both devices provide a view of the atmosphere surrounding the lidar field of view [61]. The CALIPSO mission provides information on the following aspects of Earth's atmosphere:

- Statistics on the vertical structure of clouds around the globe
- Statistics on the geographic and vertical distribution of aerosol particles around the globe

- Detection of clouds in the upper troposphere and Polar Stratospheric Clouds
- Improvement of observationally-based estimates of direct and indirect aerosol radiative forcing
- Improved characterization of surface longwave radiative fluxes and atmospheric heating rates

Validation of CALIPSO measurements via intercomparison with independent ground based lidar systems is essential to the production of high quality data. During analysis of profiles measured at Cork, CALIPSO datasets and air mass backward trajectories are used to confirm the presence of various aerosol loads above Cork.

1.3. Aerosol Remote Sensing in Ireland

Since the Cork station is located close to the Celtic Sea and giving the strong westerly winds coming from over the Atlantic Ocean, the aerosol load over Cork is expect to be maritime by nature. Since the Cork site in Ireland is located in the Atlantic at the western edge of Europe (51.53N 8.29W), the station is of obvious geographic importance as an entrance point of air masses into continental Europe from a north-westerly direction. This offers a unique opportunity to establish a lidar station, where clean conditions are expected but also the possibility of other aerosol being transported from continental Europe, North Africa and North America. The clean maritime conditions would provide a strong baseline for intercomparison with other station which would experience high aerosol loads on a regular basis. The remit of the Cork station is to actively contribute to EARLINET and the 'Aerosols, Clouds, and Trace gases Research InfraStructure Network' (ACTRIS, http://www.actris.net) through the collection of quantitative data on the vertical aerosol profiles over Southern Ireland.

1.4. EARLINET (European Aerosol Research lidar Network)

EARLINET was established in February 2000 as a research project supported by the European Commission under the Fifth Framework Programme (FP5). It then evolved into EARLINET-ASOS (European Aerosol Research lidar Network - Advanced Sustainable Observation System) which comprised Integrated Activities implemented as Coordination Action within the Sixth Framework Programme (FP6). It is currently supported by the EU FP7 project ACTRIS (section 1.4.1). More information on the EARLINET consortium of 27 lidar stations across Europe can be found at

www.EARLINET.org. Figure 1 shows the active EARLINET station in Europe. The objectives of EARLINET are to:

- provide a long-term, continuous and readily available database of aerosol measurements.
- establish microphysical and radiative properties for aerosol research and characterization.
- validate satellite retrievals and synergies with other databases.
- validate and improve models that predict the future state of the atmosphere.



Figure 1. Map of existing EARLINET lidar stations in Europe.

On 7 January 2008, an application from the Cork research group to join the network had been accepted. EARLINET hold two annual workshops to meet and discuss the current activities such as lidar intercomparisons, upcoming measurement campaigns and quality assurance issues. In addition, support is given on testing individual experimental lidar parameters, error analysis, comparative results of different components and hardware testing. One of the requirements for EARLINET is to submit regular backscatter profiles taken at specific times during the week, weather permitting. The network also works with CALIPSO by performing direct intercomparison of ground based lidar measurements and satellite measurements [64-66].

EARLINET also collaborates with AERONET [67] (AErosol RObotic NETwork), a network of ground-based remote sensing aerosol networks established by NASA. AERONET provide aerosol optical depth (AOD) values using sun photometers by measuring the extinction of direct beam spectral solar radiation. Comparisons of AOD between EALINET and AERONET ensure each network observe similar values [68-70]. EARLINET is also part of the Global Atmosphere Watch (GAW) aerosol program. The GAW programme is a partnership of 80 countries which provide information on the chemical composition of the atmosphere, its natural and anthropogenic change and help improve the understanding of interactions between the atmosphere, the ocean and the biosphere. The strategic plans can be found in [71]. GAW main areas of study are greenhouse gases, ozone, UV, aerosol particles, selected reactive gases, and precipitation chemistry.

1.4.1. ACTRIS (Aerosols, Clouds, and Trace gases Research InfraStructure) Network

ACTRIS was established in April 2011 as a research project supported by the European Commission under the Seventh Framework Programme (FP7). ACTRIS combines three existing research infrastructures EUSAAR, EARLINET, CLOUDNET, and a new trace gas network component into a single coordinated framework. On 3 February 2012 an application from the Cork research group to become an affiliated member of the network had been accepted.

The main objectives of ACTRIS are:

- To provide long-term observational data on aerosol particles, clouds and trace gases and to substantially increase the number of high-quality data relevant to climate and air quality research on the regional scale produced with standardized or comparable procedures throughout the network.
- To provide a coordinated framework to support transnational access to European advanced infrastructures for atmospheric research strengthening high-quality collaboration in and outside the EU.
- To develop new integration tools to fully exploit the use of multiple atmospheric techniques at ground-based stations, in particular for the calibration / validation / integration of satellite sensors and for the improvement of the parameterizations used in global and regional scale climate and air quality models.

1.5. Thesis Objectives

The scope of this PhD work was to establish the Cork site as an integral part of the network(s) EARLINET (ACTRIS and GALION (Global Atmosphere Watch Aerosol Lidar Observation Network)) and to contribute backscatter and extinction profiles to their respective databases. To ensure UCLID is at the same standard as other EARLINET stations, internal performance test were developed and performed regularly and submitted for approval to network operatives (Section 3). Since many of the lidar stations within EARLINET are situated on the European continent the Cork site was expected to provide important information on the vertical distribution of aerosol particles in a marine atmosphere. For the first time in Ireland the seasonal effects on the planetary boundary layer, AOD and vertical aerosol backscatter profiles will also be studied over the periods, April 2010 to May 2011 and February 2012 to June 2012.

Section 2.1 covers the theory on Rayleigh and Raman backscattering. Section 2.2 explains the lidar retrieval principles. In section 3.1 the lidar setup and the design parameters of UCLID will be discussed. Section 3.2 explains the internal lidar checkup procedures, required by EARLINET, which ensure high quality of the data submitted to the database. In Section 4, the results of measurements made with UCLID will be discussed; section 4.1 describes the statistical analysis of climatology parameters (planetary boundary layer height, lidar ratio, aerosol optical depth and backscatter profiles), section 4.2 outlines aerosol detection after the eruption of Eyjafjallajökull in Spring 2010, and section 4.3 discusses the aerosol profiles during the occurrence of dust events in the troposphere over Cork. Section 5 contains the conclusions.

2. Elastic and Inelastic scattering theory and the Lidar equations

2.1. Theory of Rayleigh and Raman Scattering

Scattering of light is based on the time dependence of the dipole moment that is induced in a molecule by the electric field of a light wave interacting with the charges in a molecule. The induced dipole moment depends on the state of motion of the molecule, generally either vibrational or rotational. Scattering is inherently weak and can be elastic or inelastic. If no state change occurs in the molecule during the interaction with the light wave the frequency (ν_0) of the scattered photon remains constant. This case is called elastic (Rayleigh) scattering. If a molecule experiences a vibrational or rotational state changes during the scattering (ineleastic scattering case), the frequency (ν_0) of the scattered photon is shifted to either higher or lower frequencies (ν_R) by an amount $|\Delta\nu_0|$. If the molecule absorbs energy the frequency of the scattered photon is decreased, (red shift), $\nu_R = \nu_0 - |\Delta\nu_0|$, this process is called Stokes Raman scattering. If the molecule transfers energy to the scattered photon, the frequency of the scattered photon is increased (blue-shift), $\nu_R = \nu_0 + |\Delta\nu_0|$, this process is called anti-Stokes Raman scattering [72].

In Raman scattering the shift in the frequency is due to a change of the polarizability in the vibrational and/or rotational state of the molecule by which the photon is scattered. The cross section for Rayleigh and Raman scattering in N_2 is inherently weak (Rayleigh scattering cross section of N_2 at 532 nm is 5.1×10^{-31} m [73] and the pure Vibrational Raman scattering cross section is 2.90×10^{-34} m [74]) In Raman Lidar the inelastic Stokes scattering by N_2 in the vibrational ground state manifold is measured [75-78], however it is not rotationally resolved. Upon excitation at 532 nm, the molecule N_2, emits 607 nm which is the detection wavelength. Figure 2 shows a schematic diagram for the vibrational levels involved for N_2.

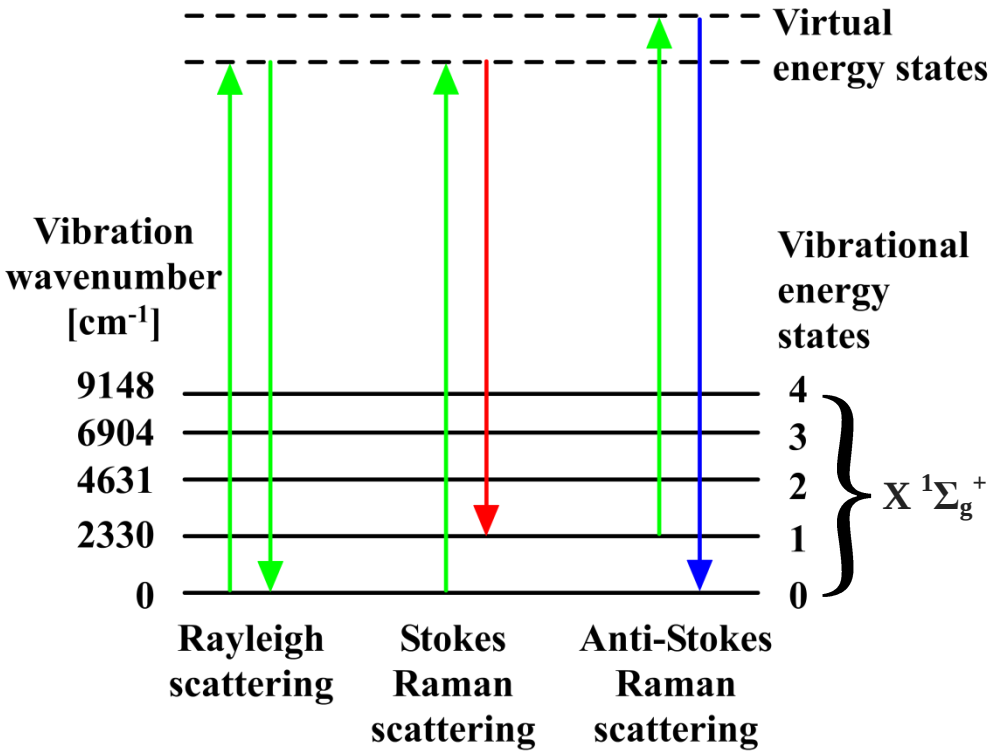


Figure 2. Vibration energy level diagram showing the states involved in Raman scattering for N_2. The different possibilities for light scattering are: Rayleigh scattering (no exchange of energy so the incident and emitted photons have the same energy), Stokes scattering (the atom or molecule absorbs energy and the emitted photon has less energy than the absorbed photon - blue shifted) and anti-Stokes scattering (the atom or molecule loses energy and the emitted photon has more energy than the absorbed photon - red shifted). The values for the vibration wavenumber consider anharmonicity correction for each vibrational energy state shown for N_2 [79, 80].

Theoretical considerations

The shift in the frequency is due to a change in the vibrational and/or rotational state of the molecule from which the photon is scattered. If a molecule experiences a vibrational or rotational state changes, the frequency (ν_0) of the scattered photon is shifted to either longer or shorter frequency (ν_R), photon is shifted by an amount $|\Delta\nu_0|$. If the molecule absorbs energy the frequency of the scattered photon is decreased, (red shift), $\nu_R = \nu_0 - |\Delta\nu_0|$, this process is called Stokes Raman scattering. If the molecule transferred energy to the scattered photon, the frequency of the scattered photon is increased (blue-shift), $\nu_R = \nu_0 + |\Delta\nu_0|$, this process is called anti-Stokes Raman scattering [72].

An incoming electromagnetic field (E) acting on a molecule is characterised by a frequency (ν_0) and amplitude (E_0):

$$E(t) = E_0 \cos 2\pi v_0 \, t \tag{1}$$

The electromagnetic field (E) induces an electrical dipole (μ) in the molecule, N_2, which is giving by:

$$\mu_{\text{ind}}(t) = \alpha \cdot E(t) \tag{2}$$

Where α is the polarizability of the molecule, a measure of the change in the molecules electron distribution in response to the applied electric field, E. If the electromagnetic field, eq (1), is combined with the induced dipole, eq (2), the dipole then oscillates with respect to the field:

$$\mu_{\text{ind}}(t) = \alpha \cdot E_0 \cos 2\pi v_0 \, t \tag{3}$$

According to eq (3) the induced dipole oscillates at a frequency v_0 and thus gives rise to the Rayleigh line. The vibrational Raman effect arises from the change of α with the vibrational normal co-ordinate, q. For simple harmonic vibrations the ground state of the molecule can be described as follows:

$$q(t) = q_0 \cos 2\pi v_{vib} t \tag{4}$$

Where v_{vib} is the resonance frequency of the vibrating molecule and q_0 is the normal coordinate. Assuming that the variation in electronic polarizability remains small during the vibrational motion of the molecule, the electronic polarizability near the equilibrium position of the atoms constituting the molecule (q = 0) can be expanded in a Taylor series:

$$\alpha = \alpha(q) = \alpha_0 + \left(\frac{\delta\alpha}{\delta\alpha}\right)_{q=0} \cdot q + \frac{1}{2}\left(\frac{\delta^2\alpha}{\delta^2 q}\right)_{q=0} \cdot q^2 + \cdots \tag{5}$$

This expression for electronic polarizability, eq (5), can be inserted into eq (3) to give the dipole oscillation:

$$\mu_{\text{ind}} = \left[\alpha_0 + \left(\frac{\delta\alpha}{\delta\alpha}\right)_{q=0} \cdot q_0 \cos 2\pi v_{vib} t\right] \cdot E_0 \cos 2\pi v_0 \, t \tag{6}$$

Expanding the term, eq (6) can be rewritten as:

$$\mu_{\text{ind}} = \alpha_0 E_0 \cos 2\pi v_0\, t + \frac{1}{2}\left(\frac{\delta\alpha}{\delta\alpha}\right)_{q=0} q_0 E_0 \cos[2\pi(v_0 - v_{vib})t] + \frac{1}{2}\left(\frac{\delta\alpha}{\delta\alpha}\right)_{q=0} q_0 E_0 \cos[2\pi(v_0 + v_{vib})t] \quad (7)$$

In eq (7), the first term corresponds to elastic scattering, the second term refers to the red shifted Stokes Raman scattering and third term refers to the blue shifted anti-Stokes Raman scattering.

The calculation for homonulear diatomic molecules, in this case N_2, can be approximated with the model of a freely rotating harmonic oscillator to give the energy of the vibrational levels (eq (8)):

$$E_{vib,v} = hc2\pi v_{vib}(\mathrm{v} + 1/2), \qquad \mathrm{v} = 0, 1, 2, \ldots, \quad (8)$$

Where:

$E_{vib,v}$ . . . energy of vibrational levels [J]

h . . . Planck's constant [J s]

$\boldsymbol{c}$ . . . speed of light in a vaccum [m s^{-1}]

v_{vib} . . . vibrational frequency of the molecule [c m^{-1}]

v . . . vibrational quantum number [1]

Eq (8) is an expression for the energy of the vibrational levels of N_2, to calculate the frequency shift after eq (8), the selection rule for vibrational transitions needs to be considered, eq (9).

$$\Delta\mathrm{v} = 0, \pm 1 \quad (9)$$

Δv is the difference of the vibrational quantum numbers of the final and the initial vibrational states. Figure 3 illustrates the transitions between the vibrational energy levels of a diatomic molecule. The transitions with $\Delta\mathrm{v} = 0$ correspond to Rayleigh scattering. The transitions with $\Delta\mathrm{v} = -1$ give anti-Stokes vibrational lines, and those with $\Delta\mathrm{v} = +1$ give Stoke vibrational lines.

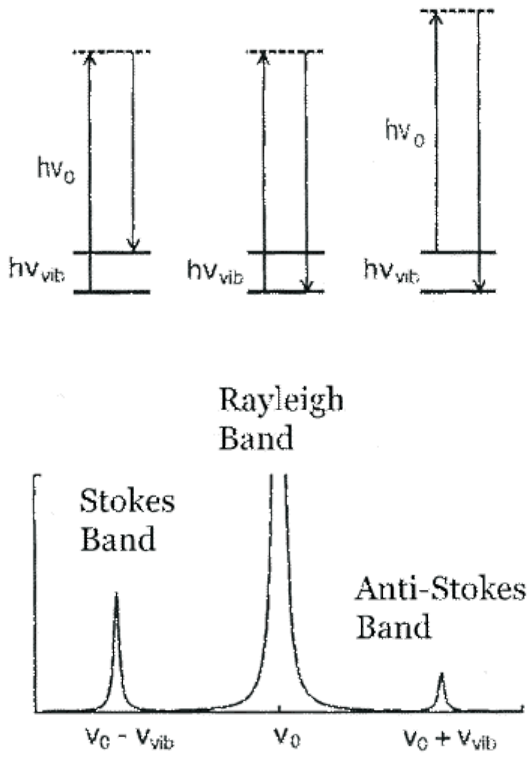


Figure 3. Vibrational Raman Spectrum. Transition where $\Delta v = 0$, produces Rayleigh lines, while transition where $\Delta v = -1$ or $\Delta v = +1$, produces anti-Stokes vibration lines and Stoke vibration lines. Image source from Long, D. A. [80].

2.2. Lidar Retrievals

The optical power returned to the lidar from height z contains both elastic and inelastic components. The elastically backscattered component of the received signal is calculated using the following equation:

$$P(\lambda_0, z) = P_0 \frac{c\tau}{2} \frac{A_T \eta_{\lambda_0} O(z)}{z^2} \beta(\lambda, z) \exp\left[-2 \int_0^z \alpha(\lambda_0, \xi) d\xi\right] \quad (10)$$

Where:

$P(\lambda_0, z)$ . . . detected power at wavelength λ_0 from distance z [W],

$\beta(\lambda, z)$ . . . elastic backscatter coefficient at z [m^{-1} sr^{-1}],

$\alpha(\lambda_0, z)$ . . . extinction coefficient at wavelength λ_0 between z and $z+dz$ [m^{-1}],

P_0 . . . average emitted power of the laser [W],

τ . . . laser pulse duration [s],

c . . . speed of light [m s^{-1}],

A_T . . . area of the telescope [m^2],

η_{λ_0}. . . transmission of the receiver optics at wavelength λ_0 [$0 < \xi < 1$],

$O(z)$ . . . overlap function between emitter and receiver field of view [0< ξ <1].

The overlap function, $O(z)$, describes the overlap between the laser beam (transmitter field of view) and the telescope's (receiver) field of view. The elastic backscattering and extinction coefficient both consist of a molecular (mol) and an aerosol (aer) term, such that, $\beta(\lambda, z) = \beta_{mol}(\lambda, z) + \beta_{aer}(\lambda, z)$ and $\alpha(\lambda_0, z) = \alpha_{mol}(\lambda_0, z) + \alpha_{aer}(\lambda_0, z)$. The two molecular terms, $\beta_{mol}(\lambda, z)$ and $\alpha_{mol}(\lambda_0, z)$, can be calculated using pressure and temperature profiles obtained by radio sounding or from the model of a standard atmosphere [81]. While the two aerosol terms cannot be calculated in the same fashion, they remain unknown in the elastic backscatter equation. If the lidar system possesses a second channel, $\alpha_{mol}(\lambda_0, z)$ can be determined by additionally detecting the Raman backscattering of atmospheric N_2. The optical power of the backscatter signal at the Raman wavelength (λ_R) is calculated from [46]:

$$P(\lambda_R, z) = P_0 \frac{c\tau}{2} \frac{A_T \eta_{\lambda_R} O(z)}{z^2} N_R(z) \frac{d\sigma(\pi, \lambda_0)}{d\Omega} \exp\left[-\int_0^z [\alpha(\lambda_0, \xi) + \alpha(\lambda_R, \xi)] d\xi\right] \quad (11)$$

Where:

$P(\lambda_R, z)$. . . detected power at wavelength λ_R from distance z [W],

$\alpha(\lambda_R, z)$. . . extinction coefficient at the Raman shifted wavelength λ_R between z and $z+dz$ [m^{-1}],

η_{λ_R}. . . transmission of the receiver optics at Raman wavelength λ_R [0< ξ <1],

$\frac{d\sigma(\pi,\lambda_0)}{d\Omega}$. . . Raman backscattering cross section [$m^2 sr^{-1}$],

$N_R(z)$ . . . molecular number density of the Raman scattering gas [m^{-3}].

The exponential function in eq (11) contains two terms: the first corresponds to the atmospheric transmission of the laser light in its propagation direction (into the atmosphere) up to an altitude z, while the second represents the transmission of the inelastically back scattered light through the atmosphere in the opposite direction. The Raman backscatter coefficient, $N_R(z) \frac{d\sigma(\pi,\lambda_0)}{d\Omega}$ depends solely on the number density of the Raman scattering gas (N_2 in this case) and the backscattering cross-section. Aerosol backscatter $\beta_{aer}(\lambda_R, z)$ does not occur in eq (11), thus the only unknown is $\alpha_{aer}(\lambda_0, z)$. Eqs (10) and (11) can be solved using several different methods. Measurements performed during this project were solved using two methods: i) the Klett method (applied for day-

time measurements), that is, by solving a Bernoulli equation that is derived from the basic lidar eq (10) [82] and ii) the Raman method (applied for evening and night-time measurements) [46].

2.2.1. The Klett method

The Klett method, suffers from the fact that two physical quantities, the aerosol backscatter (β_{aer}) and aerosol extinction coefficient (α_{aer}), must be determined from only one measured lidar signal. This is not possible without assumptions about the relation between the two and an estimate of a boundary or reference value of the aerosol extinction. This data is usually not available and causes large uncertainties in the aerosol extinction coefficients. The collected backscatter signal must be sufficiently averaged to reduce the statistical error before the retrieval procedures are performed to give the backscatter coefficient. The solution for the Klett method can be written as follows [83]:

$$\beta_{\text{aer}}(\lambda_0, z) = -\beta_{\text{mol}}(\lambda_0, z) + \frac{A(z, z_0)}{B(z_0, \lambda_0) - 2S_{\text{aer}}(\lambda_0)\int_z^{z_0} A(\xi_0, \xi, \lambda_0)d\xi} \tag{12}$$

with

$$A(z_0, z, \lambda_0) = P(z, \lambda_0)z^2 \exp\left[-2(S_{\text{aer}}(\lambda_0) - S_{\text{mol}})\int_z^{z_0} \beta_{\text{mol}}(\xi, \lambda_0)d\xi\right] \tag{13}$$

and

$$B(z_0, \lambda_0) = \frac{P(x, \lambda_0){z_0}^2}{\beta_{\text{aer}}(z_0, \lambda_0) + \beta_{\text{mol}}(z_0, \lambda_0)} \tag{14}$$

Here, $S_{mol}=8\pi/3$ sr is the molecular extinction divided by the molecular (Rayleigh) backscatter. The unknown parameters in eqs (12) and (13) are $S_{aer}(\lambda_0)$, the so called lidar ratio (aerosol extinction over aerosol backscatter), and the aerosol backscatter coefficient, $\beta_{aer}(z_0,\lambda_0)$, at a specific distance z_0, which is usually estimated (typically $z_0 >$ 30 km). Large errors due to the assumption of the lidar ratio can easily exceed 20% [84]. Since the lidar system has two channels it is possible to obtain a value for the lidar ratio from the measurement of the inelastic backscatter. Based on this so-called Raman method, the error on the Klett solution as per eqs (12) to (14) can thus be strongly reduced.

2.2.2. The Raman method

The extinction coefficient can be calculated from the inelastic backscatter signal in eq (11) assuming the overlap function to be unity:

$$\alpha_{\text{aer}}(\lambda_0, z) = \frac{\frac{\mathrm{d}}{\mathrm{dz}}\left[\ln \frac{N(z)}{z^2 P_{\lambda_{\text{R}}}(z)}\right] - \alpha_{\text{mol}}(\lambda_0, z) - \alpha_{\text{mol}}(\lambda_0, z)}{\left(1 + \frac{\lambda_0}{\lambda_{\text{R}}}\right)^{\text{å}}} \tag{15}$$

The Angström exponent, å, describes the wavelength dependence of the aerosol extinction coefficient $\alpha_{\text{aer}}(\lambda_0, z)/\alpha_{\text{aer}}(\lambda_{\text{R}}, z) = (\lambda_{\text{R}}/\lambda_0)^{\text{å}}$. The value of å is often set to one. With the knowledge of $\alpha_{\text{aer}}(\lambda_0, z)$ in eq (15) the backscatter coefficient can be calculated using both types of information (elastic and Raman signal). The aerosol backscatter coefficient, $\beta_{\text{aer}}(\lambda_0, z)$, can be derived by the ratio of the elastic ($P(\lambda_0)$) and inelastic ($P(\lambda_{\text{R}})$) signals at z and at a reference height z_0, specifically $\left[P(\lambda_0, z)P(\lambda_{\text{R}}, z_0)/P(\lambda_0, z_0)P(\lambda_{\text{R}}, z)\right]$. Re-arranging eqs (10) and (11) and introducing the above ratio yields:

$$\begin{aligned}
&\beta_{\text{aer}}(\lambda_0, z) \\
&= -\beta_{\text{mol}}(\lambda_0, z) + [\beta_{\text{aer}}(\lambda_0, z_0) + \beta_{\text{mol}}(\lambda_0, z_0)] \frac{O(\lambda_{\text{R}}, z)}{O(\lambda_0, z)} \\
&\times \frac{P(\lambda_{\text{R}}, z_0)P(\lambda_0, z)\beta_{\text{mol}}(\lambda_0, z)}{P(\lambda_0, z_0)P(\lambda_{\text{R}}, z)\beta_{\text{mol}}(\lambda_0, z_0)} \frac{\exp\left\{-\int_{z_0}^{z}[\alpha_{\text{aer}}(\lambda_R, \xi) + \alpha_{\text{mol}}(\lambda_{\text{R}}, \xi)]\, d\xi\right\}}{\exp\left\{-\int_{z_0}^{z}[\alpha_{\text{aer}}(\lambda_0, \xi) + \alpha_{\text{mol}}(\lambda_0, \xi)]\, d\xi\right\}}
\end{aligned} \tag{16}$$

A reference height z_0 is chosen so that $\beta_{\text{mol}}(\lambda_0, z) \gg \beta_{\text{aer}}(\lambda_0, z)$, this occurs in the upper atmosphere where aerosol concentration is insignificant; z_0 can be determined using the Raman signal profile. Eq (16) is valid only when there is a complete overlap $O(\lambda_0, \lambda_{\text{R}}, z) = 1$. The overlap can be determined experimentally using the technique described in [85]. The experimentally determined overlap function permits data at altitudes below the complete overlap to show interaction of low planetary boundary layers with additional layers compared to a simulated overlap and have a smaller error associated with the values where the overlap is not complete. Determining the experimental overlap function is only possible when a Raman backscatter signal is

available from a measurement. In section 3 the (typical) overlap function of UCLID will be discussed.

3. UCLID design and experimental procedures

3.1. UCLID setup

A lidar system can be divided into three different components as seen in Figure 4. The three components are:

(A) Transmitter unit

(B) Receiver unit

(C) Data Processing unit

The transmitter unit (A) consists of the laser and beam expander, which are connected by beam steering optics. The power of the laser is also measured in the transmitter unit before the beam expander.

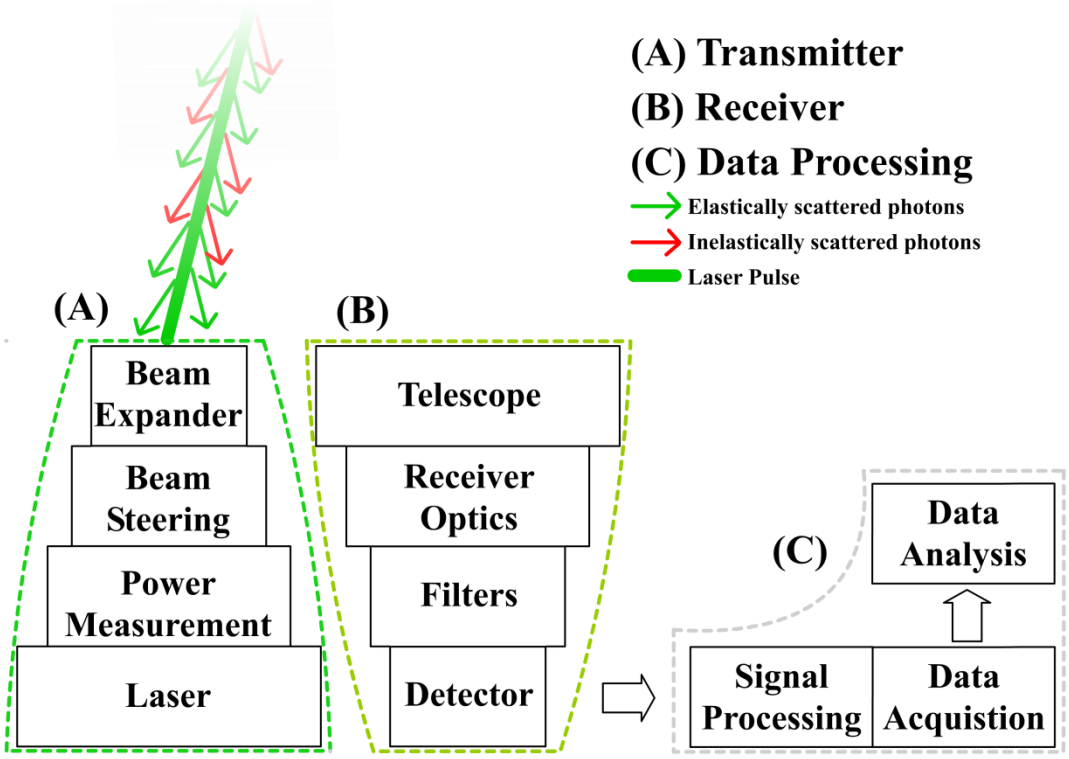


Figure 4. Components of a lidar system. The transmitter unit (A) contains the Nd:YAG laser and a Galilean telescope (used for the beam expansion) connected by beam steering optics. The receiver unit (B) contains a Newtonian reflector telescope, a beamsplitter and two narrow band filters and two detectors. The Data processing unit (C) has three functions: signal processing, data acquisition (2 input transient card) and data analysis.

The UCLID system, which was originally used until 2007 (see [86]), was upgraded by August 2010. Table 1 summarizes the "old" and "new" lidar specification. The main changes (highlighted in Table 1) were laser and detector replacements as well as the

addition of a camera to improve the overlap function stability (see Figure 5). A comparison of the detectors is made in

Table 2 and Table 3.

Table 1. Comparison of "new" and "old" UCLID system specifications. Changed specifications are highlighted.

	Old system	**New system**
Laser		
Type	Nd:YAG	Nd:YAG
Operating Wavelength	532.08 nm	532.08 nm
Repetition Frequency	10 Hz	20 Hz
Power	30-50 mJ	150 mJ
Transmitter Optics		
Telescope	Refractor (Galilean)	Refractor (Galilean)
Main Lens	120 mm, f /5	120 mm, f /5
Beam expansion factor	12	12
Beam divergence	0.25 mrad	0.04 mrad
Receiver Optics		
Geometry	Newtonian	Newtonian
Main Mirror	300 mm, f /5	300 mm, f /5
Field of view	0.73 mrad	0.73 mrad
Filter 1	532.08 +/- 1.0 nm	532.08 +/- 1.0nm
Filter 2	607.4 +/- 0.34	607.4 +/- 0.34
Detectors		
Channel 1 (red sensitive)	Thorn EMI 9659 QB	Hamamatsu H7422P-40
Channel 2 (green sensitive)	Philips XP2212B	Hamamatsu H5783P
Data acquisition system		
Type	2 input multi-channel scalar	2 input multi-channel scalar
Max count rate	300 MHz	300 MHz
Min time-bin width	200 ns	200 ns

Table 2. PMT characteristics comparison of the Philips XP2212B PMT to the upgraded H5783P PMT.

	Philips XP2212B	**H5783P**
Typical Gain	1×10^{7}	1×10^{6}
Window material	Lime glass	Borosilicate Glass
Cathode material	Bi-alkaline	Bi-alkaline
Effective cathode diameter	44 mm	8 mm
Sensitive region of spectrum [nm]	300-500	300-550
Dark counts at 5 mV discriminator threshold (21 ^{0}C)	75000 s^{-1}	80 s^{-1}
Dark counts at 20 mV discriminator threshold (21 ^{0}C)	20000 s^{-1}	0 s^{-1}
FWHM	14.9 ns	2-3 ns

Table 3. PMT characteristics comparison of the Thorn EMI 9659 QB PMT to the upgraded H7422P-40 PMT.

	Thorn EMI 9659 QB	**H7422P-40**
Typical Gain	7×10^{6}	1.8×10^{6}
Window material	Fused Silica	Borosilicate Glass
Cathode material	S20 (tri-alkaline)	GaAsP
Effective cathode diameter	45 mm	5 mm
Sensitive region of spectrum [nm]	350-750	400-700
Dark counts at 5 mV discriminator threshold (21 ^{0}C)	500-1100 s^{-1}	500 s^{-1}
Dark counts at 20 mV discriminator threshold (21 ^{0}C)	60-300 s^{-1}	0 s^{-1}
FWHM	11.9 ns	2-3 ns

Figure 5 shows a schematic diagram of the transmitter, receiver and detection optics of UCLID. The components of this figure will be explained in the same sequence in which the lidar system is operated. The light source is a frequency doubled Nd:YAG laser (Quantel, BRILL/IR-20) operating at 20 Hz repetition rate with a beam diameter at the laser's exit aperture of 6 mm. The energy per pulse of ~150 mJ is measured with a

power meter (PM, Gentec QE 12) before and after each measurement. The beam expander used is a refractor telescope of Galilean design, which expands the laser beam by a factor of 12. An elliptical mirror (λ/8) is used to control the overlap between the transmitter and receiver.

The receiver telescope is of Newtonian design, with a 0.3 m parabolic mirror and a focal length of 1.5 m. The field stop can be varied from 0.9 mm to 5.0 mm allowing the field of view (FOV) of the telescope to range from 0.60 mrad to 3.33 mrad, respectively. A typical field stop size would be 1.1 mm which provides a field of view of 0.73 mrad. The field stop size of 1.1 mm provides enough light suppression in the near field of the telescope but allows for a complete overlap at a low altitude. A collimating lens creates a parallel beam with a diameter of 30 mm. A 45^{o} beam splitter (BS1) with a reflectivity of $R = 0.99$ at 532.1 nm and a transmission of $T = 0.97$ at 607.4 nm separates the elastic backscatter from the inelastic N_2 backscatter.

The *inelastic backscatter* passes through an optional neutral density filter, whose optical density can be chosen between 0 and 5 (in steps of 0.5) to avoid saturation of the signal under different atmospheric conditions. The light is further spectrally filtered by a narrow bandwidth interference filter (IF, Barr Ltd.) at 607.40 ± 0.34 nm. Off resonance the filter suppresses straylight by more than a factor of 10^{-8} with a max transmission of 11.4% at 607 nm. Finally a positive lens (L) causes the light to converge towards the 20 mm^2 cathode of a coolable GaAsP photomultiplier (PMT, Hamamatsu H7422) with a rise time of 1 ns and a FWHM of ca. 8 ns at a gain of 2×10^6. All measurements were performed by photon counting.

The *elastic backscatter* signal can be monitored with a high resolution CMOS camera which is used to view an image of the field stop for alignment purposes. The overlap between the expanded laser beam and the telescope's FOV can be monitored using the trigger software of the camera. Approximately half of the elastic backscatter is guided through a neutral density filter and a narrow band IF filter with the centre wavelength at 532.08 ± 1.00 nm for normal incidence with a max transmission of 35.5% at 532 nm. The elastic backscatter is detected by a bialkali PMT (Hamamatsu, H5783-P) with a cathode area of ca. 50 mm^2, a pulse rise time of 0.8 ns and FWHM of 8 ns.

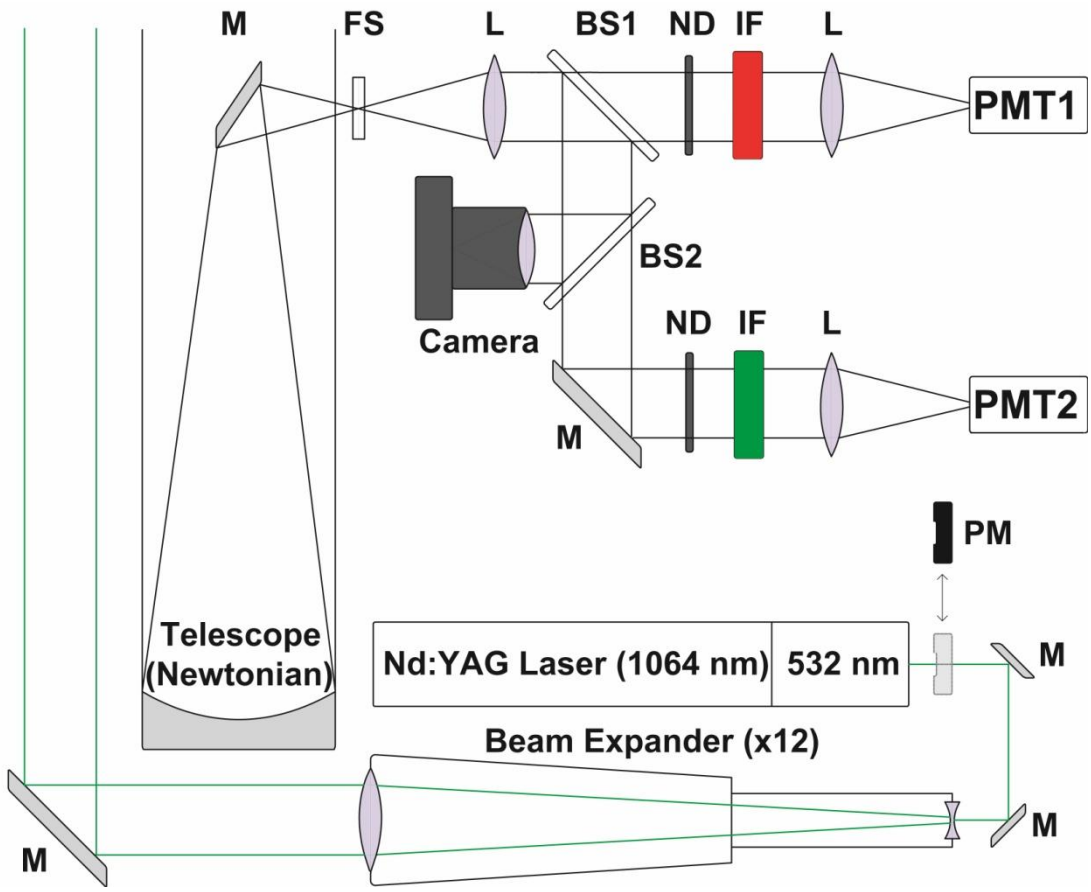


Figure 5. Schematic of the Raman lidar system UCLID: PM: power meter (optional) FS: Field stop (diameter 0.9 – 5 mm, corresponding FOV 0.6 – 3.33 mrad). L: Lens collimates the beam onto a wavelength dependent beam splitter, BS1. Dichroic beam splitter BS2: Beam splitter (50:50 ratio). Camera: CMOS is used to monitor the overlap of the system. ND: neutral density filters (optional), IF: Interference filter (narrow band), PMT: photomultiplier tube (1: cooled GaAsP, 2: uncooled bialkali).

Data acquisition is performed using a dual input photon counter card (Fast Comtec P7882). The bin width of the transient recorder is 200 ns which correspond to a minimum height resolution of 30 m. The detection optics are contained within a light tight box. A sketch of the lidar system is shown in Figure 6. The laser (yellow), beam expander (blue) are located below the detection optics together with the beam steering mirror. Power supplies and the computer controlling the data acquisition are on the same frame as the optics (Figure 6). Further details on transmitter, receiver and data processing units can be found in the MSc thesis[1].

[1] McAuliffe, M.A.P., (MSc Thesis) *Implementation of a backscatter and Raman LIDAR station for studying the vertical aerosol distribution over Southern Ireland*, in *Department of Physics*. 2008, University College of Cork: Cork.

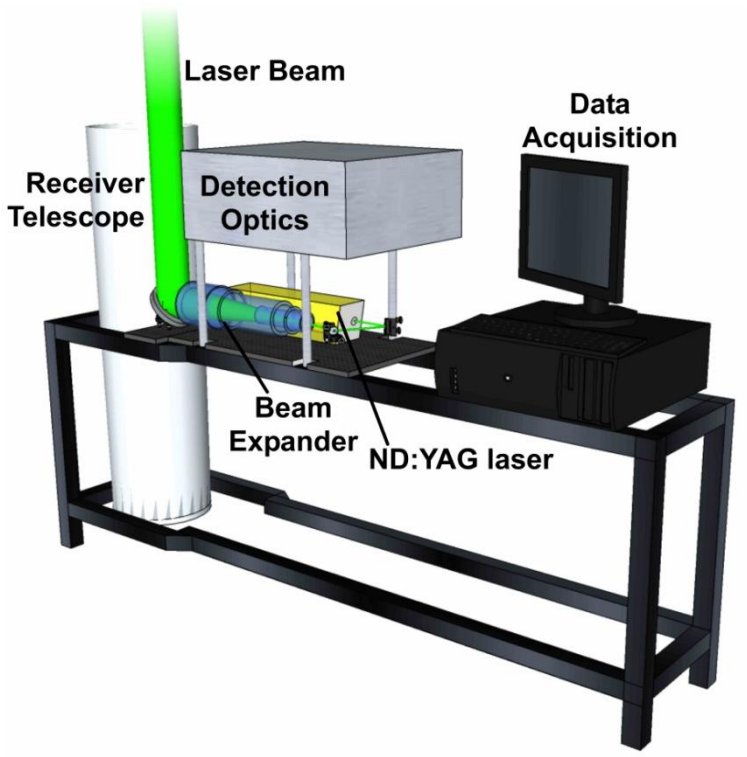


Figure 6. Schematic of UCLID setup, Computer (data acquisition), Beam Expander and Nd:YAG laser, detection optics aligned with the output of the Receiver Telescope.

3.2. Internal lidar checkup procedures

To ensure the data submitted to the EARLINET database is quality assured, several checkup procedures must be performed yearly. The procedures are listed below and will be discussed in more detail:

- Overlap function determination
- Telecover test
- Rayleigh fit
- Zero bin

3.2.1. Overlap function

The overlap between the laser beam and the telescope's field of view (FOV) as a function of altitude, *z*, is described by the overlap function, *O*(z). *O*(z) is critically dependent on the alignment of the laser beam with respect to the *FOV* of the telescope. With a ray tracing programme [87] overlap functions were simulated for the instrument's geometry and optical parameters, i.e. the primary mirror's focal length and diameter, the field stop diameter, and the distance of the beam steering mirror from the

main telescope's optical axis. Further analysis has been done on the theoretical overlap function using the ray tracing programme in the MSc thesis[2]. Based on the assumption that the overlap function for the elastic and inelastic backscatter measurement are identical, $O(z)$ can be determined using the iterative approach outlined in Wandiger and Ansmann [85]. The range-corrected ($\times z^2$) *and* overlap-corrected ($\times O(z)^{-1}$) experimental signal, $P_0(z)$, is proportional to the total backscatter coefficient, i.e. the sum of the elastic molecular backscatter coefficient at 532 nm, $\beta_{0,M}(z)$, and the Raman backscatter coefficient, $\beta_{Raman}(z)$:

$$P_0(z)O(z)^{-1}z^2 \propto \beta_{\mathrm{Raman}}(z) + \beta_{0,\mathrm{M}}(z) \tag{17}$$

The *only* range-corrected aerosol signal, is primarily a function of the total backscattering and the range-dependent overlap, as expressed by the Klett solution ($\beta_{\mathrm{Klett}}(z)$):

$$P_0(z)z^2 \propto \beta_{\mathrm{Klett}}(z) + \beta_{0,\mathrm{M}}(z) \tag{18}$$

The relative difference between the Klett and the Raman lidar solution,

$$\frac{P_0(z)O(z)^{-1}z^2 - P_0(z)z^2}{P_0(z)O(z)^{-1}z^2} \propto 1 - O(z) \tag{19}$$

can be used to calculate the overlap effect on the aerosol signal, by iteratively re-applying the Klett method to the (initially uncorrected, i = 1) elastic backscatter signal according to eq (20), see [85]:

$$P_{0,\mathrm{i}+1}(z) = P_{0,\mathrm{i}}(z)[1 + \frac{\beta_{\mathrm{Raman}}(z) - \beta_{\mathrm{Klett,i}}(z)}{\beta_{\mathrm{Raman}}(z) + \beta_{0,\mathrm{M}}(z)}] \tag{20}$$

Typically less than 15 iterations will remove the overlap effect completely. To determine the experimental overlap profile (shown in Fig. 2), a comparison is made with the measured signal profile and the corrected signal profile.

The overlap was also simulated as a function of the angle between the symmetry axis of the telescope's field of view, *FOV*, and the laser beam direction. The angle is

[2] McAuliffe, M.A.P., (MSc Thesis) *Implementation of a backscatter and Raman LIDAR station for studying the vertical aerosol distribution over Southern Ireland*, in *Department of Physics*. 2008, University College of Cork: Cork.

determined by $(FOV/2) - (x \times DIV)$, where *DIV* represents the divergence of the laser beam after expansion, and *x* is a multiplier. Changing *x* allows to control small changes in the angle between the laser beam axis and the telescope's *FOV* axis. For the two simulations shown in Figure 7 the values for *x* were chosen to be 1 and 1.5 as these multipliers appeared appropriate for a comparison with the experimentally determined overlap function.

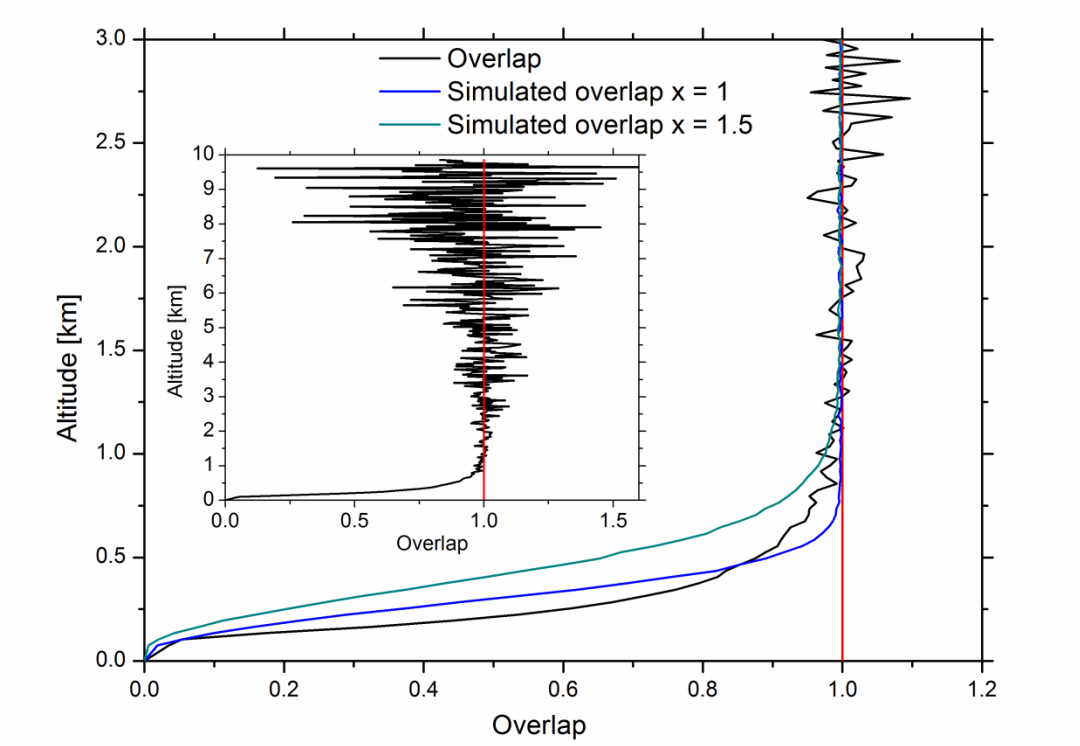


Figure 7. Measured (black line) and calculated (blue and green line for angle difference of x =1 and x = 1.5 respectively) overlap function for UCLID. The vertical red line indicates the complete overlap, i.e. O(z)=1. Insert: The same overlap function up to an altitude of 10 km.

The overlap of laser and *FOV* is complete at approximately 1000 m. Having a low complete overlap makes UCLID ideal for monitoring the boundary layer. Based on the comparison in Fig. 2, the angle between the laser beam axis and the telescope's *FOV* axis is smaller than $(0.5 \times DIV)$. The accuracy for measuring the field stop diameter of UCLID is ≈ 0.25 mm. For the given setup, changing the field stop from 1.1 mm to 1.2 mm increases the *FOV* from 0.73 mrad to 0.80 mrad. The *FOV* for the experimentally measured overlap is possibly larger than the value used in the simulation. Therefore it is be possible to reduce the height at which the overlap is complete. If the diameter of the field stop is unintentionally larger than required, the PMTs may be exposed to excess light in the near field of the telescope (below 700 m) causing the PMTs to saturate. This

scenario has not been observed with UCLID due to careful neutral density filter selection.

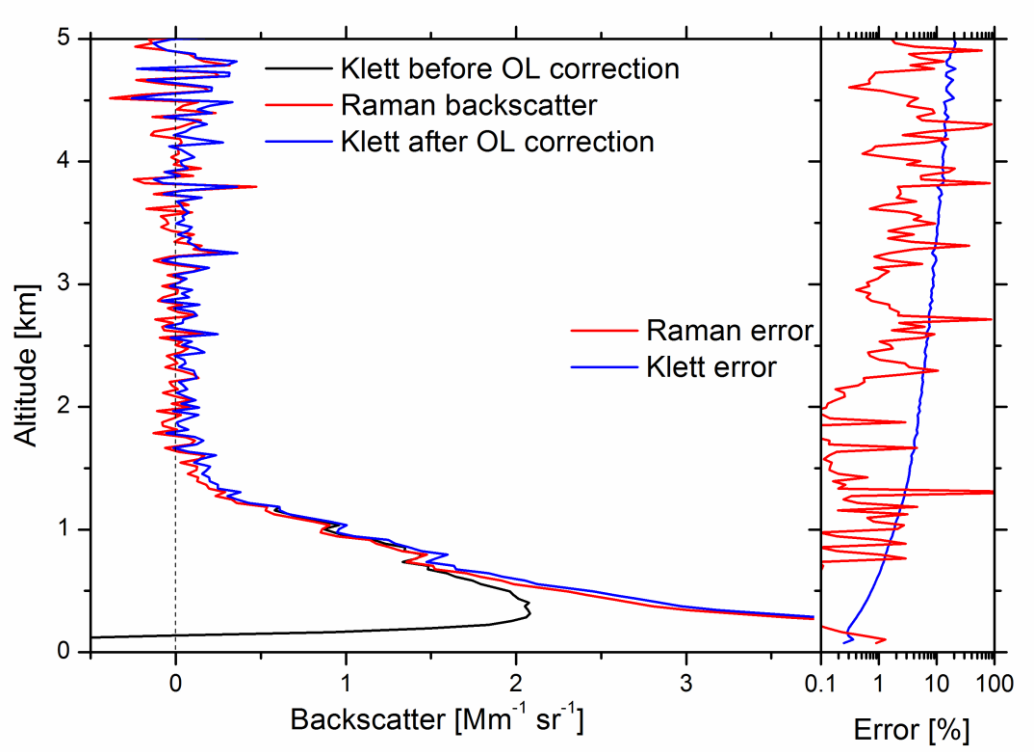


Figure 8 Left: Comparison between an uncorrected (black line) and corrected (blue line) Klett backscatter profile and a Raman Backscatter profile (red line). Right: Percentage error for the Klett (blue line) and Raman (red line) Backscatter solutions.

Figure 8 shows a backscatter signal from UCLID measured on 17 January 2011. The plot contains 3 profiles; an uncorrected Klett Backscatter profile (black line), a corrected Klett Backscatter profile (blue line) and a Raman backscatter profile (red line). These profiles were measured over a 2 hr period, with very clear conditions. A lidar ratio of 25 sr was used for the calculation of the Klett solutions.

Since the Raman backscatter profile is independent of the overlap function, it can be directly compared with the corrected Klett solution (Figure 8), and the agreement is satisfactory. At altitudes larger than approximately 700 m all three profiles (including the uncorrected Klett solution) agree very well. Below that altitude, however, the uncorrected Klett solution strongly deviates from the other two profiles, illustrating the necessity to perform an overlap correction. The percentage errors of the Raman backscatter (red) and Klett solution (blue) are shown in the right panel of Figure 8. The

latter gradually reaches 20% at 5 km. The substantial variation in the error of the Raman backscatter is due the inelastic signal being significantly weaker.

3.2.2. Telecover Test

For an ideal lidar system, the backscatter rays from all altitudes within the measurement range have the same transmission in the optical detection system. In the near field of the telescope, however, the total transmission decreases due to the field stop and/or other apertures in the optical system, which cause the overlap function to decrease to values substantially smaller than 1. In addition, backscattered light with large angles of incidence with respect to the optical axis of the receiver telescope can have reduced transmission due to the angular dependence of the interference filter transmission, see Figure 9.

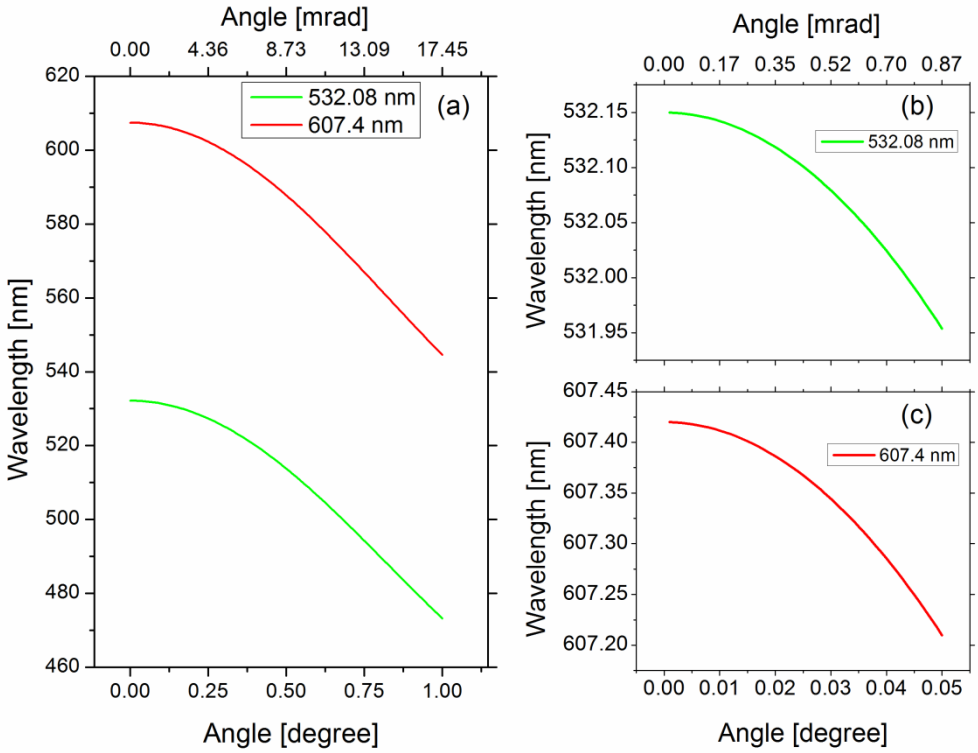


Figure 9. Angular wavelength shift with incident angle of the interference filters. Plot (a) shows the wavelength shift for both filters for a range of 1 degree. Plot (b) and (c) shows the wavelength shift for the 532.08 nm and 607.4 nm for a range of 0.05 degree, respectively.

To check the performance and alignment of the optical detection system the so-called "telecover test" was developed by V. Freudenthaler [88]. The test involves comparing the range dependent lidar signals of backscattered rays from different parts of the telescope aperture. This is achieved by blocking ¾ of the telescope aperture with an

opaque substrate. The quadrants of telescope are named North (N), East (E), West (W) and South (S). North is oriented from the telescope optical axis towards the laser optical axis as seen in Figure 10.

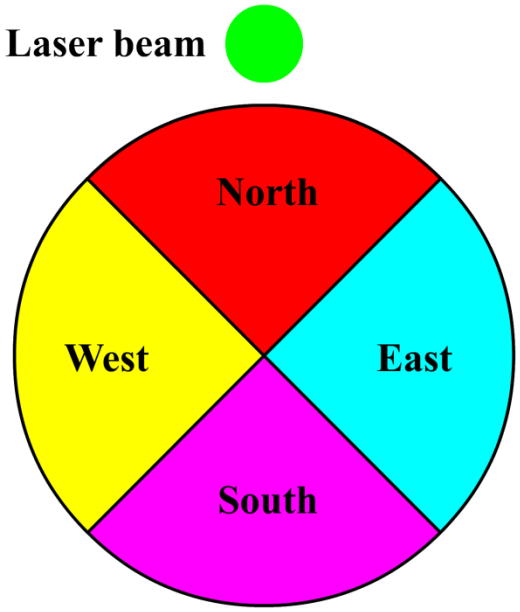


Figure 10. Test sections of the covered telescope aperture, all apertures have the same effective area.

The telecover test procedure involved the following steps:

1. Measure 532 nm and 607 nm backscatter signal for each quadrant for ca. 10 minutes.
2. Repeat the first sector (North) measurement to obtain information about potential atmospheric changes during the test (North 2 or N2).
3. Normalize all N, E, W, S, N2 range corrected profiles to 1.0 in the far range above the height where the differences between the signals can be unambiguously identified.
4. Determine the deviation of the signals from the mean of the N, E, W, S quadrants.

Figure 11 and Figure 13 show the normalized, range corrected signal for 532 nm and 607 nm, respectively. Both signals were normalized on the basis of the data from 4-8 km, thus the smallest relative deviation from the mean is expected in this range. Figure 12 and Figure 14 show the relative deviation from the mean for 532 nm and 607 nm respectively. Figure 11 to Figure 14 all use the same colour code to help compare

signals: North (N) is red, East (E) is cyan, South (S) is yellow, West (W) is yellow, North2 (N2) is black and the mean of N, E, W, S is orange.

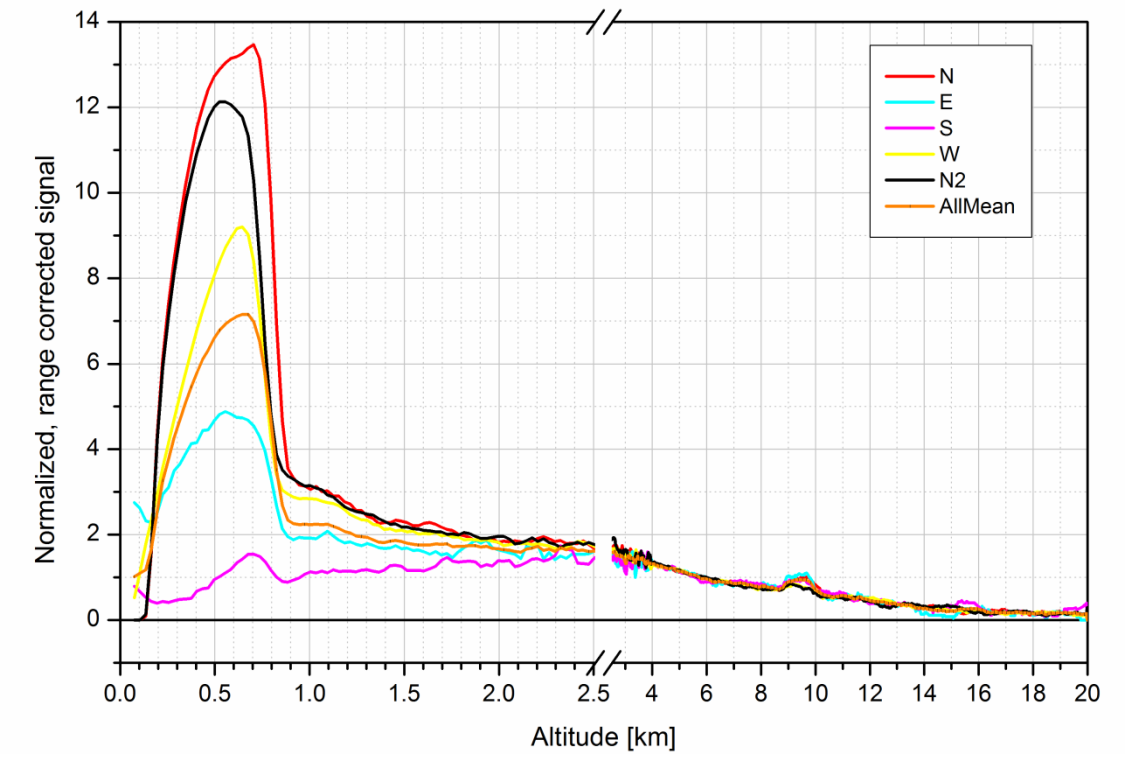


Figure 11. Normalized range corrected signal for the 532 nm telecover test. Normalization procedure performed between 4-8 km. N (red line) and N2 (black line) shows any atmospheric changes during the measurements.

Comparing the signals in Figure 11, the W signal is higher than the E and S signal; this is also the case in Figure 13. As both wavelengths exhibit the same W, E and S relative intensity it indicates that it is not caused by any misalignment of the detection optics (Figure 4 – unit (B)). For ideal telecover test results, it is expected that the E, S and W signals have the same values after normalization, while the N signal will be somewhat greater due to N section being closest to the propagation axis of the laser beam.

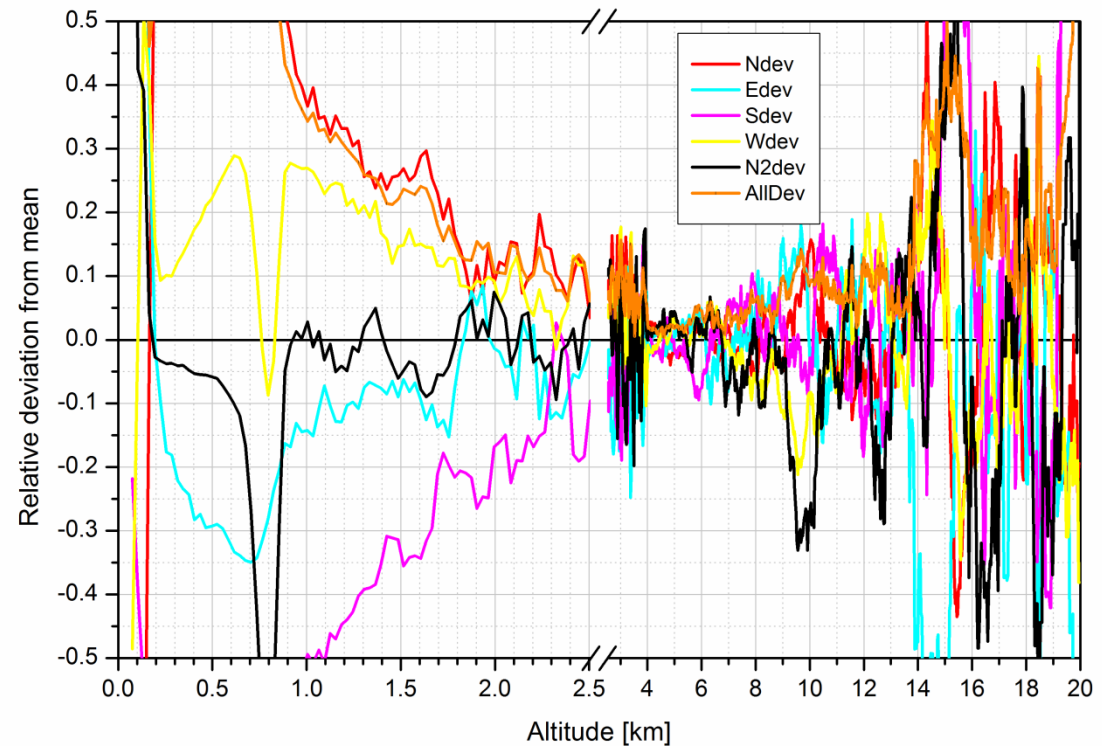


Figure 12. Relative deviation from the mean of all the profiles for the 532 nm telecover test.

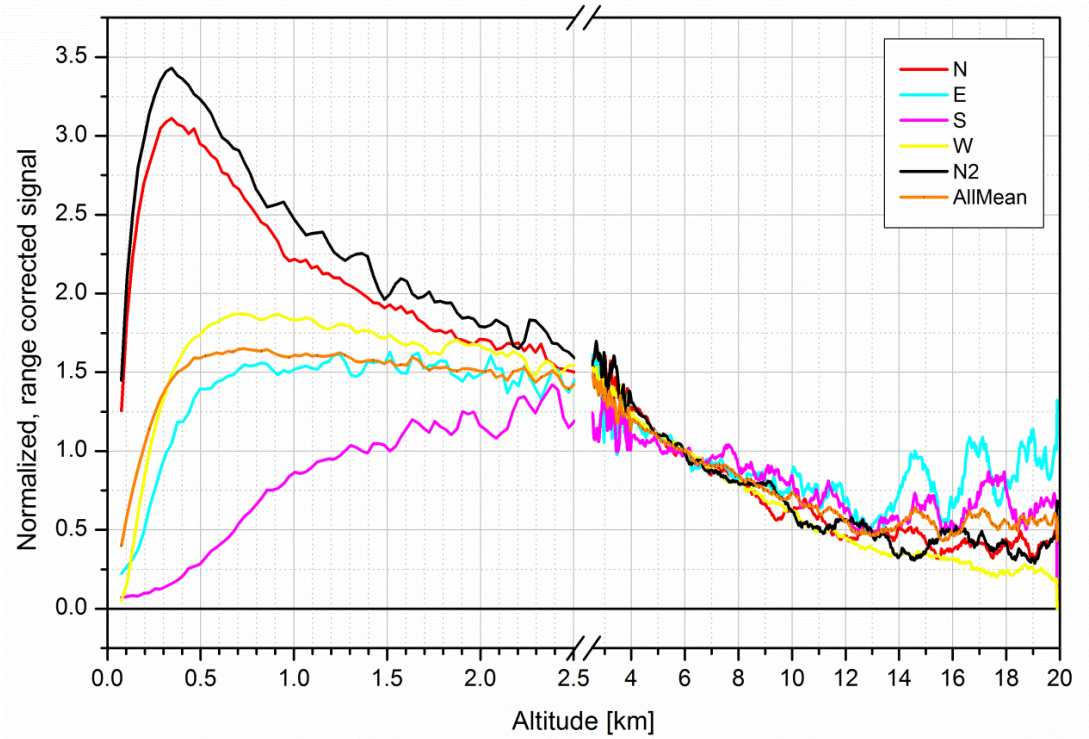


Figure 13. Normalized range corrected signal for the 607 nm telecover test. Normalization procedure performed between 4-8 km.

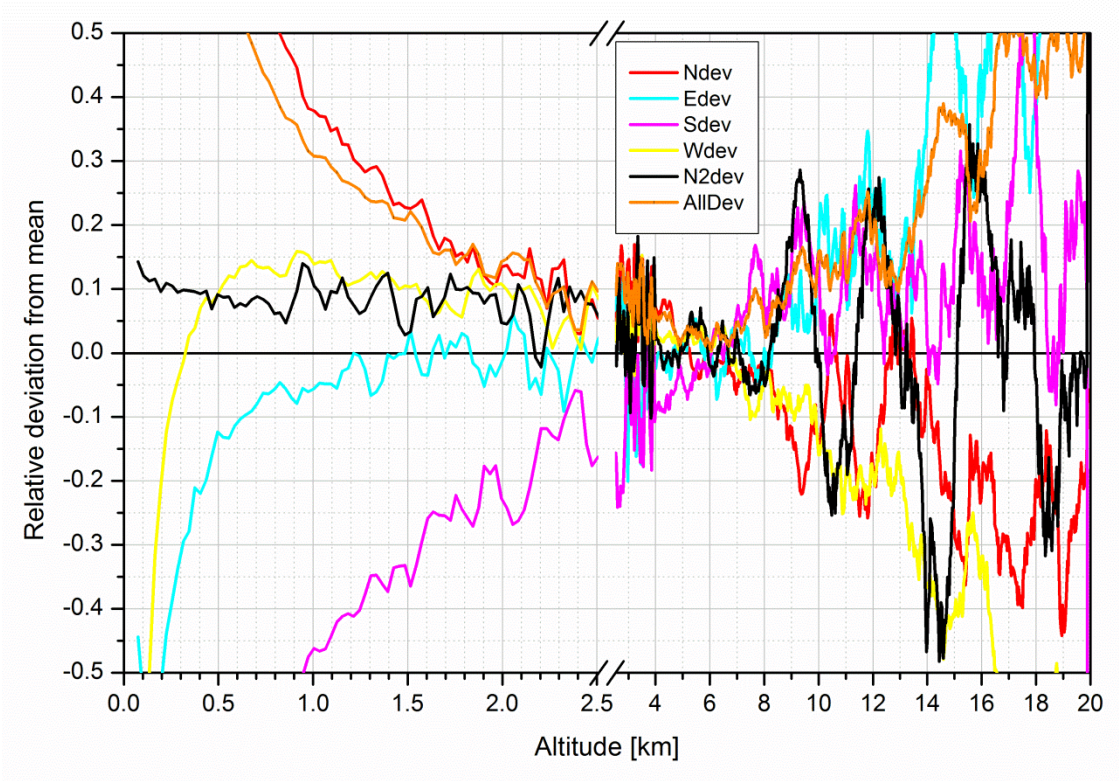


Figure 14. Relative deviation from the mean of all the profiles for the 607 nm telecover test.

The results from the telecover test indicates that the laser alignment may need to be improved for the near field or that the field stop may be too narrow which would cause the E, W, S quadrants to have different intensities. Figure 12 and Figure 14 show clearly the discrepancies between the quadrants in the near field range of UCLID, while in far field range (> 4 km) the normalized range corrected signals agree well. The telecover test exemplified here indicates that there is no substantial misalignment between the telescope's FOV and the laser beam (i.e. a bad overlap function). The signals from the far field show good agreement which will be discussed in the Rayleigh fit section, but that there may be an aperture in the telescope causing the E, S and W signals to deviate, such as a misalignment between the telescope's secondary mirror and the detection optics.

3.2.3. Rayleigh fit

While the telecover test provides information about the near range of the lidar, another procedure is required to check the quality of the signals in the far range. The Rayleigh Fit procedure involves fitting a normalized lidar signal to the calculated attenuated Rayleigh backscatter coefficient ($\beta_{\mathrm{mol}^{\mathrm{attn}}}$) in a range where (i) aerosol-free conditions can be assumed (i.e. only elastic molecular backscatter contributes to the signal) and

where (ii) the calculated signal fits the lidar signal with the least relative deviation (corroborating assumption (i)). From Bucholtz, A. [81] the total Rayleigh scattering cross section per molecule, α, is calculated from eq (21):

$$\alpha(\lambda) = \frac{24\pi^3({m_{\text{air}}}^2 - 1)^2}{\lambda^4 {N_s}^2({m_{\text{air}}}^2 + 2)^2}\frac{6 + 3\gamma}{6 - 7\gamma} \tag{21}$$

Where:

λ . . . wavelength [cm]

$\alpha(\lambda)$ . . . total Rayleigh scattering cross section per molecule [cm^2]

m_{air} . . . refractive index of air [1]

N_s . . . molecular number density for standard air [cm^{-3}]

γ . . . wavelength dependent depolarization factor - a term that accounts for the anisotropy of air molecules [1]

In Böckmann, et al. [42] the procedure to determine the extinction resulting from eq (21), is outlined (eq (22)):

$${\alpha_{\text{mol}}}^{\text{sca}}(z, \lambda; p, T) = \frac{24\pi^3({m_{\text{air}}}^2 - 1)^2}{\lambda^4 {N_s}^2({m_{\text{air}}}^2 + 2)^2}\frac{6 + 3\gamma}{6 - 7\gamma} \times N_s \frac{T_0}{p_0}\frac{p(z)}{T(z)} \tag{22}$$

Where:

T_0 . . . ground level temperature [K]

$T(z)$ . . . temperature profile obtained from radiosonde measurement [K]

p_0 . . . ground level pressure [hPa]

$p(z)$ . . . pressure profile obtained from radiosonde [hPa]

Using the ratio $\alpha_{\text{mol}}(\lambda, z)/\beta_{\text{mol}}(\lambda, z) = 8\pi/3$, the Rayleigh backscatter coefficient, β_{mol}, can be determined.

Steps involved in the Rayleigh fit procedure:

1. Select a range in the lidar signal where clean air can be assumed (z_{max}, z_{min}).
2. Calculate the attenuated Rayleigh backscatter coefficient, ${\beta_{\text{mol}}}^{\text{attn}}$, using radiosonde profiles, with attenuation starting at the middle range bin (z_0, reference range) of the selected range (z_{max}, z_{min}). Eq (23) shows the attenuation correction:

$$\beta_{\mathrm{mol}^{\mathrm{attn}}}(z, z_0) = \beta_{\mathrm{mol}} \exp\left[-2 \int_{z_0}^{z} \alpha_{\mathrm{mol}}(z')dz'\right] \quad (23)$$

This means negative attenuation for $z < z_0$, and keeps the exact reference value at the reference range z_0, i.e. $\beta_{\mathrm{mol}^{\mathrm{attn}}}(z_0, z_0) = \beta_{\mathrm{mol}}(z_0)$.

3. The agreement of the fit needs to be checked by comparing the slope of $\beta_{\mathrm{mol}^{\mathrm{attn}}}$ of as a function of height and the range corrected lidar signal.
4. If the fit is not within 2σ, steps 1 - 3 are repeated.
5. If step 4 is successful, the lidar signal, $P(z)$, is normalized to $\beta_{\mathrm{mol}^{\mathrm{attn}}}$ using the mean of $\beta_{\mathrm{mol}^{\mathrm{attn}}}$ and $P(z)$ over the fit range, see eq (24):

$$P^{\mathrm{norm}}(z, z_0)z^2 = P(z)z^2 \frac{\int_{z_{\mathrm{min}}}^{z_{\mathrm{max}}} \beta_{\mathrm{mol}^{\mathrm{attn}}}(z, z_0)dz}{\int_{z_{\mathrm{min}}}^{z_{\mathrm{max}}} P(z')z'^2 dz'} \quad (24)$$

6. The middle range bin, z_0, provides a good reference height when using the Klett method (Section 2.2 - eqs (12) to (14)).

Figure 15 and Figure 16 show the results from the Rayleigh fit for the 532 nm and 607 nm signal, respectively. The insert shows the range corrected lidar signal and the attenuated Rayleigh signal before the normalization procedure is performed. Both signals were normalized over the same range, z_{min} = 13 km and z_{max} = 15 km. Figure 17 and Figure 18 show the relative deviation of the normalized range corrected signal from the attenuated Rayleigh backscattering signal. The result of the Rayleigh fit show that the overlap in the far range field is complete and there is good agreement with the attenuated Rayleigh backscattering signal. The 607 nm signal has a lower signal to noise (S/N) compared to the 532 nm signal, hence larger deviations are evident, in Figure 18 in comparison to Figure 17.

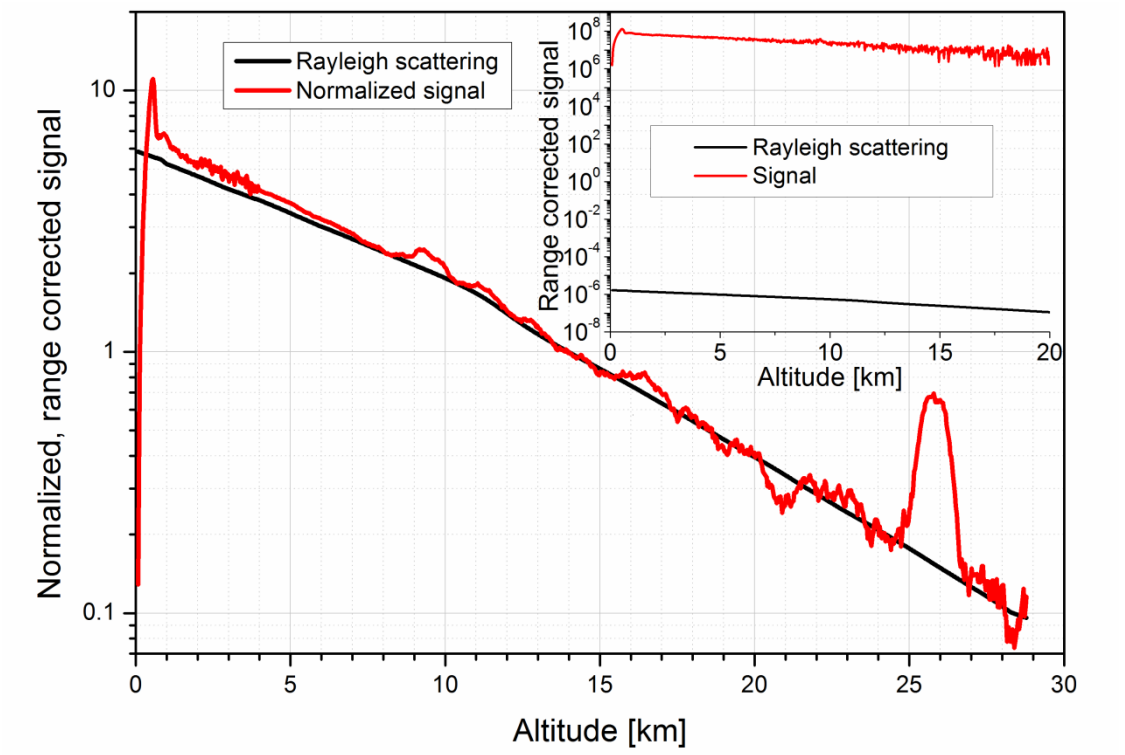


Figure 15. Rayleigh Fit for 532 nm normalized signals. Normalization range (z_{min}, z_{max}) from 13 km to 15 km. Insert shows the Range corrected lidar signal (red line) and the attenuated Rayleigh scattering (black line).

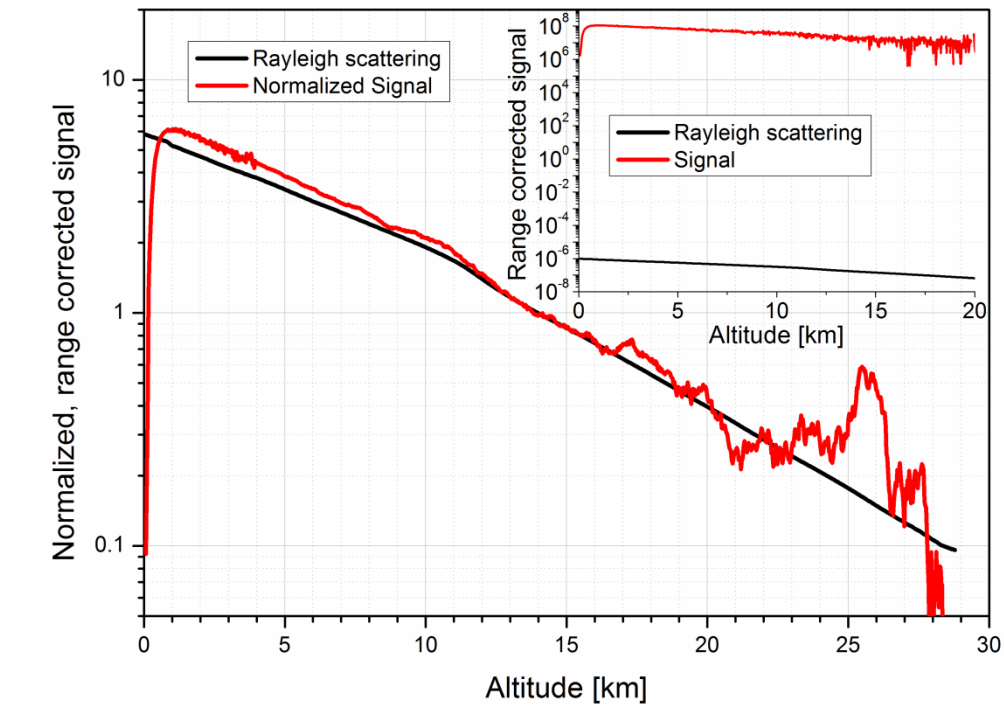


Figure 16. Rayleigh Fit for 607 nm normalized signals. Normalization range (z_{min}, z_{max}) from 13 km to 15 km. Insert shows the range corrected lidar signal (red line) and the attenuated Rayleigh scattering (black line).

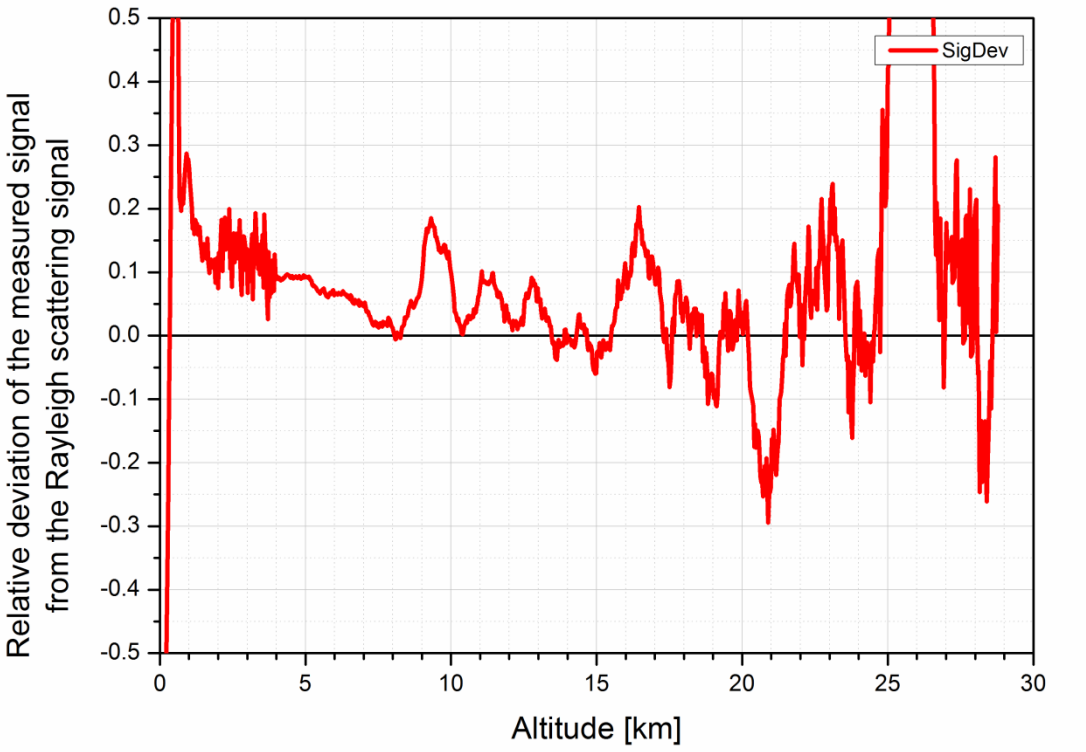


Figure 17. Relative deviation for the Rayleigh Fit to the elastic backscattering signal at 532 nm. The red line is the deviation of the normalized lidar signal from the attenuated Rayleigh scattering.

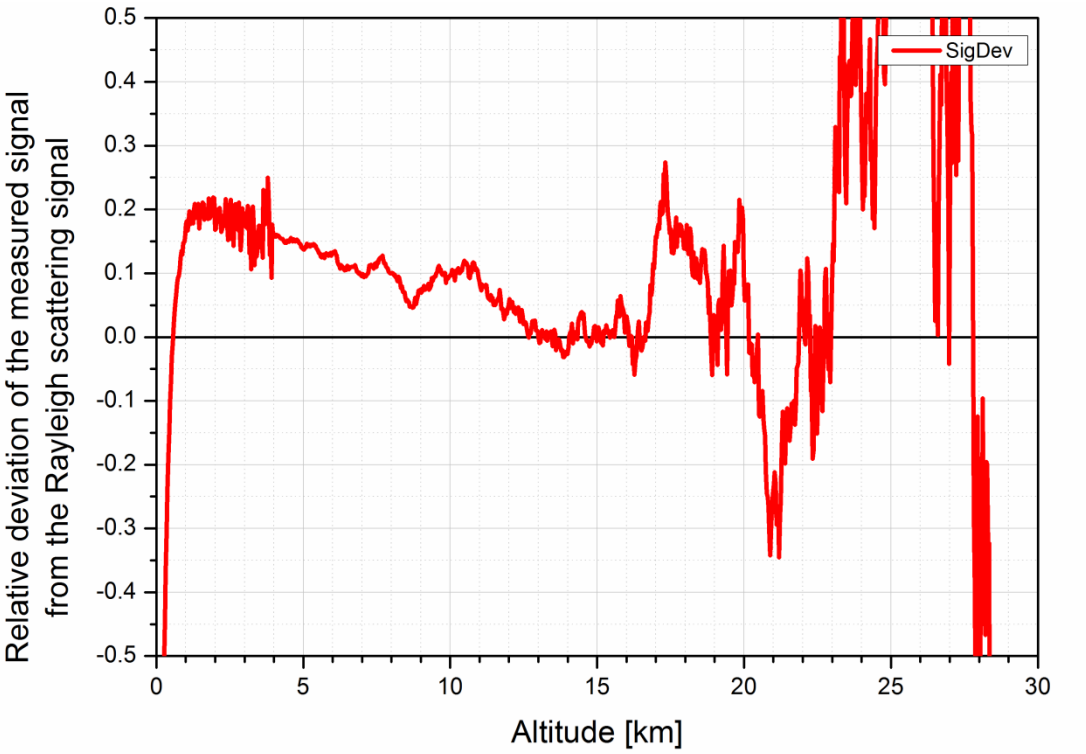


Figure 18. Relative deviation for the Rayleigh Fit to the elastic backscattering signal at 607 nm. The red line is the deviation of the normalized lidar signal from the attenuated Rayleigh scattering.

3.2.4. Zero bin measurement

When the trigger from the laser starts the transient recorder, there can be an error in the trigger delay which causes large errors in the near range signal. The Raman signals can be considerably affected by the error from the trigger delay, because during the Raman analysis the slope from the near field signal changes depending where the zero bin is assumed.

Figure 19 (provided by Volker Freudenthaler (EARLINET-ASOS NA3 Internal lidar checkup procedures - http://www.meteo.physik.uni-muenchen.de/)) illustrates the consequences a wrong definition of time zero can have on the extinction coefficient.

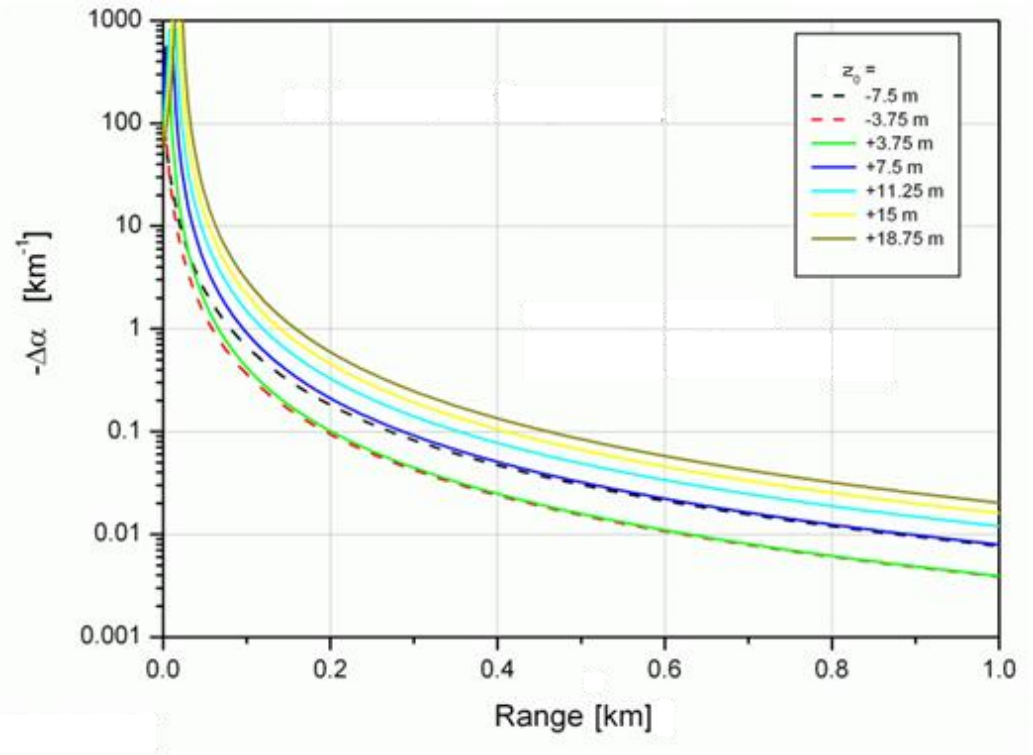


Figure 19. Absolute error of the extinction coefficient α from Raman measurements due to uncertainty z_0 in the true zero bin. Image provided by Volker Freudenthaler (EARLINET-ASOS NA3 Internal lidar checkup procedures - http://www.meteo.physik.uni-muenchen.de/).

The zero bin measurement is more relevant for systems which have a smaller transient recorder bin width. For example LICEL detection systems have a bin width of 50 ns, while UCLID has a bin width of 200 ns, therefore a trigger delay of ± 50 ns would affect the LICEL systems more. To measure the zero bin for UCLID, a near range target with a defined distance to the lidar detection unit was used to produce a signal peak for the zero bin calibration from the roof of the dome (enough light was scattered from the

fibre glass roof). The telescope aperture was covered to reduce scattered light; a 60 mm opening allowed the reflected light from the target to be detected. The q-switch trigger output which triggers the transient card has an added delay so that the near range reflection is recorded in the second range bin (bin number 1 as seen in Figure 20).

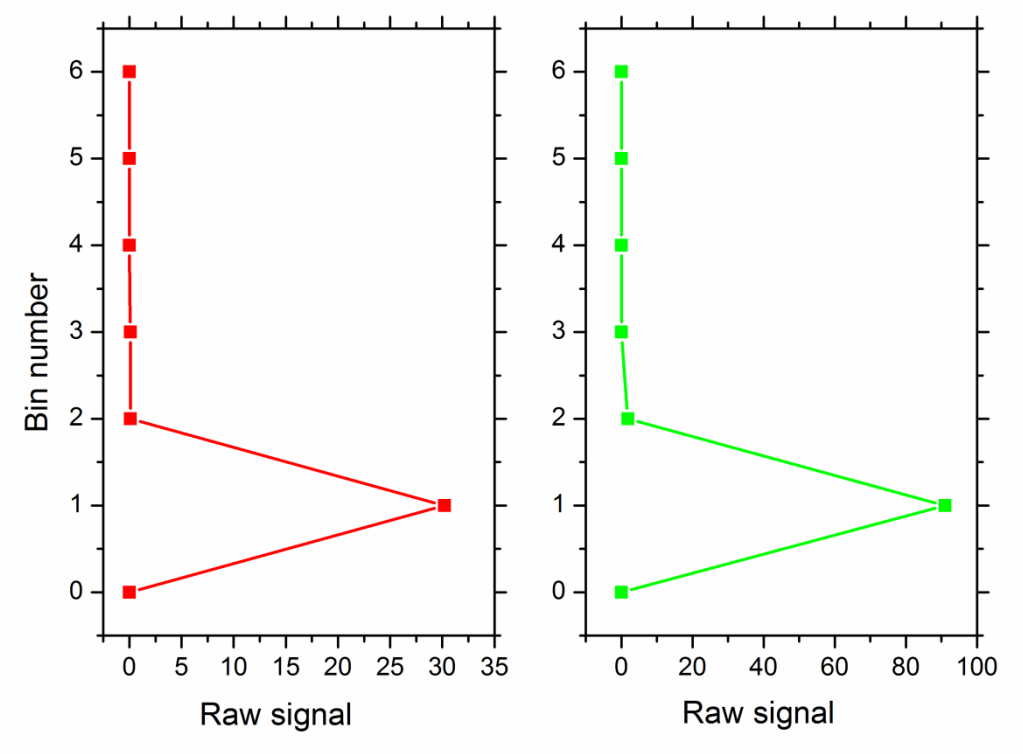


Figure 20. Zero bin pulse of UCLID from reflections of the outgoing laser pulse from the roof of the dome. Left is the 607 nm zero bin pulse, right is the 532 nm zero bin pulse.

The zero bin measurements include any additional delays between the optical laser pulse and the time the electronic trigger pulse from the laser electronics reaches the trigger input of the data acquisition system due to delays in the laser electronics. From Figure 20, the zero bin is bin number 1, therefore all profiles have the first bin (bin number 0) removed before analysis is performed.

4. Results and Discussion

4.1. Climatology measurements

The analyses of measurements taken with UCLID have undergone extensive quality assurance procedures. The inversion algorithms [43] for both elastic and Raman lidar data have been quality assured within EARLINET using the same data and comparison as outlined in [42]. Table 4 shows the number of measurements performed for each season over the periods, April 2010 to May 2011 and February 2012 to June 2012. During the period from June 2011 to January 2012 no measurements were performed due to upgrading works of UCLID. Based on air temperature the four seasons are divided into the following three-month periods to study climatological aspects of the lidar data: December to February - winter, March to May - spring, June to August- summer, and September to November - autumn. This is a common grouping in meteorological sciences of many countries at middle to northern latitudes. During analysis the standard deviation are weight according to the Student t-distribution, where applicable (i.e. where values in Table 4 are less than >20)

Table 4. Number of measurements available for each season which include information about the PBL height, lidar ratio (LR) and aerosol optical density (AOD). A number of measurements contained Klett solutions, i.e. no lidar ratio or AOD values could be derived.

	All	Winter	Spring	Summer	Autumn
PBL	66	11	20	22	13
LR/AOD	47	6	16	18	7

The planetary boundary layer (PBL), aerosol optical density (AOD) and the lidar ratio values will be discussed and compared with values from literature. The determination of the boundary layer height from the lidar data is done by finding the first significant negative gradient in the range-corrected lidar signal, starting from ground.

The PBL is the atmospheric region with the highest concentration of aerosol between the ground level and the free troposphere. An aerosol-based definition of the PBL is given by White et al. [89] as the top of the atmospheric region where the friction and the convection generated at the surface influences directly the turbulent mixing which determines the homogeneous distribution of the aerosol. The PBL height refers to the top of the PBL layer.

AOD is a quantitative measure of the atmospheric extinction through a vertical column of atmosphere from the point of observation to a defined height in the atmosphere (e.g. 0 to 1 km and 0 to 2 km). The AOD is derived by extrapolating the lowest data point down to ground assuming a constant value of the aerosol extinction coefficient in this lowest layer; the values are then integrated over the whole layer. The lidar ratio is derived from the ratio of the extinction coefficient to the backscatter coefficient. The lidar ratio provides information on aerosol typing (i.e. marine, dust, anthropogenic particles etc.).

PBL height

The mean seasonal (red columns) and the mean monthly (blue line) values of the PBL height are shown in Figure 21. The error bars show the standard deviation of the seasonal values and the dashed blue line indicates the standard deviation of the monthly values. It is evident that the PBL height has a seasonal and monthly dependence, similar to other European lidar stations [90]. In reference [90] it is also reported that the PBL height increases during the summer months.

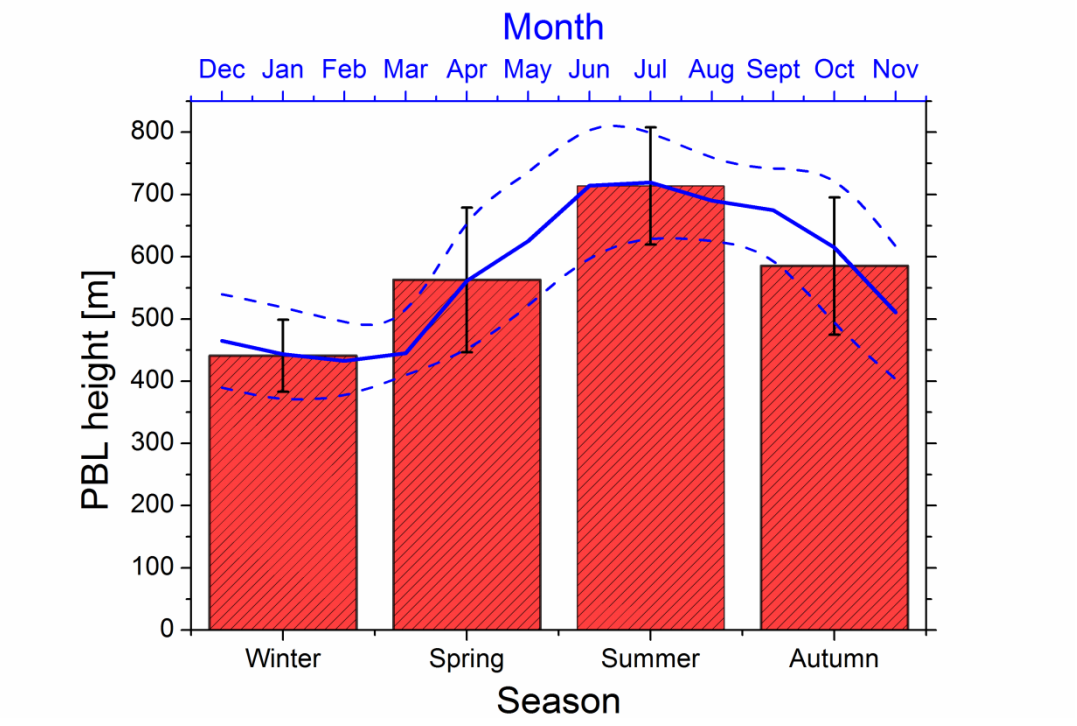


Figure 21. Mean seasonal height of the PBL (red bars), error bars show the 1σ weigh standard deviation. Mean monthly height of the PBL (solid blue), dashed line indicates the interpolated 1σ weigh standard deviation on the monthly average. Over the periods from April 2010 to May 2011 and February 2012 to June 2012.

The arithmetic average of the PBL height over Cork is 608 ± 138 m and the median value is 615 m. The average PBL height for the Cork site is significantly lower than for other European lidar stations [90], especially in comparison with Aberystwyth where a PBL height of ca. 1200 ± 480 m was reported over a two year period (55 measurements were taken into account). However, there is good agreement with reported heights of the PBL for Ireland. Studies of the PBL layer over Ireland have been performed using a wind lidar at the Mace Head Atmospheric Research station at the western coast of Ireland [91]. The authors observed typical PBL heights to vary between 600 and 1500 m from period between 1 August and 1 September 2002. Kunz et al. [92] carried out a study with a backscatter lidar operating at 1064 nm wavelength to measure the depth and structure of the coastal atmospheric boundary layer. The measurements were made during campaigns undertaken in September 1998 and in June 1999 at the Mace Head Atmospheric Research station. The authors report the PBL height to vary between 600 and 1200 m over a period of a few hours. No average PBL height was given by the authors but measured heights range from 400 to 1800 m from 6 – 13 June and 300 to 1000 m from 20 – 30 June [92].

Aerosol optical depth

The AOD is calculated within the PBL, 0 - 1 km layer, 0 - 2 km layer and in the fixed layer of 1 – 2 km to enable comparisons with literature. Figure 22 shows the mean seasonal AOD, higher values are expected during spring and summer, partly due to higher PBL heights, but also due to wind direction. Figure 23 shows the wind direction and frequency of wind speeds in the Cork region from January 2010 to May 2012 for each season. During the winter months it is evident that the prevailing wind directions are WSW and SW giving clean maritime conditions and a low AOD. During spring the WSW is still a major factor but there is an increase in the occurrence of wind directions from the E, ESE, SE, SSE and S, which would transport continental aerosol and dust particles from Europe. The summer wind chart show prevailing wind directions from WNW, W, SW and SSW, in particular the SW and SSW directions could potentially transport Saharan dust into Irish air space. A report by EARLINET indicates that during May 2000 to December 2002, the largest number of dust cases was recorded from late spring until early autumn months [93] with most dust events occurring during summer. The autumn wind chart in Figure 23 shows a decrease of wind direction from the SSW.

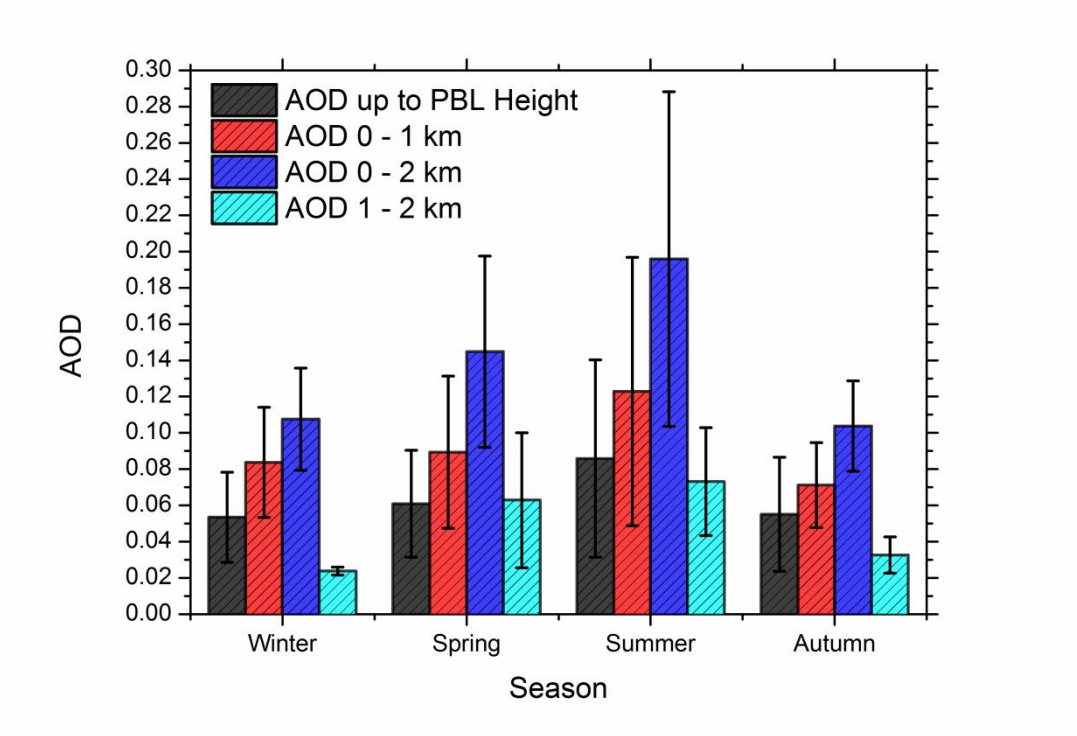


Figure 22. Mean seasonal aerosol optical depth for Southern Ireland. Black - AOD from ground to the PBL height, red - AOD from ground to 1 km asl, blue - AOD from ground to 2 km asl and cyan - AOD between 1 - 2 km asl. Error bars represent the 1σ weigh standard deviation of the average.

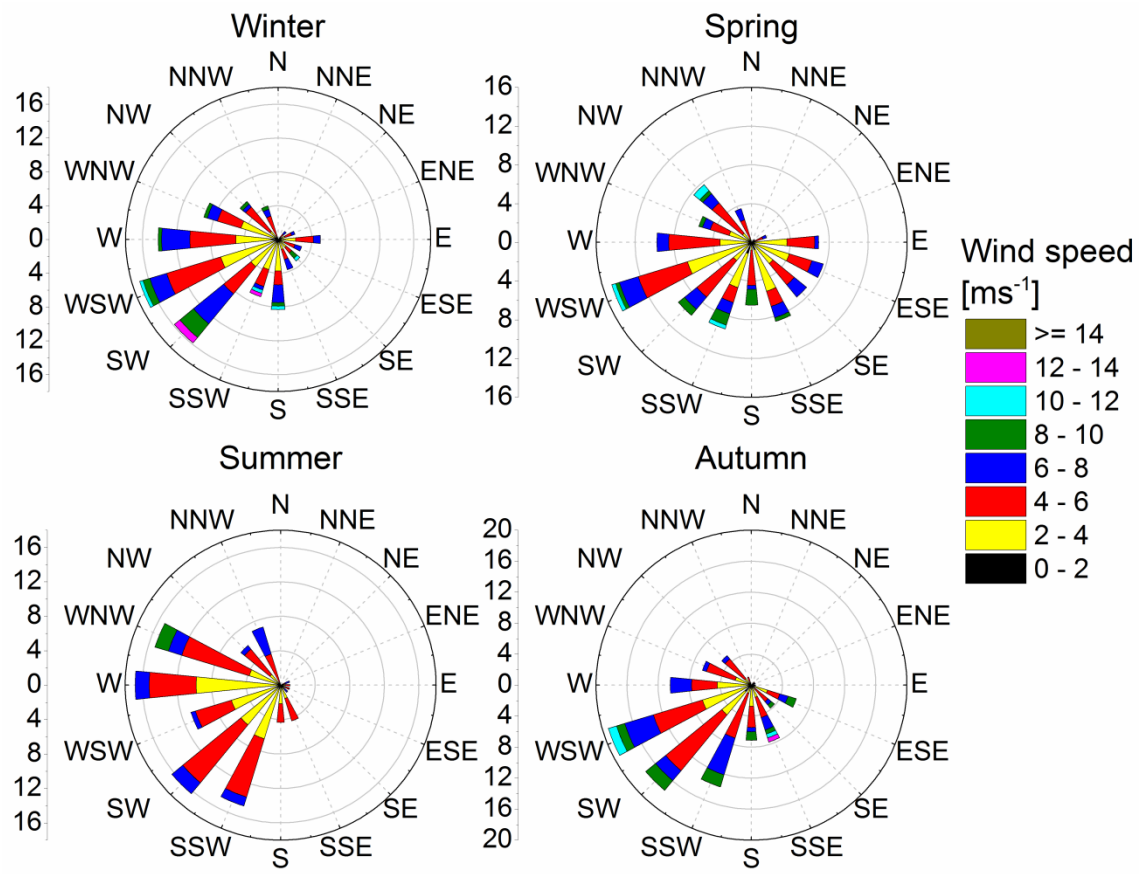


Figure 23. Summary of wind direction and frequency of wind speeds from 1 January 2010 to 30 April 2012 for each season for the Cork region. Axes on the left represent the fraction of wind speeds that occurred in a certain direction in percent, e.g. for winter ca. 12% of all wind direction are from the SW. The colour plot on the right represents the wind speed, e.g. for the SW direction in winter ca. 4% of the wind had a speed between 2-4 ms^{-1} (yellow), ca. 4% between 4-6 ms^{-1} (red), ca. 4% between 6-8 ms^{-1} (blue) and so forth. Data provide by Met Éireann [94].

The AOD of the 0 - 1 km layer is larger in comparison the AOD within the PBL because the PBL height is quite low at the Cork site as small amounts of free troposphere aerosol particles are included in the 0 - 1 km layer. The large AOD standard deviation for spring and summer is due to the mixed conditions measured (i.e. maritime, polluted dust, dust and continental aerosol particles). Since the PBL height is low, ca. 70 % of the total AOD is due to the lowest 1 km whereas in other north European lidar station ca. 60 % of the total AOD is confined in the lowest 1 km and 80 – 90 % in the lowest 2 km [90]. A statistical analysis of Raman lidar data from 10 EARLINET stations has been performed by Matthias et al. [90]. AOD from the lidar station at Aberystwyth are compared with AOD values at Cork since the atmospheric conditions at Aberystwyth were expected to be most similar to those in (Table 5). The data from

Aberystwyth are aerosol backscatter coefficient profiles at 355 nm in the near UV. Therefore the different wavelengths at Aberystwyth and Cork need to be considered in a comparison of AOD.

$$\tau_\lambda = \tau_{\lambda_0} \left(\frac{\lambda}{\lambda_0}\right)^{-å} \tag{25}$$

Where:

τ_λ . . . Aerosol optical depth with the wavelength λ of incident light **[1]**

τ_{λ_0} . . . Aerosol optical depth with the wavelength λ_0 of incident light **[1]**

å . . . Angström exponent **[1]**

A study carried out at the Mace Head atmospheric research station for the period 2002–2004 measured an Angström Exponent of 0.40 ± 0.29 in clean conditions using a radiometer to measure the AOD [95]. Using the Angström Exponent (0.40 ± 0.29) and eq (25) the AOD at 532 nm are extrapolated to 355 nm, see Table 5.

Table 5. Average and Median of aerosol optical depth in the PBL and the lowest 2 km layer for Cork and Aberystwyth. Aberystwyth AOD values are from table 3 in [90]. The errors represent the 1σ standard deviation of the average, and errors for the AOD at 355 nm for Cork are derived from error propagation.

	Cork 532 nm	**Cork 355 nm**	**Aberystwyth**
Average AOD - PBL	0.069 ± 0.042	0.081 ± 0.049	0.16 ± 0.13
Average AOD - 0 - 2 km	0.158 ± 0.074	0.186 ± 0.087	0.23 ± 0.16
Median of AOD - PBL	0.053	0.063 ± 0.007	0.135
Median of AOD - 0 - 2 km	0.138	0.163 ± 0.019	0.175

There is a noticeable difference of the mean AOD up to the PBL height between Cork and Aberystwyth. This is yet again due to the lower average PBL height over Cork (608 ± 138 m) compared with Aberystwyth (1204 ± 481). The mean AOD at 355 nm in the 2 km layer show good agreement with Aberystwyth. In reference [90] it is also reported that the lowest values of the AOD are found in the north-western part of Europe (Aberystwyth), and the highest values in the south-eastern part (Athens, Thessaloniki). An annual cycle of the AOD with higher values in summer than in winter is observed at other EARLINET lidar stations which agree with the cycle evident in Figure 22.

A study by Mulcahy et al. [95] report the total AOD measured at the Mace Head atmospheric research station using a precision filter radiometer. The authors report a

three year average of the AOD of clean marine air masses at 500 nm to be 0.14 ± 0.06 and polluted air masses to be 0.19 ± 0.05. There is no total AOD available at the Cork site but as previously stated 80 - 90 % of the total AOD is confined in the first 2 km [90], hence AOD measured at Cork between 0 - 2 km for clean and polluted conditions can be compared with the total AOD. The AOD at the Cork site between 0 - 2 km for clean marine air masses is 0.119 ± 0.023 and for polluted air masses 0.170 ± 0.036. These values are within 80 - 90 % of the total AOD found at Mace Head. A rather comprehensive study by Smirnov et al. [96] of optical properties of atmospheric aerosol in maritime and coastal areas show the AOD to be in agreement with those found at the Cork site.

Lidar ratio and Backscatter profiles

The lidar ratio at the PBL height and from ground levels up to the PBL height for the Cork site show an annual cycle, evident in Figure 24. This is expected, given the seasonal dependence of the AOD. There is a larger standard deviation for the spring and summer mean lidar ratios, since these seasons experience more frequent aerosol loads, such as continental aerosol particles and dust particles from the Saharan desert. The annual cycle of the lidar ratio is confirmed at other EARLINET station [97, 98]. The lidar ratio for winter and autumn are in agreement with expected lidar ratio for maritime conditions [99]. Summer and spring lidar ratios range from 20 to 60 sr, indicating anthropogenic aerosol particles, dust particles and continental aerosol [99].

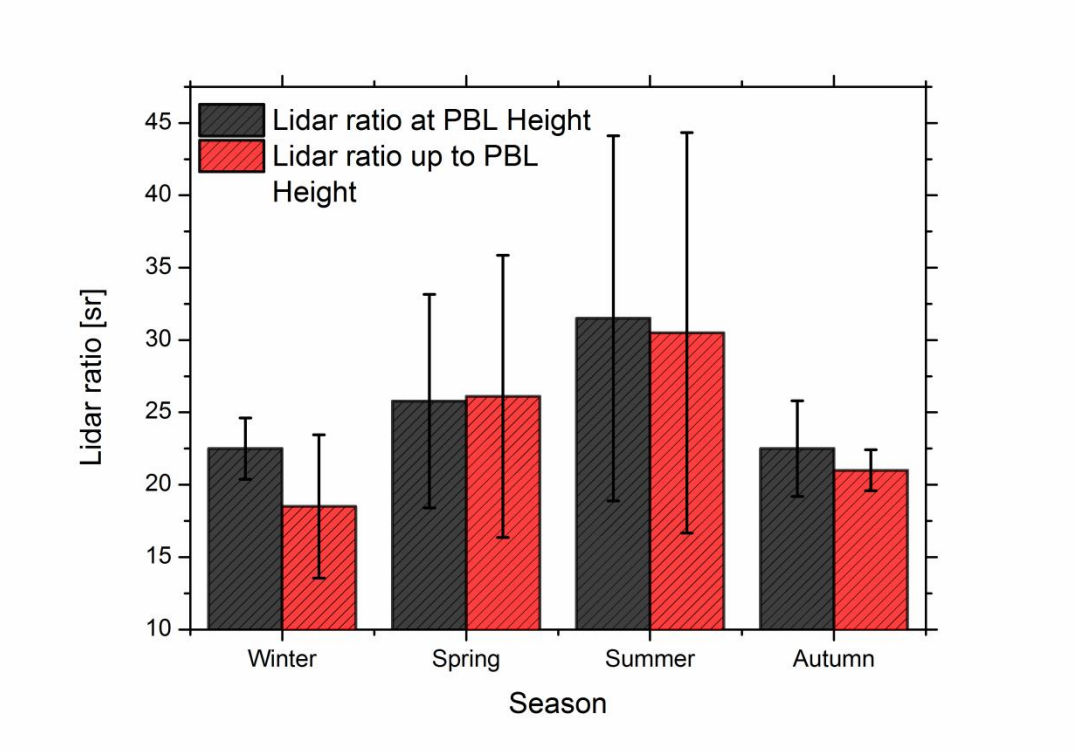


Figure 24. Average seasonal lidar ratio measured at the Cork site. Black - lidar ratio at the PBL height and red - lidar ratio from ground to the PBL height. Error bars indicate the 1σ weigh standard deviation of the average.

Mean seasonal Raman backscatter profiles measured at the Cork site are shown in Figure 25. Winter and autumn show clean conditions, with autumn exhibiting a somewhat larger backscatter coefficient within in the first 2 km. The mean Raman backscatter profile for spring exhibits a larger backscatter coefficient between 1 - 1.5 km compared to the average backscatter coefficient in the summer. This could indicate less mixing of aerosol during spring time (i.e. fixed layers form) compared with more dispersion of aerosol during summer time. Raman backscatter coefficients measured at Cork are similar to those measured at Aberystwyth [100].

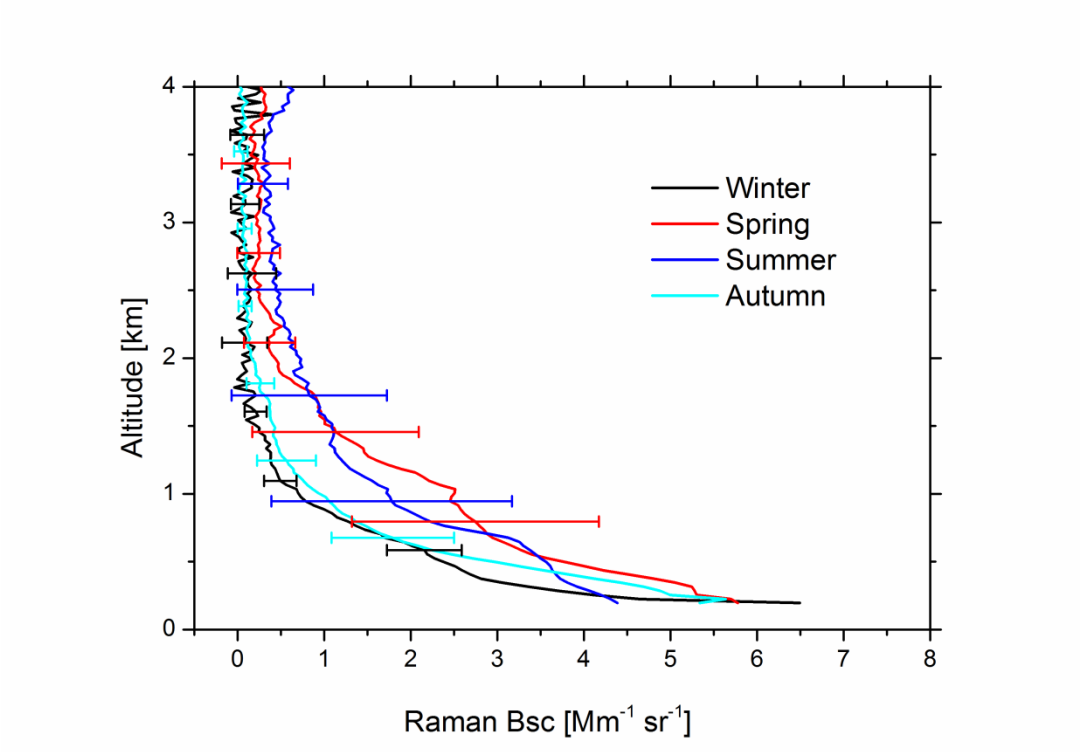


Figure 25. Mean seasonal Raman backscatter coefficients measured at the Cork site. Black - winter, red - spring, blue - summer and cyan - autumn. Error bars represent the 1σ standard deviation of the average shown for selected altitudes.

General conditions for backscatter lidar research at Cork

The location of the Cork lidar is of noteworthy benefit to the EARLINET and ACTRIS networks concerning its geographic location in the north-west of Europe. Typical aerosol scenarios are largely influenced by air masses from North America, Northern Europe and depending on transport conditions also North Africa and Western Europe. It is worth noting that Ireland is also a potential entry point for air-masses from Iceland in case of volcanic activity as encountered in 2010. However, weather conditions in Cork can be adverse when it comes to a high frequency of lidar operation. Generally, the climate in Cork is mild but changeable with a lot of rainfall and a lack of temperature extremes. Cork Airport records an average of 1194.4 millimetres of precipitation annually [94]. There are on average 151 days a year with more than 1 mm of rainfall, of which there are 75 days with rain over 5 mm [94]. Cork is generally foggy, with an average of 100 days of fog per year, typically occurring in the morning and winter. The yearly average of sunshine is 3.8 hr per day, with 69 days where no sunshine was recorded [94]. The yearly average wind speed is 9.2 ms^{-1}, while the most frequent wind directions are West, West South West, South South West and North North West (see

Figure 26, which shows the wind direction and frequency of wind speeds in the Cork region from January 2010 to May 2012). The mean relative humidity for an average year is recorded as 85 % and on a monthly basis it ranges from 78 % in May to 90 % in October and November [94].

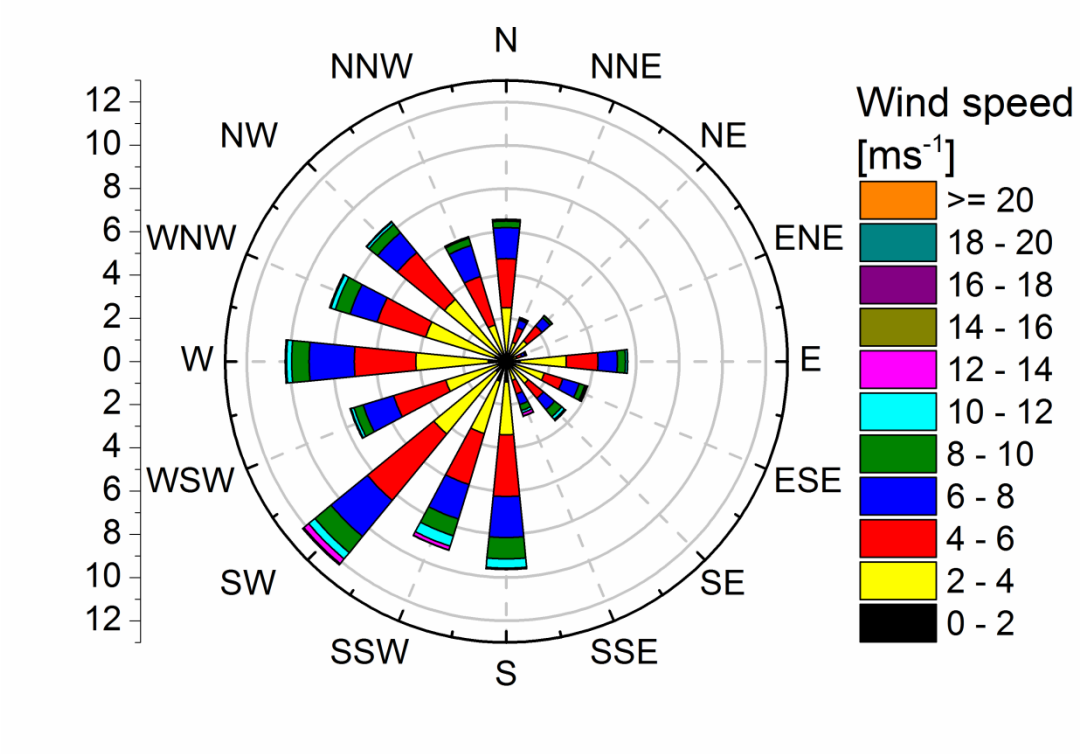


Figure 26. Summary of wind direction and frequency of wind speeds from 1 January 2010 to 30 April 2012 for the Cork region. Axes on the left represent the fraction of wind speeds that occurred in a certain direction in percent, e.g. ca. 12% of all wind direction are from the South West in said period. The colour plot on the right represents the wind speed, e.g. for the SW direction ca. 4% of the wind had a speed between 2-4 ms^{-1} (yellow), ca. 4% between 4-6 ms^{-1} (red), ca. 2% between 6-8 ms^{-1} (blue) and so forth. Data provided by Met Éireann [94].

Relevant for a lidar station is the level of cloud cover[3]. Figure 27 shows the frequency of hourly cloud cover distributed by different cloud levels over Cork airport from 1 January 2010 to 30 April 2012. Table 6 show the number of hours categorised by different cloud cover levels over Cork airport from said period. For climatological measurements the typical averaging time is 30 minutes, if cloud is present during a measurement, it can be removed during analysis, up to a maximum of 50%. Based on the typical cloud cover from Figure 27 ca. 75% of potentially EARLINET measurements are affected by more than 50% cloud cover.

[3] 0 oktas = clear sky, 4 oktas = sky half covered in cloud, 8 oktas = completely overcast

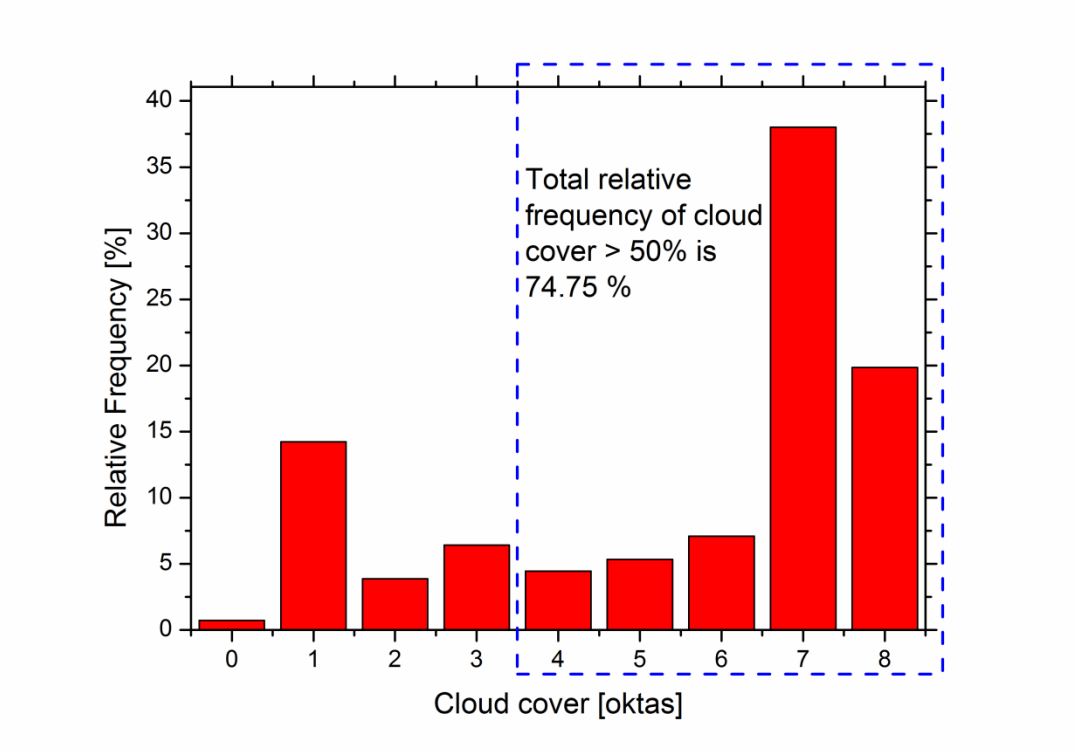


Figure 27. Relative frequency of hourly cloud cover over Cork. Blue dashed line indicates when the amount of cloud cover is more than 50 %. The total relative frequency for more than 50% cloud cover is ca. 75%.

Table 6. Number of hours categorised by different cloud cover over Cork airport from 1 January 2010 to 30 April 2012, total number of hours 20425.

Cloud cover (oktas)	0	1	2	3	4	5	6	7	8
Number of hours	149	2907	793	1309	911	1088	1449	7765	4054

4.2. Volcanic ash event – Eyjafjallajökull

In spring 2010 a strong eruption of the volcano Eyjafjallajökull in Iceland occurred. The eruption can be divided into two activity phases: The first was an effusive eruption, characterised by alkali-olivine basalt lava flowing from various eruptive vents. This phase lasted from 20 March to 12 April [101, 102]. Effects from the effusive eruption where localised to Iceland. On 14 April 2010 the volcano enter the second phase, explosive eruption, which occurred beneath glacial ice [101, 102]. Cold water from melted ice quickly chilled the lava causing it to fragment into highly abrasive glass particles that were then carried into the eruption plume. This injected a glass-rich ash plume into the into the south-easterly moving Jet Stream[4] [103, 104]. The location of this eruption directly under the Jet Stream caused the ash to be transported into the airspace over northern and central Europe a region with the highest density of air traffic in the world [103]. From 14 to 20 April ash covered large areas of northern Europe which forced many countries to close their airspace for all air traffic [105]. In October 2010 the volcano returned to dormancy and the eruption was considered to be over [102].

During phase two, volcanic particles were observed and monitored by various ground based means throughout Europe. The following is a summary of locations where observations have been published in peer-reviewed literature: Central Europe [69, 106-109], France [110], UK [107], Poland [111] Switzerland [112] Norway [106], Italy [108, 113, 114], Iberian Peninsula [115] and East Mediterranean Europe [116]. Findings from EARLINET stations have also been published [44], where quantitative data about the presence, altitude and layering of the volcanic plume are discussed.

It must be noted that measurements presented in section 4.1 were performed using the "old" system configuration as listed in Table 1. The system was undergoing the upgrade when the volcano eruption occurred, thus the Raman channel was unavailable as the PMT was not operational. Results presented in this section, are the 532 nm backscatter profiles determined using the Klett method as outlined in section 2.2. Observations were made in the period of 21 April to 7 May. Using an estimated lidar ratio for ash particles and the measured Klett backscattered profiles it is possible to calculate

[4] Jet streams are fast flowing, narrow air currents found in the Earth's atmosphere. Jet streams are caused by a combination of a planet's rotation on its axis and atmospheric heating (both by the sun and the Earth's core) [102].

extinction profiles and AOD values for the ash plume. This is discussed after presenting the Klett solutions of data measured at the Cork site. Table 7 summarizes measurements between 21 April and 7 May 2010 for which Klett backscatter profiles could be calculated (only 43 % of the measurements provided suitable data for analysis). Figure 28 shows the cloud cover (black, circle) and daily rainfall (blue, bar) from the 21 April to 7 May 2010.

Table 7. Summary of measurements made and suitable data available for analysis during the Eyjafjallajökull eruption in 2010.

Date	Measurement performed	Klett Profile calculated	Weather
21/04/2010	Yes	Yes	Cirrus
22/04/2010	Yes	Yes	Clear
23/04/2010	Yes	No	Low cloud
24/04/2010	Yes	No	Low cloud/rain
25/04/2010	No	No	Low cloud
26/04/2010	No	No	Low cloud
27/04/2010	No	No	Low cloud
28/04/2010	No	No	Low cloud/rain
29/04/2010	No	No	Low cloud
30/04/2010	No	No	Low cloud
01/05/2010	No	No	Low cloud/rain
02/05/2010	No	No	Low cloud
03/05/2010	No	No	Low cloud
04/05/2010	Yes	No	Low cloud
05/05/2010	Yes	No	Low cloud
06/05/2010	No	No	Low cloud
07/05/2010	Yes	Yes	Clear

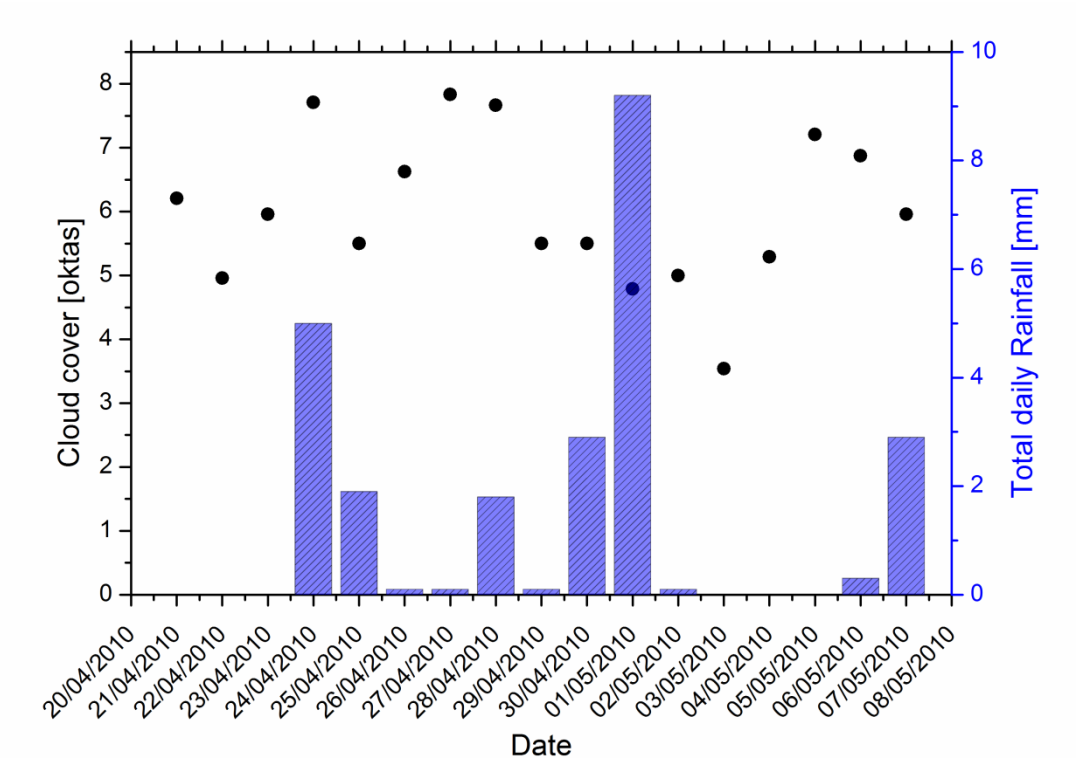


Figure 28. Cloud cover (black, circles) and total rainfall (blue, bar) from 21 April to 7 May. Weather conditions allowed for 7 days of lidar measurements over this period, with only 3 days for which Klett backscatter profiles could be established.

Mona at al. [113] describe a technique whereby all data submitted to the EARLINET database from 19 April to 14 May were analysed to provide an overview of volcanic layer identification and aerosol type assignment for said period. By applying the methodology described in Mona et al. [113] to all EARLINET observations of the volcanic event, quantitative information about the four-dimensional distribution of the volcanic plume at continental scale can be obtained. The observations of the volcanic plume made with UCLID were used in the four-dimensional distribution of the volcanic plume [44].

It is not possible to determine what type of aerosol particles are present using a single wavelength, therefore additional sources of information were required to confirm the presence of volcanic particles. In order to determine where the air masses arriving at Cork had originated backward trajectories were calculated using the HYSPLIT (HYbrid Single-Particle Lagrangian Integrated Trajectory) model [117] which is based on GDAS (Global Data Assimilation System - http://ready.arl.noaa.gov/gdas1.php) meteorological data. Satellite images provide by NASA/MODIS (MOderate Resolution Imaging Spectroradiometer) Rapid Response Team were also used to confirm the

presence of volcanic aerosol over Cork (http://earthdata.nasa.gov/data/nrt-data/rapid-response/).

In addition to these sources, forecasted graphics from the Met Office London Volcanic Ash Advisory Centres (VAAC) provided estimations of the movement of the volcanic ash plume. The forecast is generated with the Numerical Atmospheric-dispersion Modelling Environment [118] (NAME) which uses the Met Office Unified (MetUN) Model [119] and European Centre for Medium-range Weather Forecast (ECMWF) Numerical Weather Prediction (NWP) meteorology data - http://www.ecmwf.int/. The graphics usually provide up to 24 hours forecasts for airports and aviation authorities in order to support the decision making process on whether aircrafts can fly safely. The graphics consists of 4 panels (see Figure 33, Figure 37 and Figure 41), corresponding to predictions of ash clouds at 6 hour increments. The red line shows the regions for which ash has been predicted between the heights SFC-FL200 (surface to flight level 20000 ft). The green line indicates regions for ash being predicted between the heights FL200/FL350 (flight level 20000 ft to 35000 ft).

Brief discussion of individual days during the eruption period

21 April 2010

Figure 29 and Figure 30 are backscatter profiles for 21 April 2010. The panels (a), (b), (c) and (d) in both figures represent the time period used to determine the Klett backscatter profile, panel (a) 20:30 - 21:30, panel (b) 21:30 – 22:30, panel (c) 22:30 – 23:30 and panel (d) 23:30 – 00:30, all profiles are averaged over 1 hour periods. Figure 29 shows the backscatter profiles up to 12 km to illustrate the detection of a cirrus cloud (descending from 6 km to 4.5 km), while Figure 30 shows the lower 3 km of the backscatter profiles. No overlap function is available to correct the first 1 km of the profiles in Figure 29 and Figure 30, hence a larger error is expected. The top of the PBL height for panel (a), (b), (c) and (d) was determined to be 465 ± 30 m, 585 ± 30 m, 405 ± 30 m, and 585 ± 30 m respectively (average height of PBL 510 ± 90 m). The PBL height was calculated using the 1st derivative of the backscatter coefficient as described in [120]. The top of the PBL was found at the altitude of the steepest gradient of the particle backscatter profile, i.e., the largest local minimum of the first derivative of the range-corrected signal.

Figure 30 shows a layer was measured between 750 m and 1500 m. According to the HYSPLIT model (Figure 31 (left)), the air masses probed at 500 m (red line) and 1000 m (blue line) on 21 April had originated from Iceland, while the air masses at the altitude of the cirrus cloud originated over the Atlantic Ocean (green line). Figure 31 (right), shows an image captured with the MODIS instrument on NASA's Terra satellite from 20 April 2010. The ash plume (inside the red line) is apparent and drifting to the south. This observation agrees with the HYSPLIT model. Figure 32 is the colour-coded image of time-dependent range corrected 532 nm backscatter profiles. The ash layer between 750 m and 1400 m and the planetary boundary layer (PBL) at ca. 500 m are evident in this image.

Additional evidence that the layer detected in the lower troposphere above Cork, consisted of ash particles is shown in Figure 33. This VAAC prediction graphic shows the expected ash coverage at 6 hour intervals in four panels (Figure 33 a, b, c and d). The model indicates that the ash was expected to cover all of Ireland's troposphere, but could only estimate the tropospheric position of the ash to be somewhere between ground level and ~6 km. Based on the backscatter signal (Figure 30) the ash layer was confirmed to be between 0.8 km to 1.4 km.

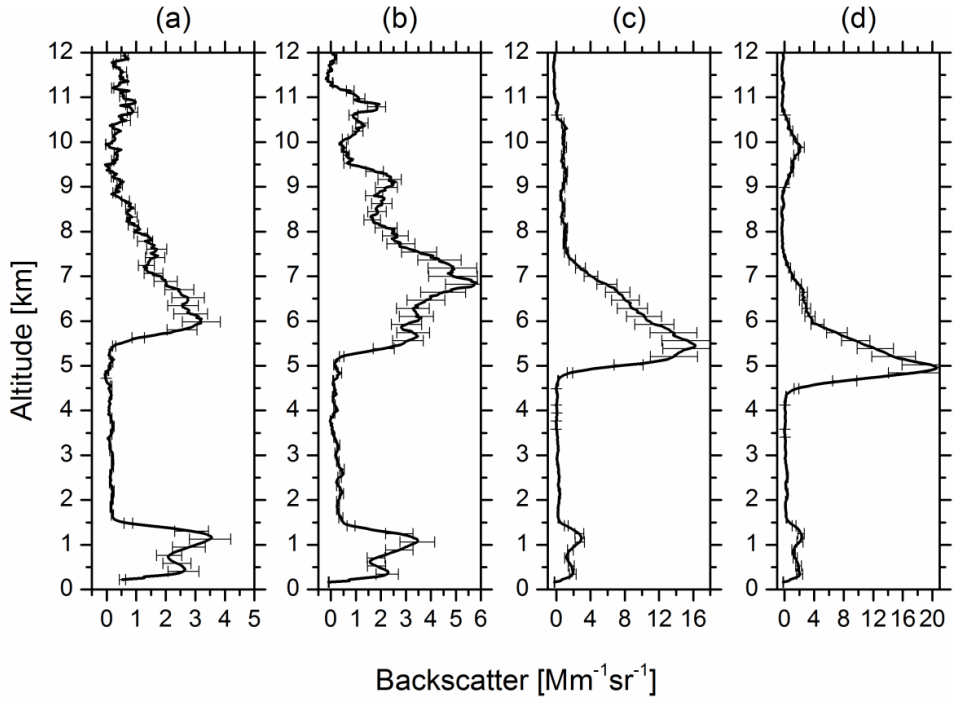


Figure 29. Backscatter profiles determined using the Klett method for 21 April 2010. The panels (a), (b), (c) and (d) are profiles averaged from 20:30 - 21:30, 21:30 – 22:30, 22:30 – 23:30 and 23:30 – 00:30 respectively A descending cirrus cloud is apparent in the sequence of panels between 4.5 and 8 km . Aerosol of volcanic origin was observed between 750 m and 1500 m.

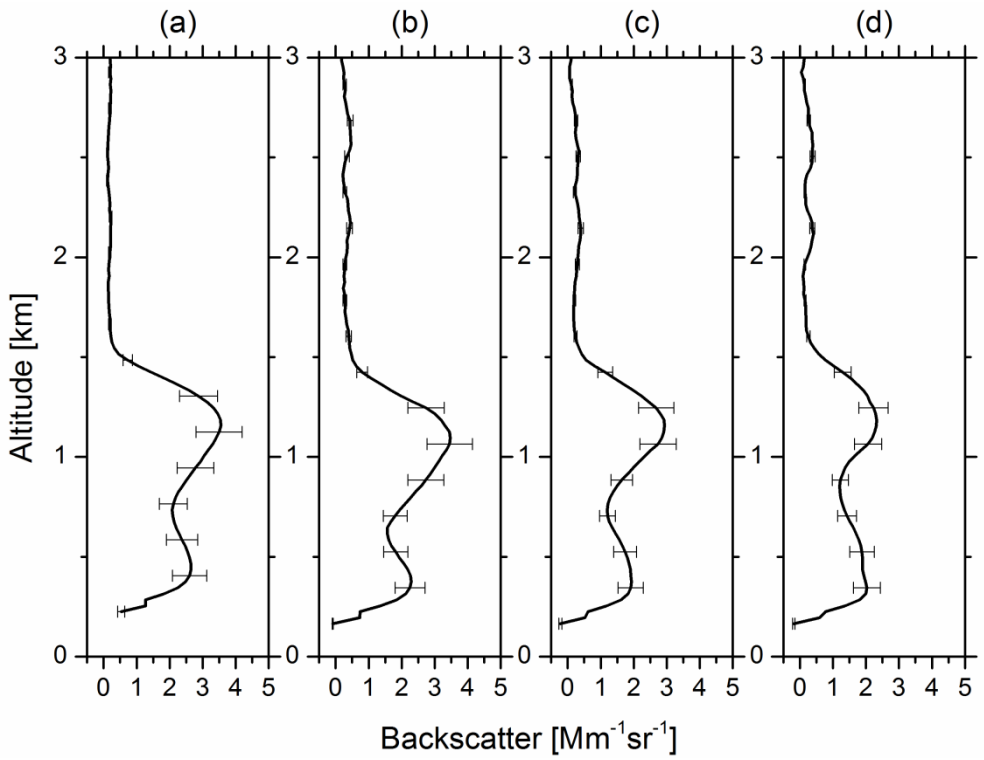


Figure 30. First 3 km of the backscatter profiles determined using the Klett method for 21 April 2010. The panels (a), (b), (c) and (d) are profiles averaged from 20:30 - 21:30, 21:30 – 22:30, 22:30 - 23:30 and 23:30 – 00:30 UTC respectively. The average top height of the PBL was determined to be 510 ± 90 m, the volcanic particles were observed between 750 and 1400 m.

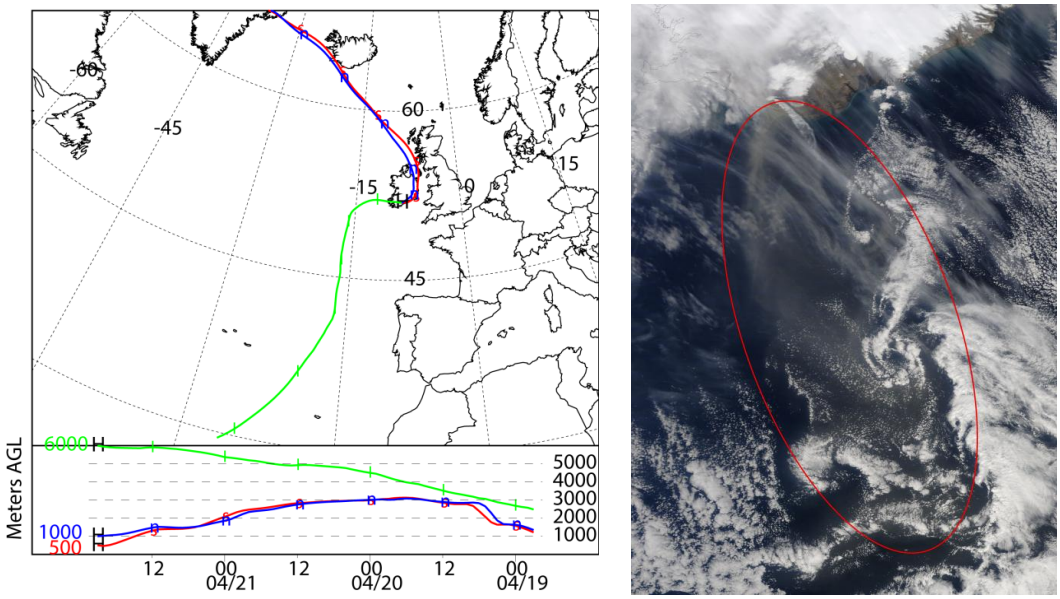


Figure 31. Left: NOAA HYSPLIT model backward trajectories for three days before 21 April. Trajectories indicate air masses arrived at Cork from Iceland (blue and red traces). Right: Image from the MODIS instrument on NASA's Terra satellite that captured an visible image of the ash (inside red line) drifting south and east from the Eyjafjallajökull volcano in Iceland on 20 April 11:55 UTC [28].

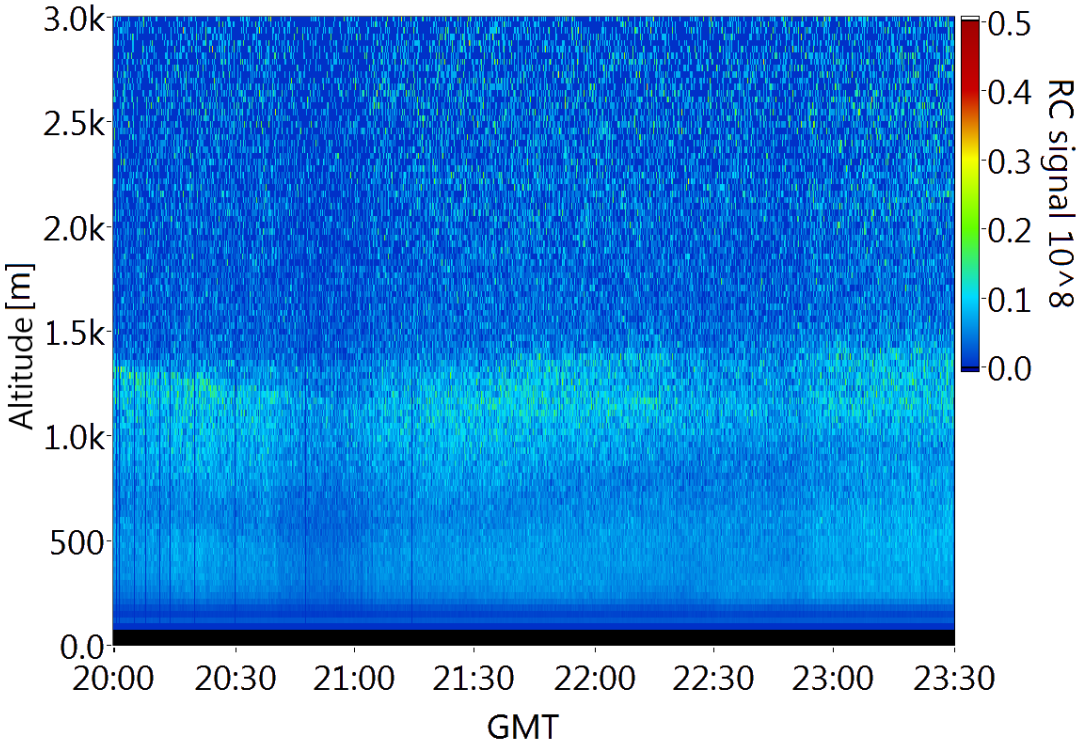


Figure 32. Colour-coded image of time-dependent range corrected 532 nm backscatter profiles of the measurement on 21 April. The ash layer is evident between 750 m and 1400 m.

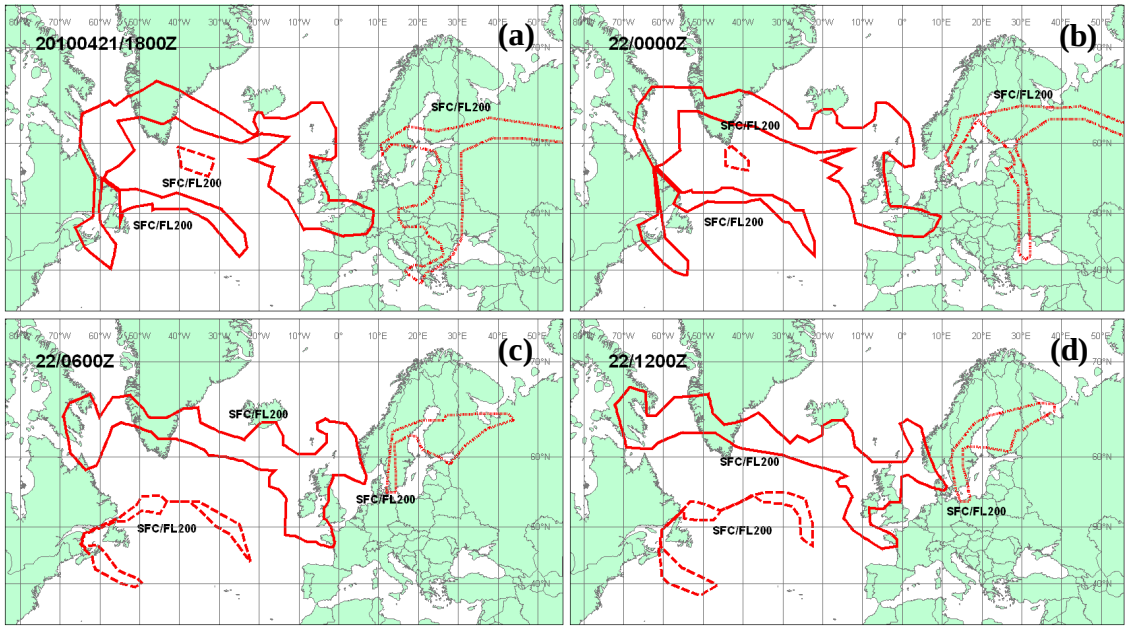


Figure 33. The VAAC prediction graphic released on 21 April 2010 18:51 UTC. All ash clouds are estimated to be between ground level and 6 km (Red line - SFC/FL200) [121].

22 April 2010

Figure 34 shows the Klett backscatter profiles from 0 to 3 km for 22 April 2010. The panels (a), (b) and (c) represent the time period used to determine the Klett backscatter profile, panel (a) 20:00 - 21:00, panel (b) 21:00 – 22:00 and panel (c) 22:00 – 23:00, all profiles are averaged over these 1 hour periods. No overlap function is available to correct the first 1 km of the profiles, hence a larger error is expected. The left panel of Figure 35 shows the HYSPLIT model backward trajectories for three days before 22 April. According to the model the air masses originate from Iceland and pass over England (red and blue lines). The right panel of Figure 35 illustrates that on 22 April the ash density had diminished in comparison to 20 April (shown in Figure 31 (right panel)). The amount of volcanic material injected into the atmosphere had started to decrease by 22 April. Comparing the backscatter profiles in Figure 30 with Figure 34, the ash layer was measured at ca. 3.5 $Mm^{-1}sr^{-1}$ for 21 April and ca. 2.5 $Mm^{-1}sr^{-1}$ for 22 April, confirming the reduction of ash particles in the lower troposphere. This is also evident in the VAAC prediction model, Figure 37, where the predicted ash in the troposphere over Ireland is receding. Figure 37, panel (a) predicts the ash cloud to be over Ireland, panel (b) predicts the ash cloud to move to the north, panel (c) predicts the ash cloud to be over Northern Ireland and panel (d) predicts no ash cloud over Ireland. While the model predicts diminishing ash occurrence for 22 April, this is not evident from the backscatter profiles in Figure 34, as the detected layer remains at ca. 2.5 $Mm^{-1}sr^{-1}$ during the 3 hr measurement period shown.

Figure 36 is the colour-coded image of time-dependent range corrected 532 nm backscatter profiles. The weak ash layer between 500 m and 1200 m and the planetary boundary layer (PBL) at ca. 450 m are evident in this image.

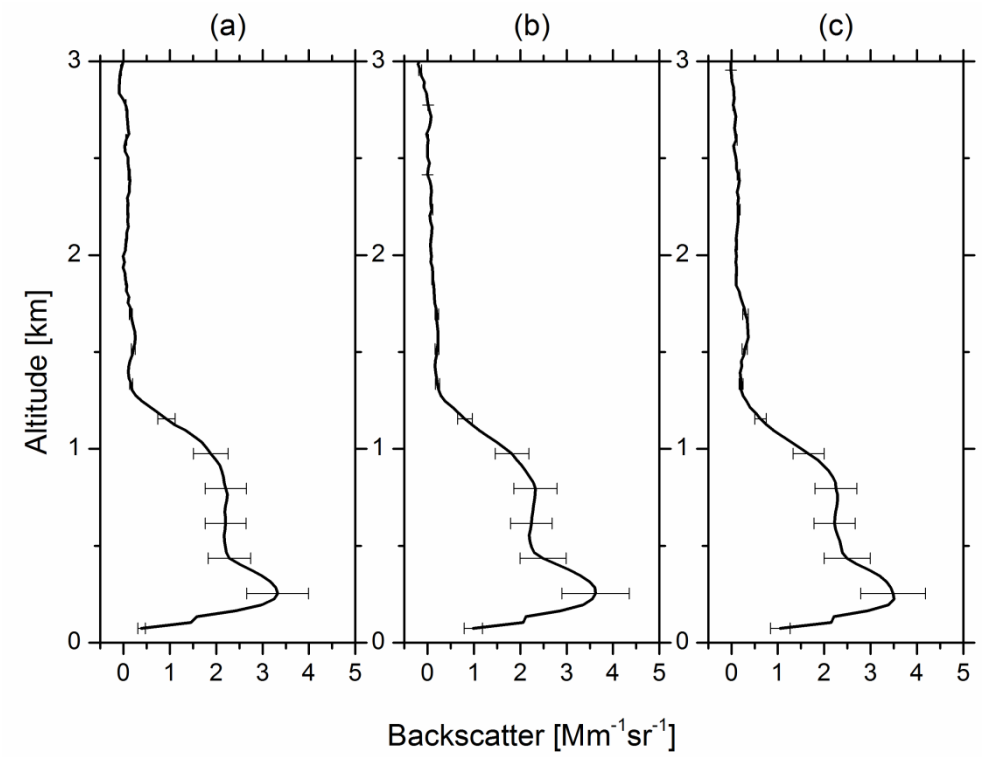


Figure 34. Backscatter profiles determined using the Klett method for 22 April 2010. The panels (a), (b) and (c) are profiles averaged from 20:00 - 21:00, 21:00 – 22:00 and 22:00 - 23:00 UTC respectively. The average top height of the PBL was determined to be 485 m ± 46 m, the volcanic particles were observed between 500 m and 1200 m.

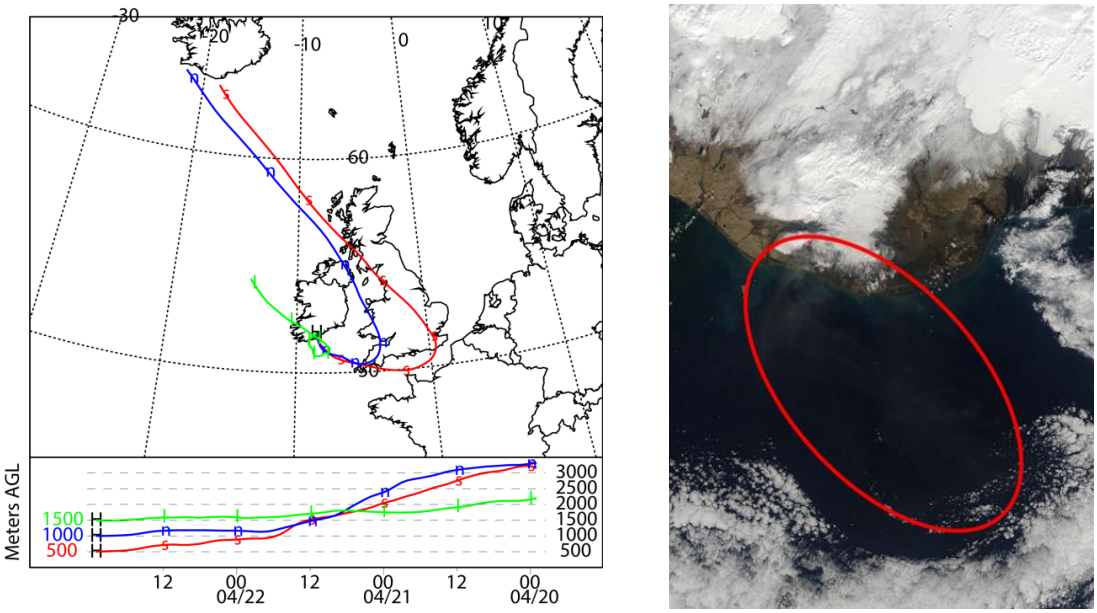


Figure 35. Left: NOAA HYSPLIT model backward trajectories for three days before 22 April. Trajectories indicate air masses arrived at Cork from Iceland having passed over England. Right: Image from the MODIS instrument on NASA's Terra satellite that captured an image of the much diminished ash occurrence (inside red line) drifting south and east from Eyjafjallajökull volcano on 21 April 12:35 UTC [28].

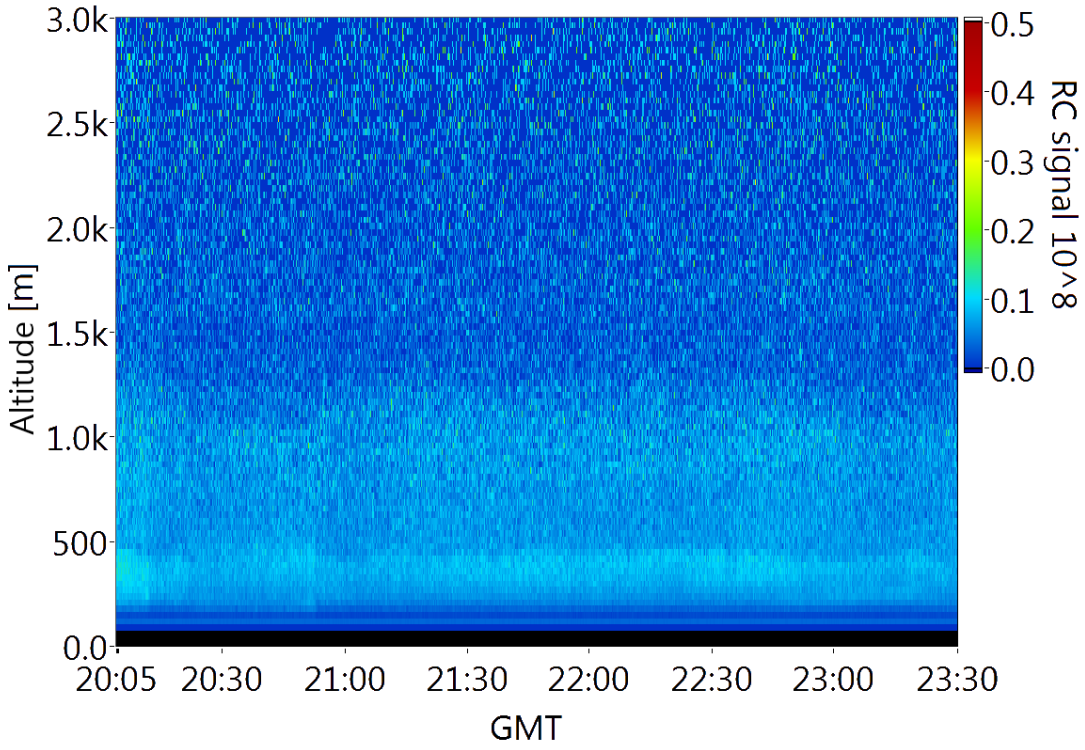


Figure 36. Colour-coded image of time-dependent range corrected 532 nm backscatter profiles of the measurement on the 22 of April. The weak ash layer is evident between 500 m and 1200 m.

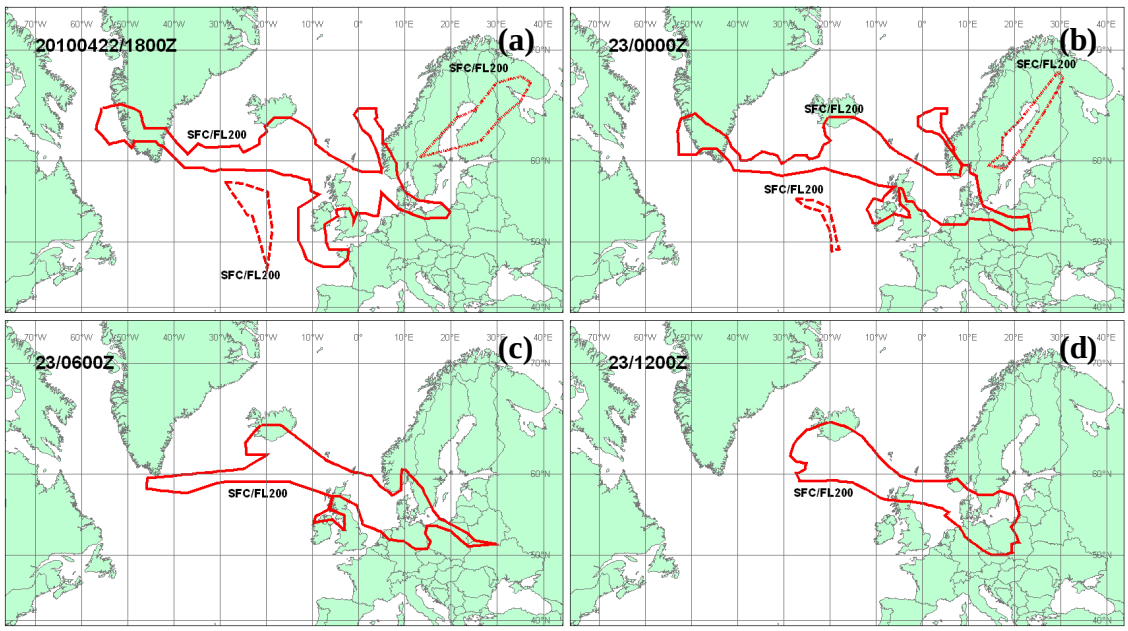


Figure 37. The VAAC prediction graphic released on 22 April 2010 19:38 UTC. All ash clouds are estimated to be between ground level and 6 km (Red line - SFC/FL200) [121].

7 May 2010

The final detection of volcanic particles over Cork was made on 7 May. Figure 29 shows a 1 hr averaged Klett backscatter profile from 20:30 to 21:30 UTC. Larger errors up to 1 km are expected as no overlap correction was available. There are several layers present above the top of the PBL (PBL height 735 ± 30 m) in the lower troposphere at 1.2 km, 1.6 km, 2.2 km and 2.9 km. The VAAC prediction graphic, Figure 41, predicts the ash to be present over the north and east of Ireland; according to the HYSPLIT model air masses originate from over central England and Northern Europe where no ash occurrence was indicated by the information from VAAC. As discussed in Matthias et al [109], between 2 and 5 May England was largely influenced by stronger ash occurrences (seen in Fig. 2c and 2d in [109]). The findings in [109] support the HYSPLIT model, that air masses with ash particles were transported over Ireland and were detected on 7 May. More than one layer is present between 1 km and 3 km as opposed to the backscatter signals from the 20 and 21 April where only single layers above the PBL were observed. The backscatter profile for 7 May suggest a stronger backscatter coefficient than previous ash measurements (3.5 $Mm^{-1}sr^{-1}$ in comparison with Figure 30 - 3 $Mm^{-1}sr^{-1}$ and Figure 34 - 2.5 $Mm^{-1}sr^{-1}$), indicating a greater concentration of ash particles.

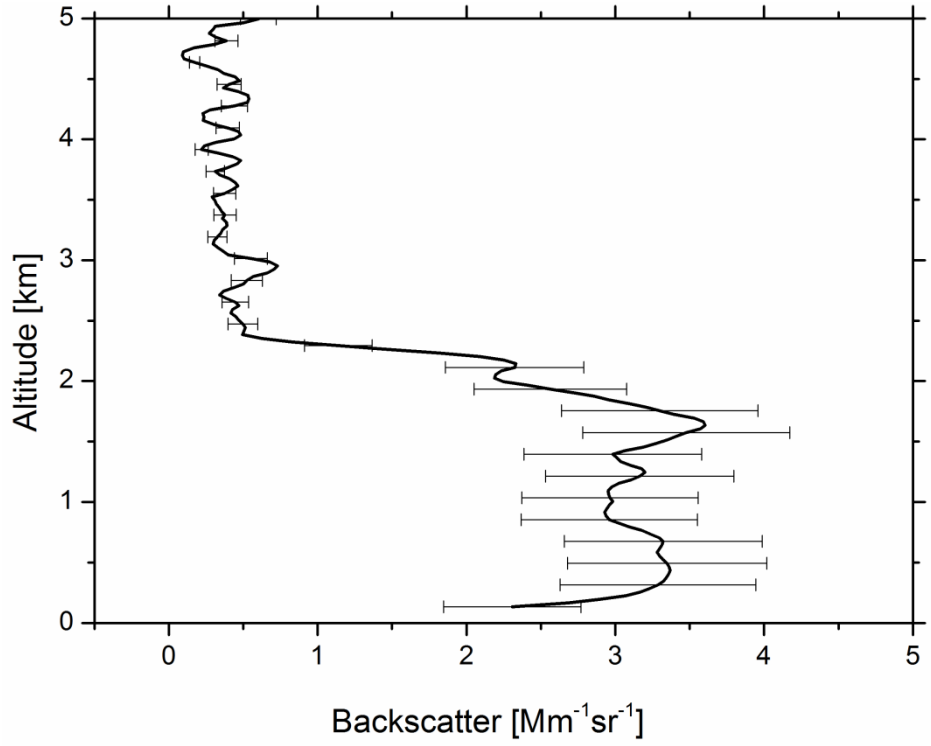


Figure 38. Backscatter profile determined using the Klett method for 7 May 2010 averaged from 20:30 – 21:30 UTC. The top of the PBL was determined to be at 735 ± 30 m, the volcanic particles were observed between 1 and 3 km. Mixing with aerosol in the PBL is evident.

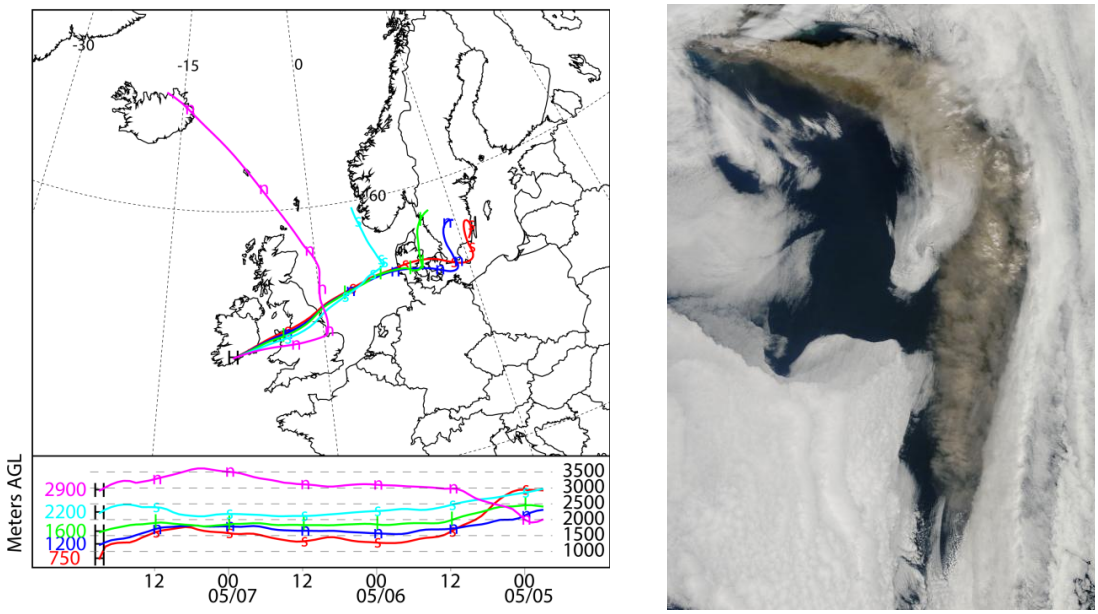


Figure 39. Left: NOAA HYSPLIT model backward trajectories for three days before 7 May. Trajectories indicate air masses arrived at Cork from over central England and Northern Europe. Right: Image from the MODIS instrument on NASA's Terra satellite of a substantial ash plume drifting east and then south over the Northern Atlantic starting from the Eyjafjallajökull volcano in Iceland on 6 May 11:55 UTC [28].

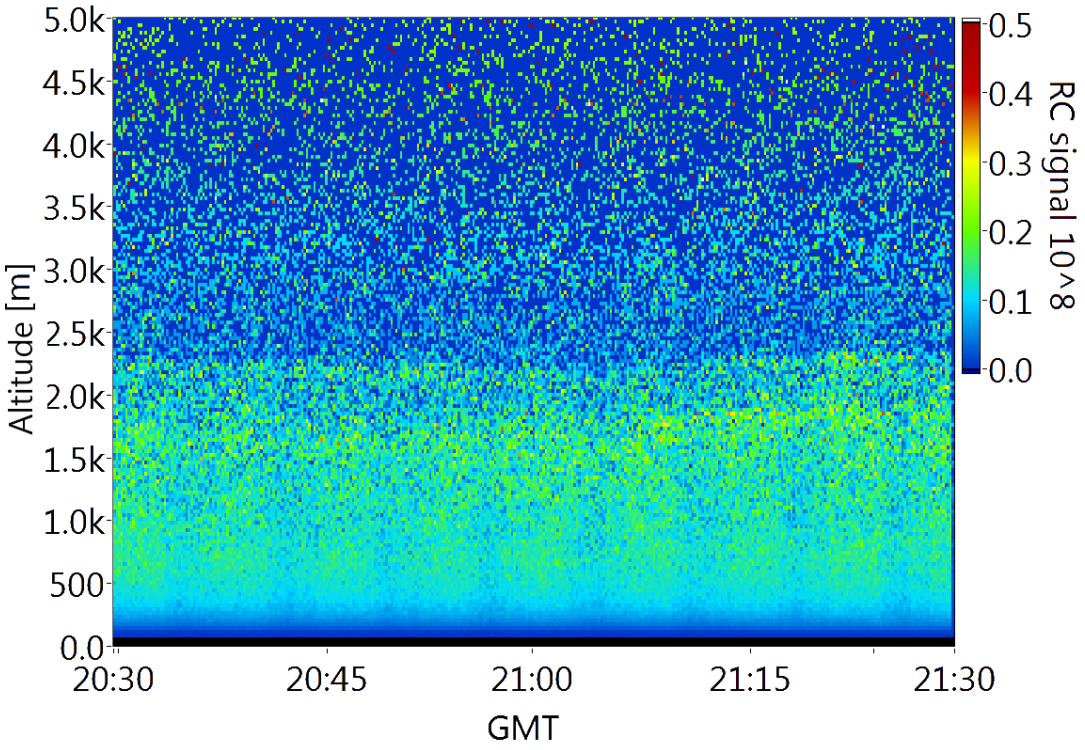


Figure 40. Colour-coded image of time-dependent range corrected 532 nm backscatter profiles of the measurement on the 7 of May. The ash layer is evident between 1 km and 2.3 km.

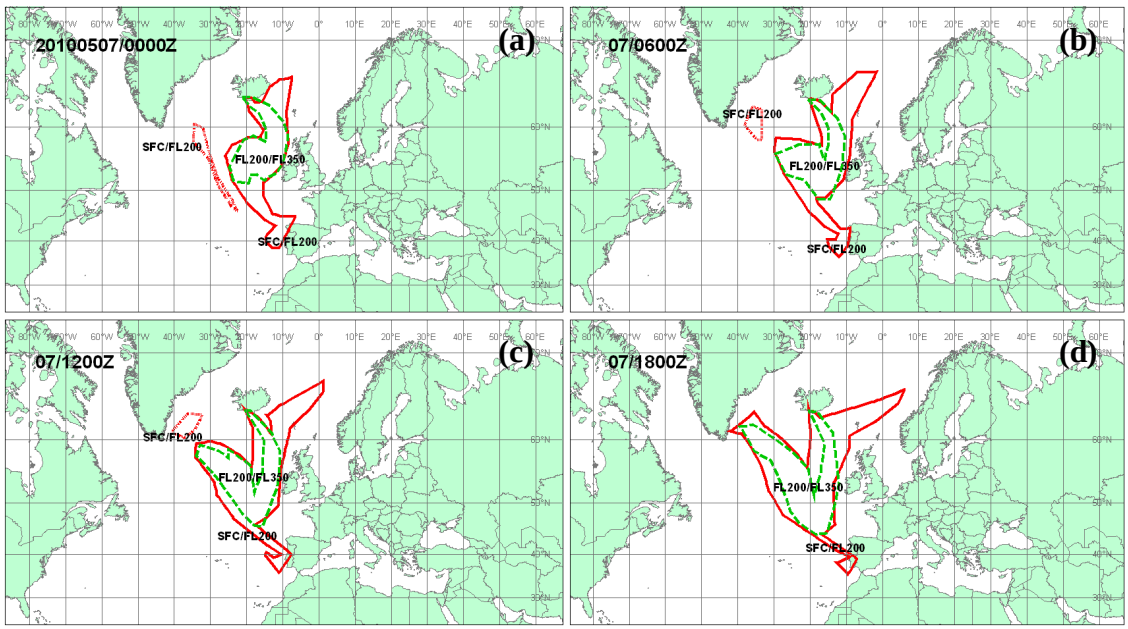


Figure 41. The VAAC prediction graphic released on 7 May 2010 00:27 UTC. Occurrence of ash was estimated to be between ground level and 6 km (Red line - SFC/FL200) and between 6 and 10.5 km (Green line – FL200/FL3500) [121].

Estimated extinction coefficients and aerosol optical depth (AOD)

Since there were Raman scattering profiles available for this period of measurements, a lidar ratio value for the ash particles was assumed to calculate an extinction profile and AOD value from the backscatter signal [122]. Based on data from the lidar station in Munich where the lidar ratio for the ash layer was found to be between 50 - 60 sr at 532 nm [68], a lidar of 55 ± 5 sr was used to calculated the extinction profiles. The uncertainty for the extinction profiles will be determined by error propagation due to the error of the backscatter coefficient profiles and the range of the lidar ratios determined in Munich. Table 8 shows the maximum extinction coefficient, mean extinction coefficient and the AOD of the ash layers measured at the Cork site.

Table 8. Maximum and average extinction coefficient of the ash layer calculated from the measured Klett backscatter profiles and the assumed lidar ratio of 55 ± 5 sr for ash particles [68]. Errors for the mean ExtCf indicate the standard deviation of the mean, all other errors determined by error propagation.

	Maximum ExtCf [Mm^{-1}]	Mean ExtCf [Mm^{-1}]	AOD [1]
21 April	195 ± 41	149 ± 30	0.122 ± 0.400
22 April	152 ± 35	115 ± 22	0.090 ± 0.038
7 May	218 ± 44	170 ± 19	0.215 ± 0.080

The ash layers detected on 21 and 22 April are optically thinner than the one on 7 May. Ansmann et al. [68] report the extinction coefficients of 400 Mm^{-1} at the start of the eruptive period on 16 and 17 April. The authors reports AOD values for the same period to be 0.35 ± 0.05. Flentje et al. [123] report a measured extinction value of 500 Mm^{-1} on 17 April in Hohenpeissenberg, Germany. Since the ash measured at the Cork site had aged by ca. 5 days compared to the particles observed over Munich and Hohenpeissenberg, it was expected that the values determined at the Cork site would be smaller. Measurements in Southeastern Italy from 20 to 22 April show good agreement with the calculated extinction coefficients and AOD of the ash layer that was measured at the Cork site [124]. The authors report extinction values between ca. 100 and 150 Mm^{-1} and AOD values between 0.15 and 0.25 (Figure 4. and Figure 6. in ref [124] respectively). A different study by Mona et al. [113] in Southern Italy found the AOD at

355 nm to be ca. 0.12 - 0.13 on 20 April 2010, in similar to values found at the Cork site. Reports of AOD at 440 nm over the Iberian Peninsula vary from 0.17 to 0.31 over the period of 6 - 12 May 2010 [115], and agree with the AOD measured on 7 May at the Cork site.

A report by Marenco et al [125] compares an airborne lidar with a ground based lidar in the United Kingdom over the period 20 April to 18 May. Both instruments operate at 355 nm. From 20 April to 22 April the authors report no significant ash detection with the airborne lidar, from 4 May to 18 May ash at different heights and concentrations were detected. A maximum extinction value of 700 Mm^{-1} was measured on the 16 and 17 May, on the remaining days the extinction value varied between 100 to 400 Mm^{-1} [125]. On 4 May a direct comparison between the airborne lidar and ground based lidar at Aberystwyth is made [125]. Both lidars measured the main aerosol layer at the same altitude and the magnitude of the extinction coefficient is within 25% (ca. extinction value of 150 Mm^{-1}).

A study in France [110], reports on lidar observations at 355 nm from 18 to 22 April and 18 and 19 May 2010. The authors report a mean extinction of 369 ± 38 Mm^{-1} on 19 April, 275 ± 56 Mm^{-1} on 22 April, 502 ± 46 Mm^{-1} on 18 May and 927 ± 153 Mm^{-1} on 19 May. A stronger extinction is detected on the 22 April in France in comparison to the Cork site, the is likely due to the direction the air masses travelled (see Figure 35), the red and blue traces show that the air masses travelled over England and the English Channel before arriving at the Cork site. A smaller ash concentration was transported back to the Cork site after passing over English Channel, while the results presented in [110] would indicate that a larger concentration was transported over France. A comprehensive study by Toledano et al. [115] discuses the aerosol properties of the Eyjafjallajökull ash over the Iberian Peninsula on 6 to 12 May 2010. The authors report on findings from sun photometers and satellite observations. Values of AOD at 440 nm varied from 0.19 to 0.31 at 8 different sun photometers stations over said period. The MODIS satellite sensor measured values of AOD at 550 nm between 0.2 to 0.5 on 11 May and between 0.1 to 0.3 on 12 May [115]. A lidar study by Sicard et al. [126] of the Eyjafjallajökull ash over the Iberian discuses results over the from 5 to 8 May. The authors report mean maximum AOD over said period for Évora, Madrid, Granda and Barcelona to be 0.107, 0.130, 0.137 and 0.017, respectively. Backscatter profiles and extinction profiles are presented in Figure 5 (7 May 2010 - Évora and Madrid) and

Figure 6 (8 May 2010 - Granda and Barcelona) in ref [126]. The maximum backscatter and extinction value from Évora and Madrid is ca. 3 $Mm^{-1}sr^{-1}$ and 120 Mm^{-1}, respectively. While the maximum backscatter and extinction value from Granda is ca. 8 $Mm^{-1}sr^{-1}$ and 300 Mm^{-1}. The backscatter values from Évora and Madrid agree with those measured at the Cork site (Figure 29, Figure 34 and Figure 38), while the extinction values agree with values calculated from backscatter profiles at the Cork site (see Table 8).

Another rather comprehensive study by Matthias et al. [109] discusses results from sun photometers, lidars and in-situ aircraft observation from 11 AERONET station within Europe from 14 to 22 April. AOD values at 532 nm determined with lidars varied from 0.08 to 0.44. Extinction values of the ash layer were measured to be 700 Mm^{-1} at Hamburg and 500 Mm^{-1} at Leipzig on the 16 April. On 18 April the lidar station at Palaiseau measured extinction values of the ash layer to be 200 Mm^{-1} and the lidar station at Potenza shows a decrease to 50 Mm^{-1} on the 20 April.

Winker et al. [127] presents CALIPSO observations of Eyjafjallajökull ash between 15 and 20 of April. The CALIPSO satellite observed the volcanic plume over 12 different locations within Europe. The closet observation to the Cork site was made over the south eastern England (18 April) and North of Ireland over the Atlantic Ocean (19 April). A weak layer was detected on 18 April with an extinction value of 25 Mm^{-1} and AOD at 532 nm to be 0.024 and with an increase on 19 April with an extinction value of 67 Mm^{-1} and AOD at 532 nm to be 0.039. A measurement on 20 April south of Iceland show a larger extinction and AOD value of 248 Mm^{-1} and 0.29, respectively. This is in agreement with the calculated extinction values at the Cork site, where it would be expected to be of the same order of magnitude as the CALIPSO observation a day earlier than the first detection of ash particles at the Cork site.

4.3. Saharan dust events

In 2011 and 2012 Saharan dust events were detected during the spring season at the Cork site. Two separate events were detected on 8 and 21 April in 2011, and a continuous event was detected over four days from 26 to 29 March in 2012. To confirm that the aerosol loads over Cork were dust; measurements from Cloud-Aerosol Lidar Infrared Pathfinder Satellite Observations (CALIPSO) [61, 63] (where available) were used. The Cork lidar station is situated within 100 km of the orbital path of CALIPSO. The satellites orbital path can pass within the 100 km distance between 2 and 4 times a week, during day and night. A direct comparison cannot be performed as CALIPSO measurements occur between either: (i) ca. 01:00 to 04:00 where access to the lidar is unavailable or (ii) ca. 12:00 to 14:00 where no measurements were performed. Therefore CALIPSO data were used to provide meaningful information about the aerosol load (i.e. if dust particles were present) in the troposphere within a 100 km radius of the Cork site. In addition to CALIPSO observations, the Dust Regional Atmospheric Model (DREAM) [128] which forecast dust events was used to verify the presence of dust. The forecasts are available at http://www.bsc.es/projects/earthscience/DREAM. The Navy Aerosol Analysis and Prediction System (NAAPS) [129] long-range pollution transport model was developed by the Naval Research Laboratory in Monterey (NRL). The NAAPS model uses meteorological data obtained from the Navy Operational Global Atmospheric Prediction System (NOGAPS) global circulation model [130]. The images from the NAAPS model show the optical depth at a wavelength of 0.55 μm for three components: sulphate particles, dust, and smoke. Also backward trajectories of the air masses arriving at Cork on the dates concerned were determined using the HYSPLIT model [117] with GDAS meteorological data.

8 April 2011

Figure 42 shows an aerosol event detected at the Cork site on 8 April 2011. Panels (a), (b), and (c) show the extinction coefficient, the Raman backscatter coefficient and the lidar ratio as a function of altitude, respectively. The integration time was 30 minutes. The top of the planetary boundary layer was determined to be 615 ± 30 m. In Figure 43 (left panel) a backward trajectory (3 days) is shown as determined by the HYSPLIT model. The model implies that the air masses over Cork on that day arrived from the Atlantic Ocean and the Sahara desert. A large dust event was forecasted by the DREAM

model for the start of April 2011 (Figure 44). According to the model on 8 April dust was present over southern Spain, Portugal, northern France, the Atlantic Ocean and Ireland; these locations match with the blue and green traces on the HYSPLIT backward trajectory (see Figure 43 left). The forecast for the NAAPS model for 8 April at 08:15 (see Figure 43 right) confirms the presence of a dust in the lower atmosphere.

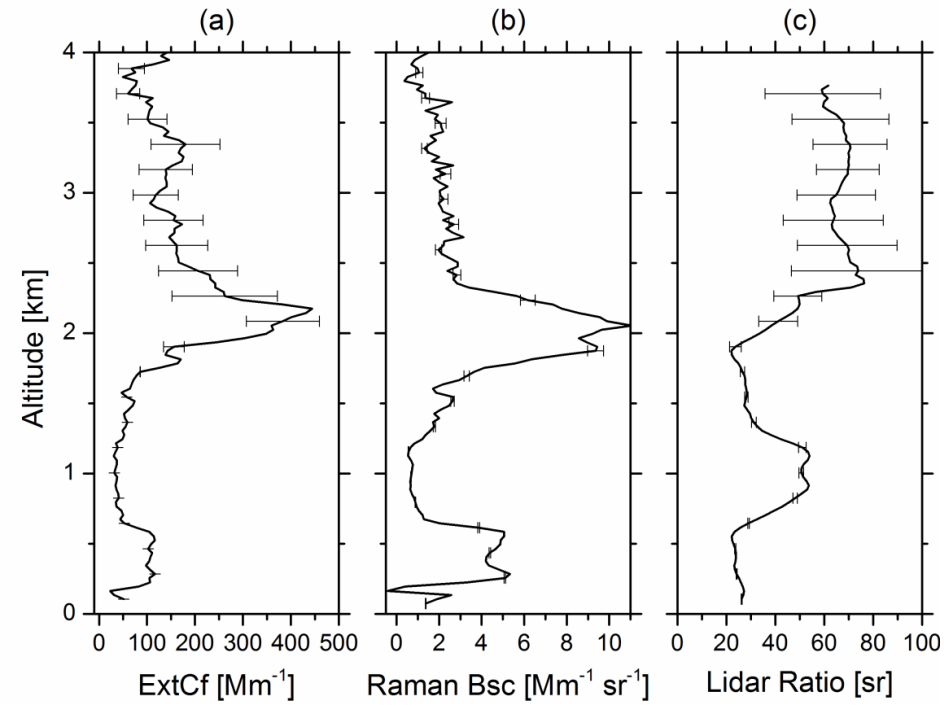


Figure 42. Measurement on the 8 April 2011 (2100-2130 hrs). (a): Extinction coefficient (ExtCf) with errors (signal smoothing with window lengths of 90 m up to 1230 m, 330 m between 1230 and 2490 m, and 810 m from 2490 m upwards), (b) Raman backscatter (Bsc) solution with errors, (c) Lidar ratio with a smoothing window of 210 m up to 2265 m and 570 m from 2265 m onwards. An aerosol layer is evident between 2 and 4 km with a lidar ratio between 20 and 65 sr. Error bars indicate the standard deviation caused by photon noise.

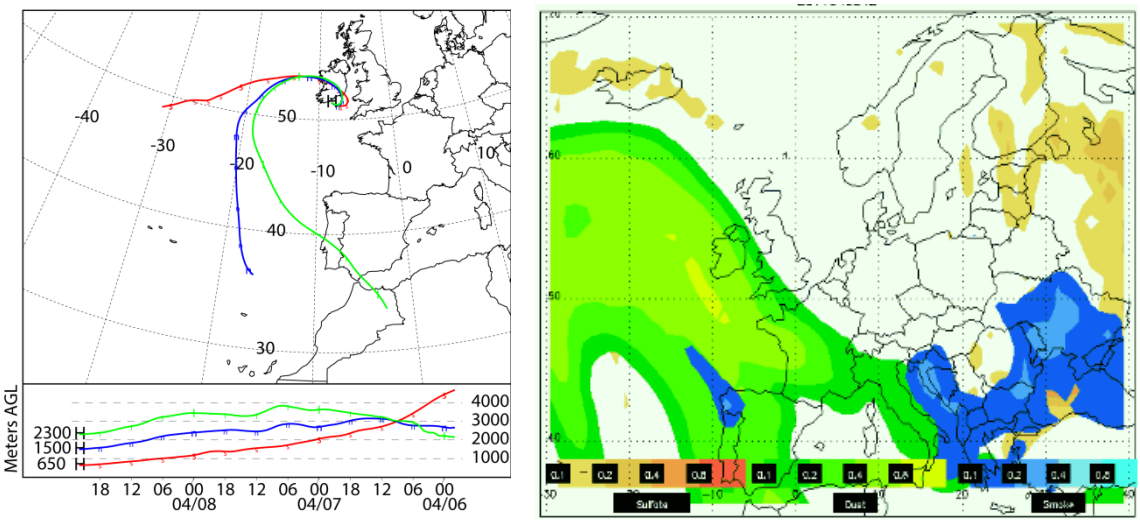


Figure 43. Left: NOAA HYSPLIT model backward trajectories for three days before 8 April. Trajectories indicate air masses arrived at Cork from the Atlantic Ocean and the Sahara desert. Right: NAAPS Aerosol Model for 8 April 2011. The colour code for different aerosol particles are: sulphate - orange to red, dust - green to yellow and smoke - blue. The model predicts a dust event over southern Spain, Portugal, France, Atlantic Ocean and Ireland [131].

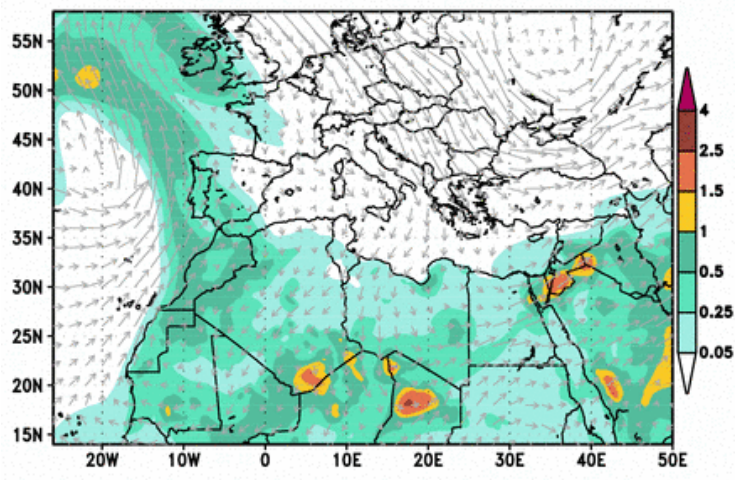


Figure 44. Dream model forecast for dust loading over North Africa, Middle East and Europe for 8 April (colour-coded unit: g/m^2). Wind directions are also indicated. A dust event was predicted over southern Spain, Portugal, northern France, Atlantic Ocean and Ireland as indicated by the image [132].

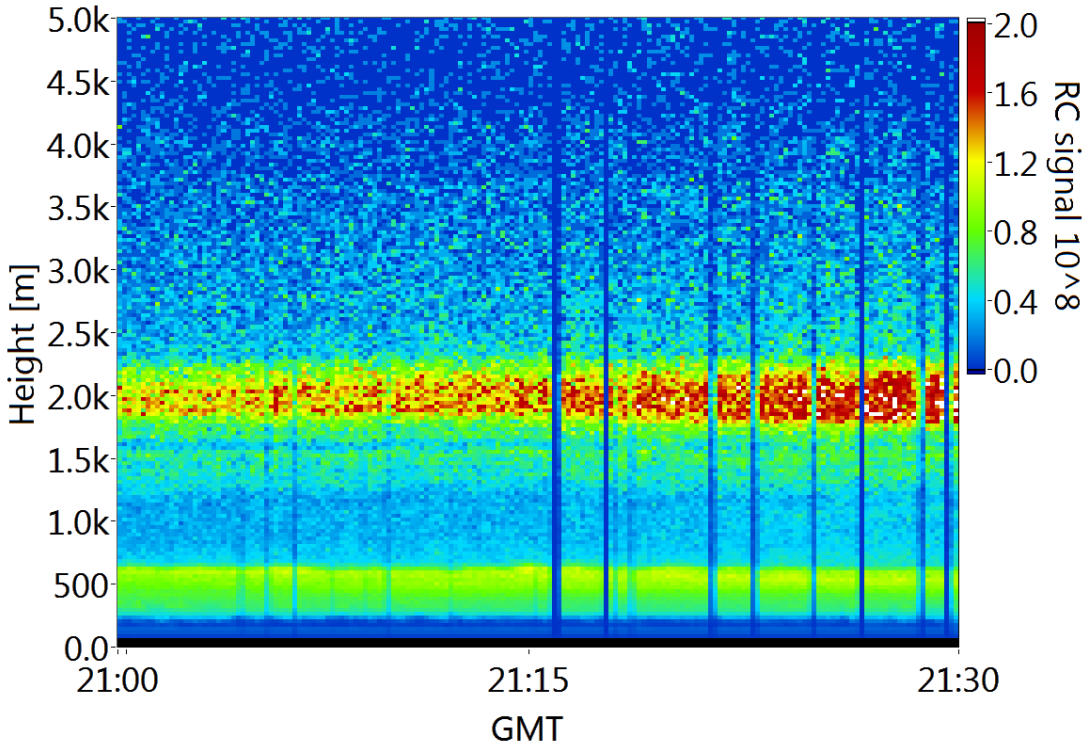


Figure 45. Colour-coded image of time-dependent range corrected 532 nm backscatter profiles of the measurement on 8 April for a 30 min period. A large aerosol layer is evident between 1.3 and 2.3 km.

Figure 46 shows the orbital projection of CALIPSO over Ireland for 8 April. The data presented in Figure 48 corresponds to the time shown in pink in Figure 46. Figure 47 shows the total attenuated backscatter for 8 April 2011, start time 03:13:01 UTC and end time 03:26:30 UTC, the region for comparison is between latitude 48.83 and 54.81 N. Figure 48 shows the aerosol type assignments based on the report: CALIOP Algorithm Theoretical Basis Document Part 3 [62]. The aerosol types are colour-coded as: blue – clean marine, yellow - dust, red - polluted continental, green – clean continental, brown – polluted dust and black – smoke.

From the Raman backscatter profile (Figure 42 (b)), a large aerosol layer was detected between 2.0 and 4.0 km, this correlates to the green trace on the HYSPLIT model (Figure 43 left). The lidar ratio for this layer is 66 ± 4 sr agreeing with the lidar ratio found for dust in [133]. While the backward trajectory (red line, Figure 43 left) suggests that the layer between 550 to 700 m passed over the Atlantic Ocean, indicating marine aerosol confirmed by a lidar ratio of 26 ± 5 sr (see Figure 42 (c)) and agrees with lidar ratio for marine aerosol particles [134]. Both the DREAM and NAAPS models predicated the dust entering Ireland's atmosphere on 8 April; see Figure 43 (right) and

Figure 44 respectively. The trajectories from HYSPLT show that the air masses at 650 m (red), 1500 m (blue) and 2300 m (green) originated over the Atlantic Ocean. It is evident that no mixing between the PBL and the dust occurred as shown by the different lidar ratio at each layer height, i.e. 26 ± 5 sr to 550 to 700 m and 66 ± 4 sr 2000 to 4000 m. Between 0.8 and 2.0 km the lidar ratio suggest there is additional mixing taking place, a lidar ratio of 51 ± 2 sr between 0.9 and 1.2 km suggests dust, marine and anthropogenic particles are mixing [133] and a polluted marine aerosol layer between 1.5 and 1.8 km with a lidar ratio of 30 ± 2 sr [99]. There is a varying amount of mixing of dust taking place between each air mass height as shown by the different lidar ratio at each layer, i.e. 26 ± 5 sr from 550 to 700 m, 53 ± 3 sr from 800 to 1200 m and 66 ± 4 sr from 2000 to 4000 m. CALIPSO also confirms the presence of dust at 03:13:01 to 03:26:30 on the morning of 8 April, over the Atlantic Ocean (lat 53.87^{o} lon -12.02^{o} to lat 47.89^{o} lon -14.64^{o} (Figure 48)). Figure 45 show the colour-coded image of the range corrected 532 nm backscatter signal vs. time where the layer between 2.0 to 4.0 km is clearly evident.

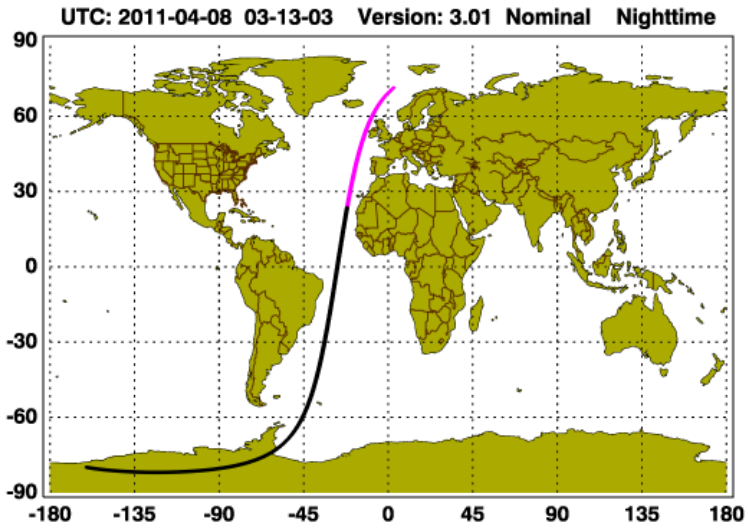


Figure 46. CALIPSO orbit projection for 8 April in black. The orbit projection in pink corresponds to the time when data shown in Figure 48 were taken. The horizontal and vertical axes represent latitude (deg) and longitude (deg) respectively.

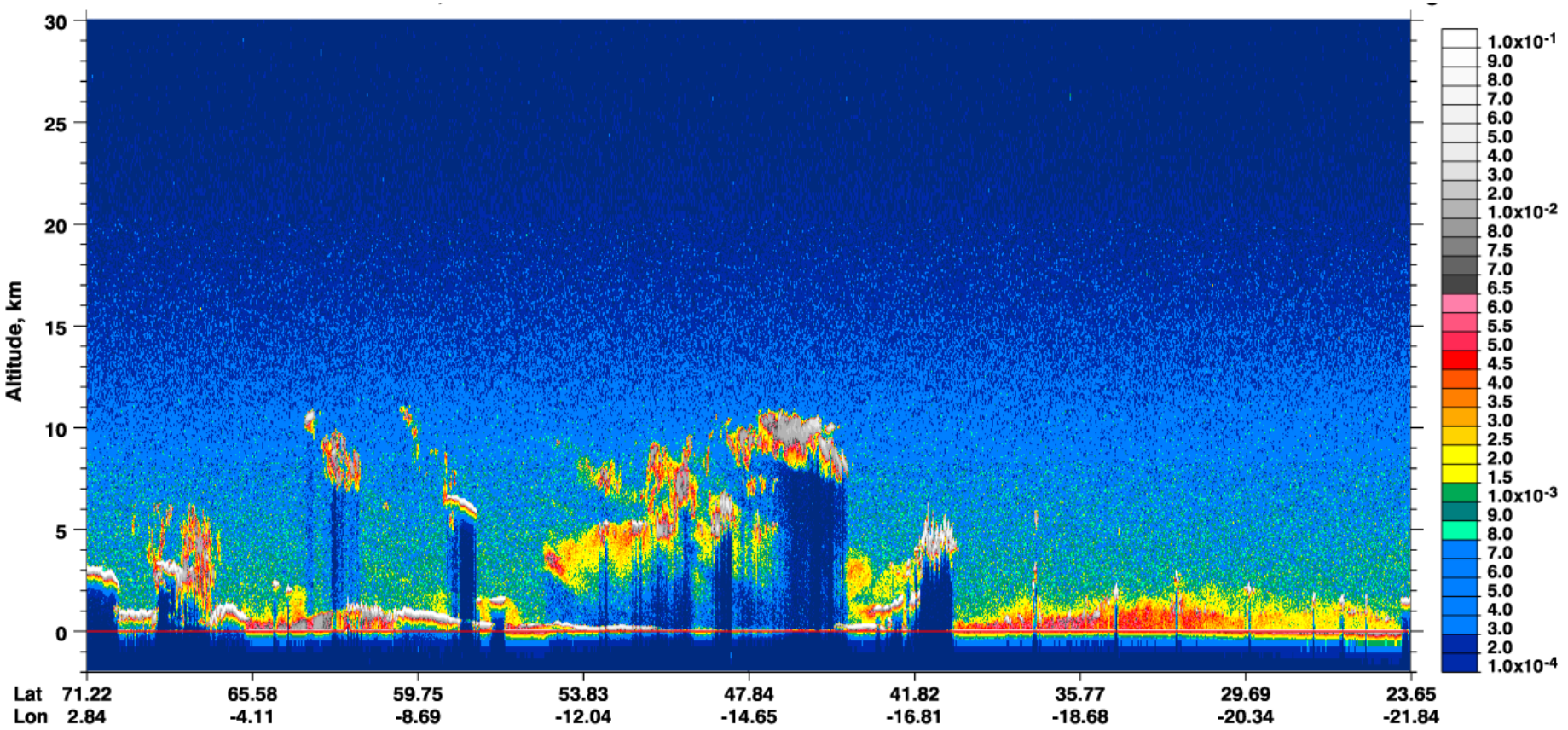


Figure 47. CALIPSO night-time colour-coded (unit: $km^{-1}sr^{-1}$) total attenuated backscatter, for 8 April 2011, start time 03:13:01 UTC and end time 03:26:30 UTC. An estimated surface elevation is derived from a digital elevation map and is displayed as a red line [135].

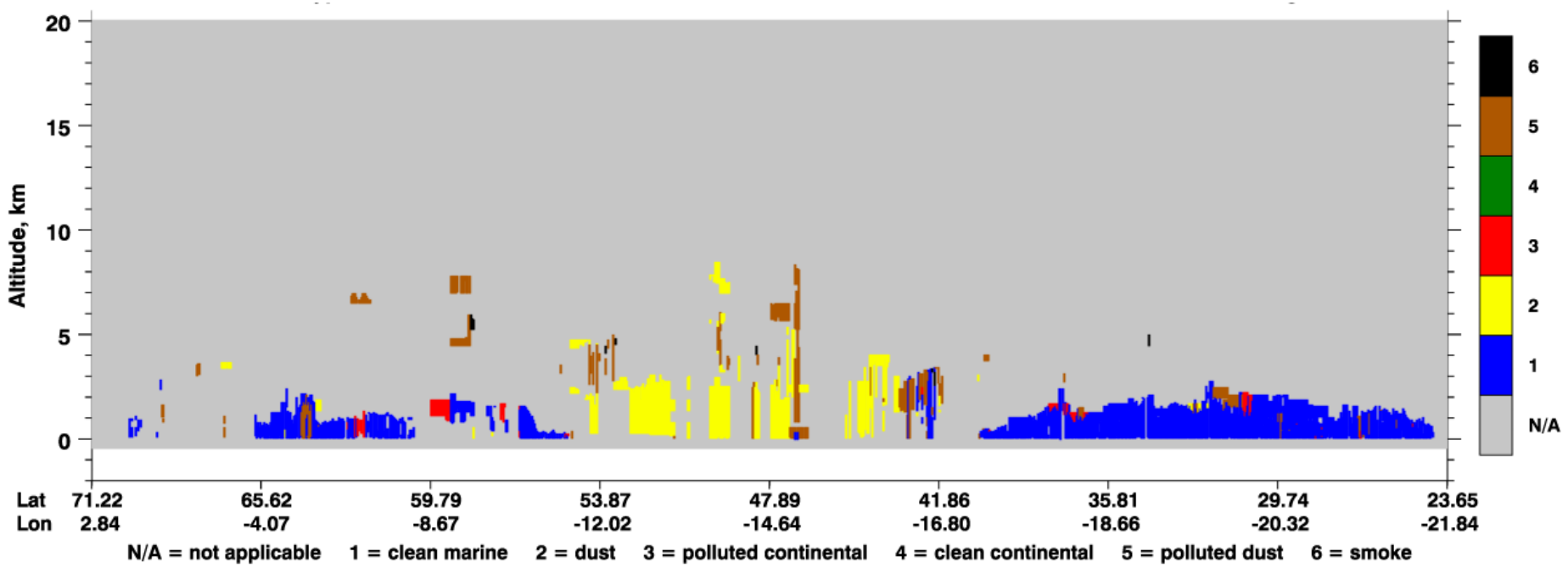


Figure 48. Colour-coded aerosol subtype analysis for the total attenuated backscatter shown in Figure 47 : blue – clean marine, yellow - dust, red - polluted continental, green – clean continental, brown – polluted dust and black – smoke [135].

21 April 2011

Figure 49 shows an aerosol event detected at the Cork site on 21 April 2011. Panels (a), (b), and (c) show the extinction coefficient, the Raman backscatter coefficient and the lidar ratio as a function of altitude, respectively. The integration time was 30 minutes. The top height of the PBL was determined to be 615 ± 30 m. In Figure 50 (left) a backward trajectory (4 days) is shown as determined by the HYSPLIT model. The model implies that the air masses over Cork on that day arrived from Western Europe. A large dust event was forecast by the DREAM model for the end of April 2011. According to the model on 21 April dust was present over Spain and southern France; these locations match with the blue, cyan and green traces on the HYSPLIT backward trajectory (see Figure 50 (left)). According to the NAAPS model for 21 April at 10:10 (see Figure 50 (right)) dust was present above Ireland and sulphate was present at the Cork site.

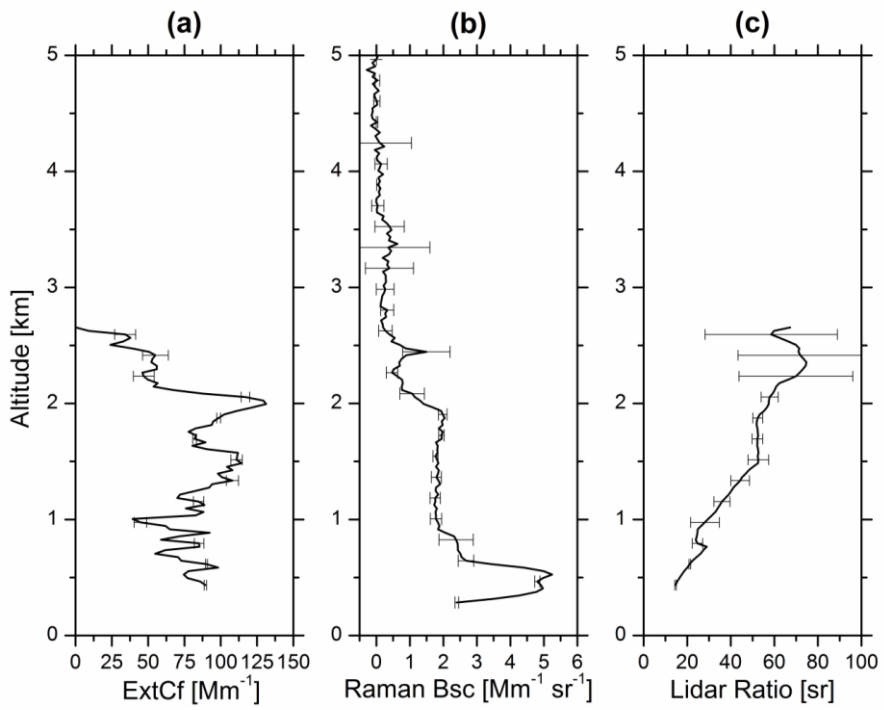


Figure 49. Measurement on 21 April 2011 (2130-2200 hrs). (a): Extinction coefficient (ExtCf) with errors (signal smoothing with window lengths of 250 m up to 960 m, 390 m between 960 and 2490 m, and 570 m from 2490 m upwards, (b) Raman backscatter (Bsc) solution with errors (up to 5 km), (c) Lidar ratio with a smoothing window of 270 m. An aerosol layer is evident between 0.5 – 2 km with a lidar ratio between 20 and 60 sr. Error bars indicate the standard deviation caused by photon noise.

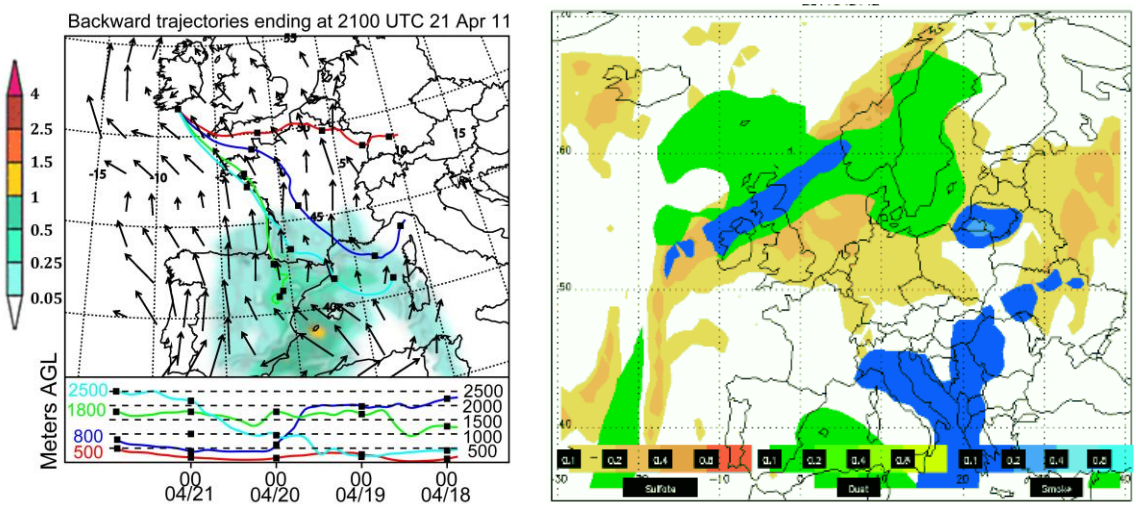


Figure 50. Left: NOAA HYSPLIT model backward trajectories for four days before 21 of April. The map includes the colour-coded (unit: g/m^2) image from the DREAM forecast for 21 April, 1200 hrs. Wind directions are also indicated. A dust event was predicted over Spain and southern France as indicated by the image. Trajectories indicate aerosol particles arrived at Cork from the European continent. Right: NAAPS Aerosol Model for 21 April 2011. The colour code for different aerosol particles are: sulphate - orange to red, dust - green to yellow and smoke - blue. The model predicts a large dust event above Ireland [131].

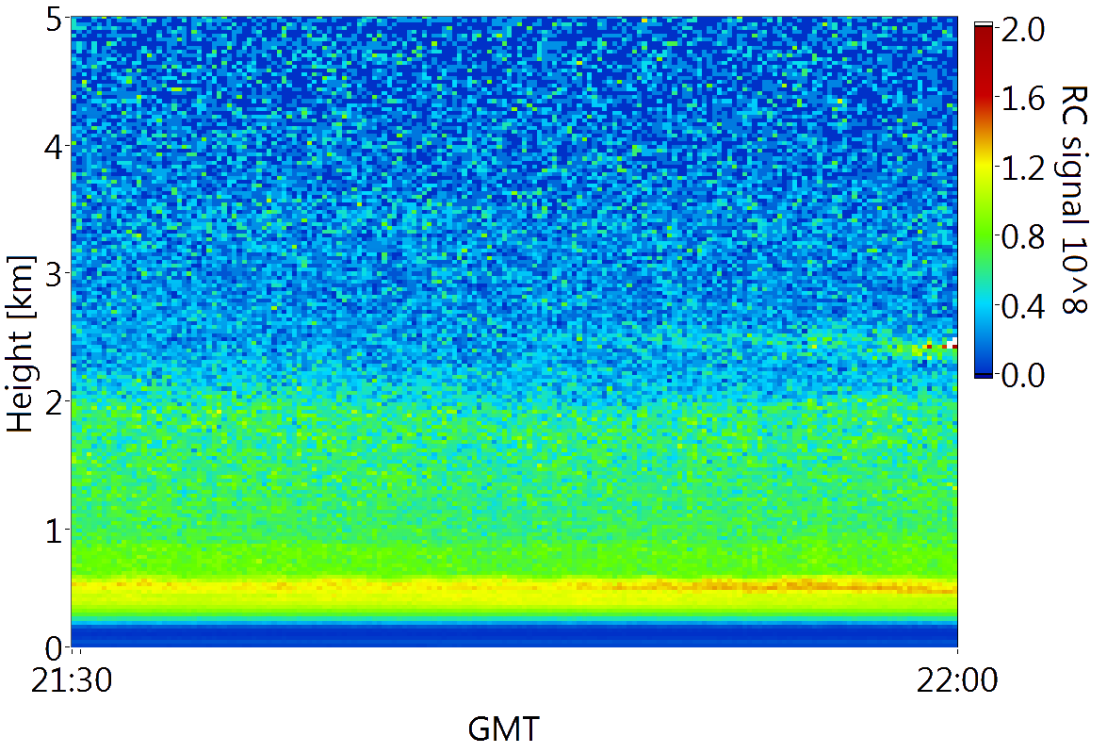


Figure 51. Colour-coded image of time-dependent range corrected 532 nm backscatter profiles of the measurement on 21 April for a 30 min period. A wide aerosol layer is evident between 0.5 km and 2.0 km.

Figure 52 shows the orbital path of CALIPSO over Ireland for the 21 April. The data presented in Figure 54 corresponds to the time of the orbit projection shown in pink in Figure 52. Figure 53 shows the total attenuated backscatter coefficient for 21 April 2011, start time 02:43:17 UTC and end time 02:56:46 UTC, the region for comparison is between latitude 48.83^{o} N to 54.81^{o} N. Figure 54 shows the aerosol type assignment for CALIPSO.

From the Raman backscatter profile (Figure 49 (b)) a large aerosol layer was detected between 0.7 and 2 km and another one at 2.5 km. Both these correspond to the blue (0.7 – 2 km) and cyan (2.5 km) trajectories calculated with the HYSPLIT model (Figure 50 left). While the backward trajectory suggested that the layer between 500 to 800 m passed over Western Europe (red line, Figure 50 left), it was likely that mixing with local marine aerosol from the Celtic Sea took place during the transport to Cork. Given the low top altitude of the PBL and the strong marine layer above the PBL it was concluded that the layer at 2.5 km was a pure dust layer with a lidar ratio of 70 sr, while the layer from 1.0 to 1.8 km contained dust, marine and anthropogenic particles (lidar ratio 40 to 50 sr). The lidar ratios agreed well with the ones measured in [133]. While DREAM forecast the dust entering Ireland's atmosphere on 23 April, the event was measured 30 hr before the model prediction. This is again illustrated in Figure 50 (left), where the data from DREAM are overlaid with trajectories from HYSPLIT. The figure also shows the prevailing wind directions at the time relevant for Ireland. Analysis of the CALIPSO night-time total attenuated backscatter signal (Figure 53) indicates that there was a region of polluted dust between 2 and 4 km at lat lat 48.88^{o}, lon -6.48^{o} (see Figure 54) confirming that dust was present on the morning of 21 April over the Celtic Sea. Figure 51 shows the colour-coded image of the range corrected 532 nm backscatter signal vs. time where the layer between 0.7 and 2.0 km is clearly evident. Another aerosol layer started to become evident at ca. 2.5 km altitude approximately at 21:50.

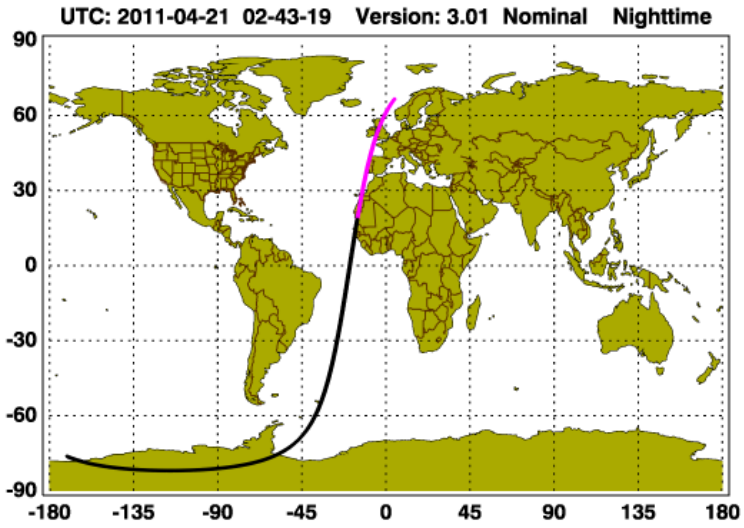


Figure 52. CALIPSO orbit projection for 21 April in black. The orbit projection in pink corresponds to the time when data shown in Figure 54 were taken. The horizontal and vertical axes represent latitude (deg) and longitude (deg) respectively.

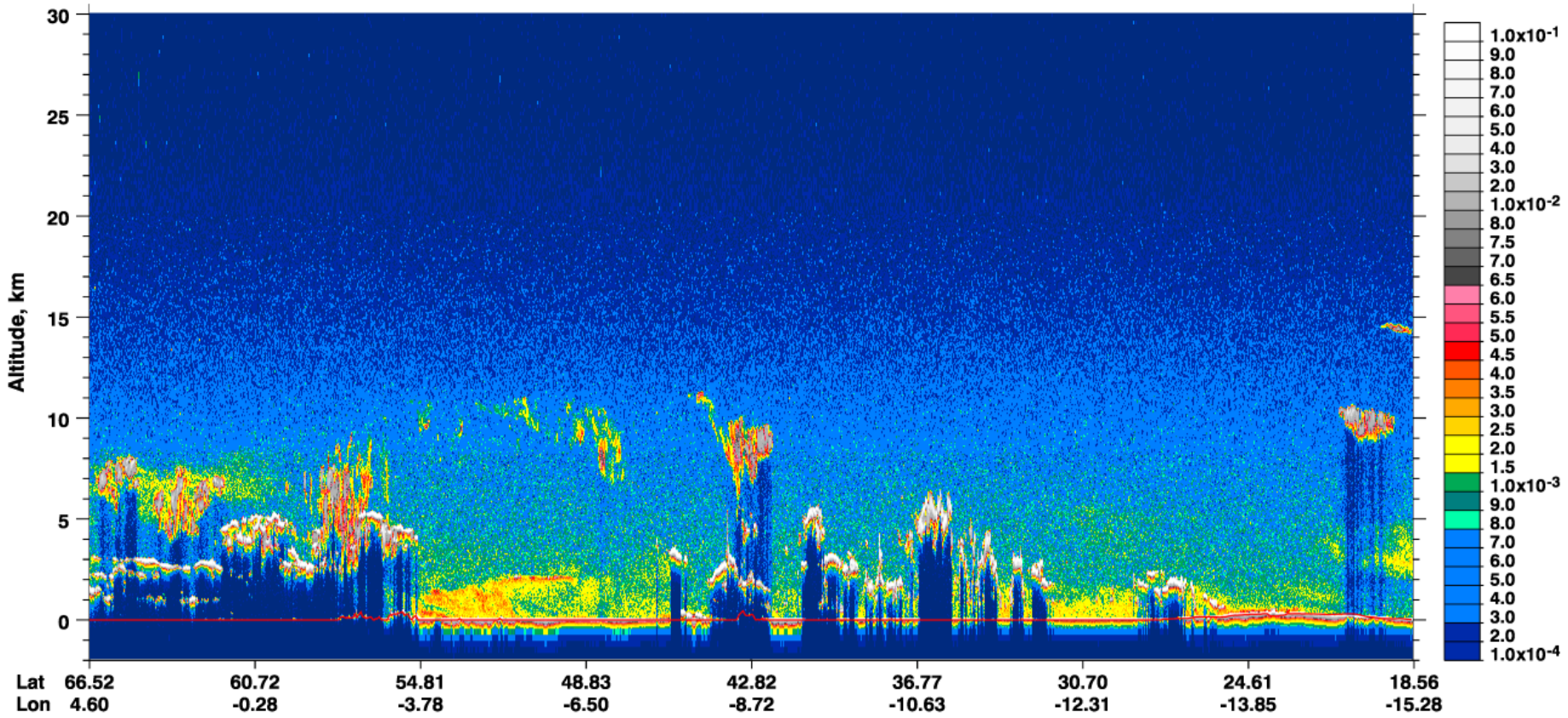


Figure 53. CALIPSO night-time colour-coded (unit: $km^{-1}sr^{-1}$) total attenuated backscatter, for 21 April 2011, start time 02:43:17 UTC and end time 02:56:46 UTC. An estimated surface elevation is derived from a digital elevation map and is displayed as a red line.

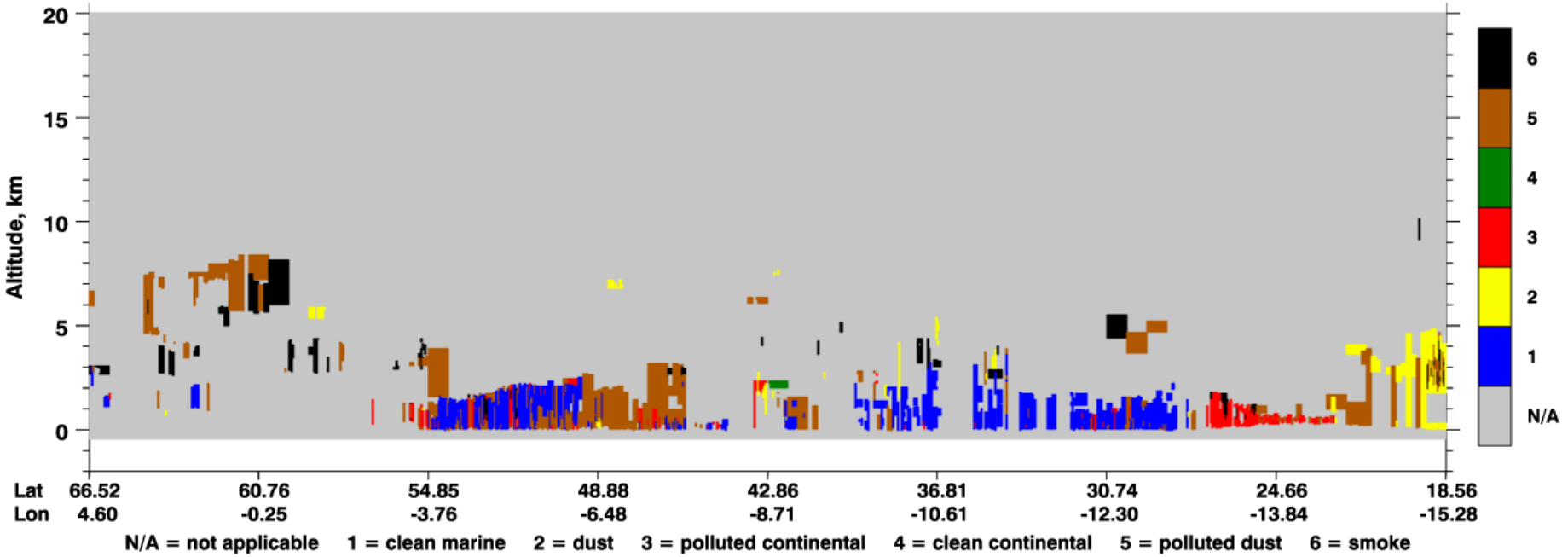


Figure 54. Colour-coded aerosol subtype analysis for the total attenuated backscatter shown in Figure 53: blue – clean marine, yellow - dust, red - polluted continental, green – clean continental, brown – polluted dust and black – smoke [135].

26-29 March 2012

A dust event was detected on 3 consecutive nights between 26 and 29 March. Figure 55 to Figure 58 show the profiles measured from 26 to 29 March. Panels (a), (b), and (c) show the extinction coefficient, the backscatter coefficient and the lidar ratio as a function of altitude, respectively. Figure 58 (b_1) shows the detection of cirrus clouds from 6.4 to 6.7 km and at the upper end of the typical range from 10.5 to 11.0 km; panel (b_2) is an enlargement of (b_1) plotted to an altitude of 5 km to provide more detail of the lower atmosphere. The integration time for each measurement was 60 minutes. The PBL height for the corresponding days was determined to be 465 ± 30 m, 495 ± 30 m, 465 ± 30 m and 460 ± 30 m respectively.

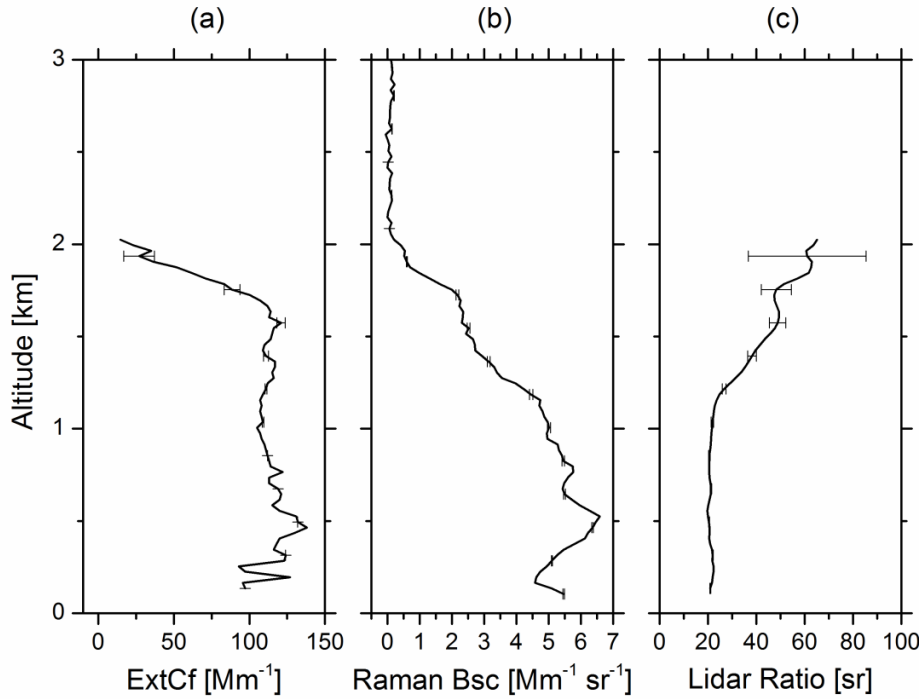


Figure 55. Measurement on 26 March 2012 (2030-2130 hrs). (a): Extinction coefficient (ExtCf) with errors (signal smoothing with window lengths of 90 m up to 720 m, 600 m between 720 and 1980 m, and 900 m from 1980 m upwards, (b) Raman backscatter (Bsc) solution with errors, (c) Lidar ratio with a smoothing window of 210 m. A strong extinction coefficient is evident between 0.5 – 2 km with a lidar ratio of 20 up to 1.2 km and between 50 and 60 sr from 1.6 km upwards. Error bars indicate the standard deviation caused by photon noise.

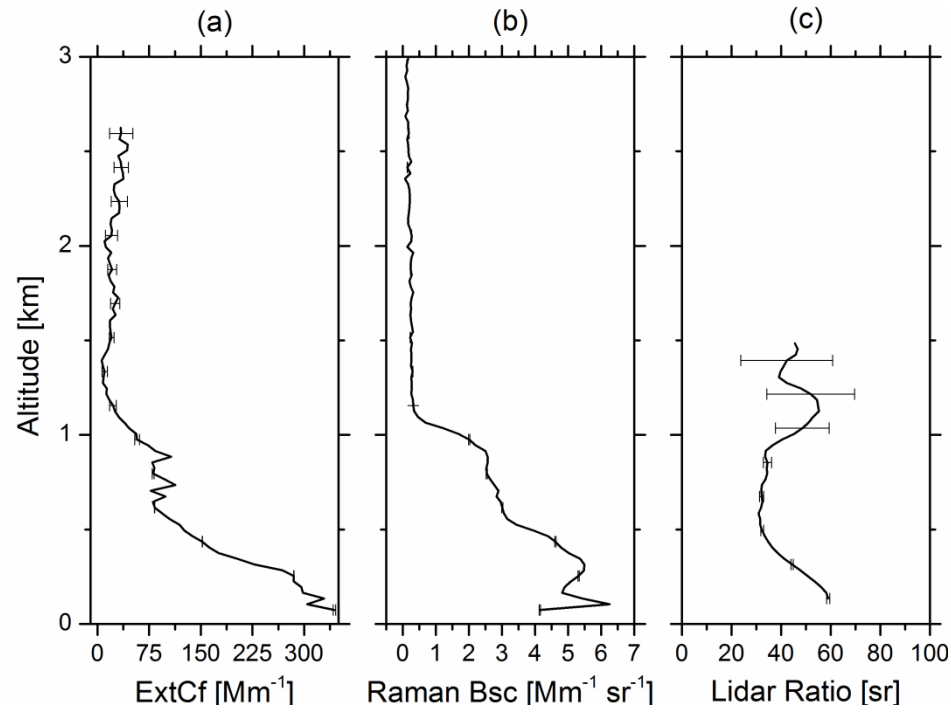


Figure 56. Measurement on 27 March 2012 (2030-2130 hrs). (a): Extinction coefficient (ExtCf) with errors (signal smoothing with window lengths of 120 m up to 750 m, 570 m between 750 and 1500 m, and 810 m from 1500 m upwards, (b) Raman backscatter (Bsc) solution with errors (up to 5 km), (c) Lidar ratio with a smoothing window of 210 m. A strong extinction coefficient is evident up to 500 m with a lidar ratio of between 30 and 60 sr. Error bars indicate the standard deviation caused by photon noise.

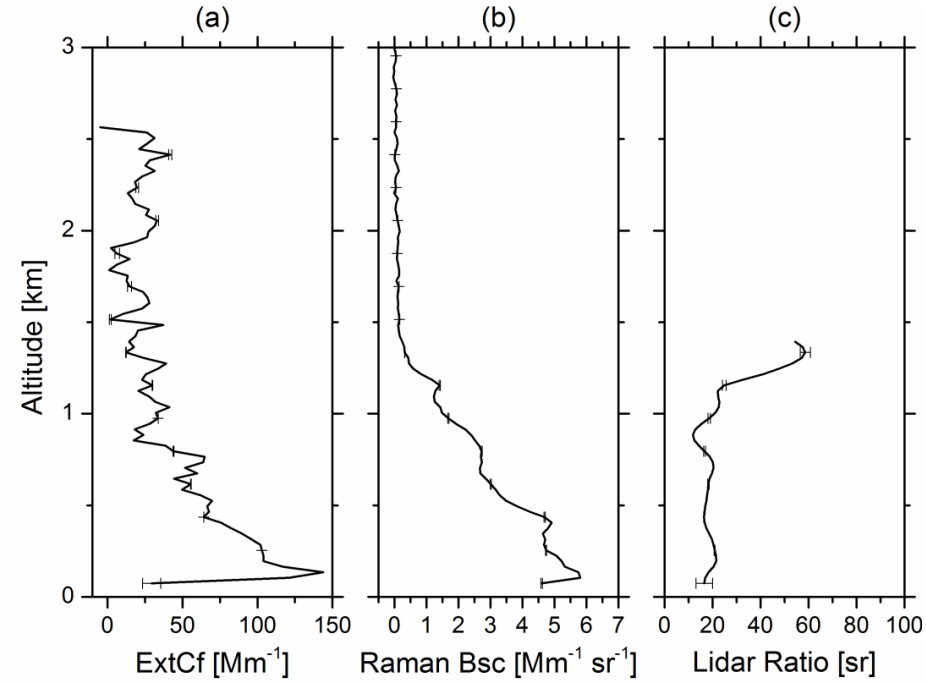


Figure 57. Measurement on 28 March 2012 (2030-2130 hrs). (a): Extinction coefficient (ExtCf) with errors (signal smoothing with window lengths of 210 m up to 1470 m and 360 m from 1470 m upwards, (b) Raman backscatter (Bsc) solution with errors, (c) Lidar ratio with a smoothing window of 210 m. Error bars indicate the standard deviation caused by photon noise.

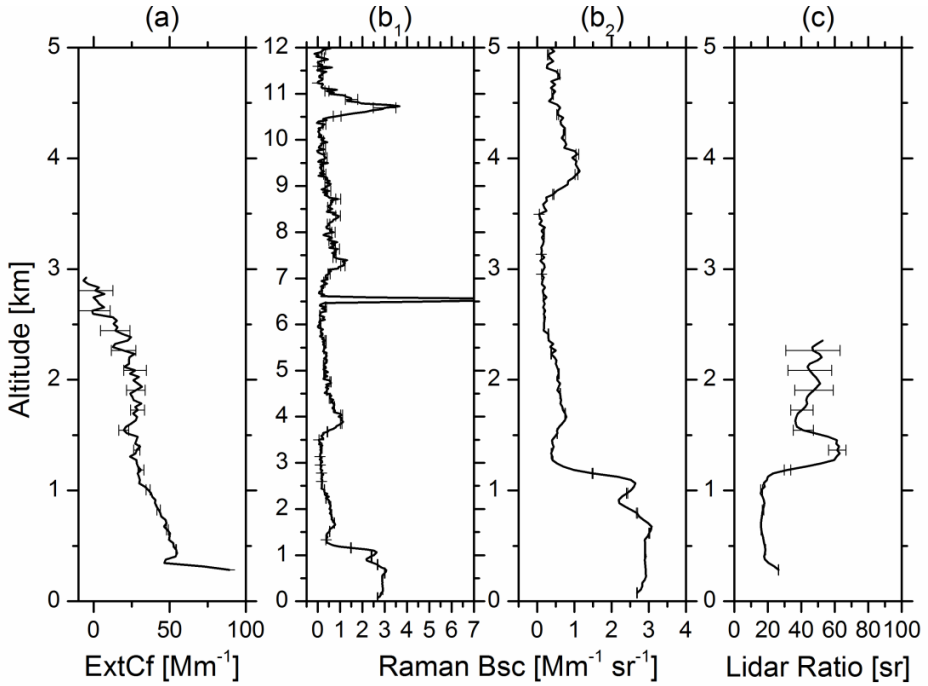


Figure 58. Measurement on the 29 of March 2012 (2100-2200 hrs). (a): Extinction coefficient (ExtCf) with errors (signal smoothing with window length of 490 m, (b_1) Raman backscatter (BSc) solution with errors (up to 12 km); cirrus cloud between 6.4 and 6.7 km and 10.5 and 11.0km. (b_2) Data from panel (b_1) for altitudes up to 3 km, (c) Lidar ratio with a smoothing window of 150 m. An aerosol layer is evident between 1.2 and 2.4 km with a lidar ratio between 40 and 60 sr. Error bars indicate the standard deviation caused by photon noise.

In Figure 59 a backward trajectory (4 days) is shown for each day ((a) 26 March, (b) 27 March, (c) 28 March and (d) 29 March) as determined by the HYSPLIT model. The model implies that the air masses over Cork from 26 to 29 March arrived from north central Europe and the North Sea with the exception of (d) where the air masses at 4.0 km (cyan) originated over the Atlantic Ocean. A large dust event was forecast by the DREAM model. According to the model on 26 March dust was present over Spain and Portugal originating from the Saharan Desert (Figure 60 (a)) and forecast to progress north over the Atlantic Ocean (Figure 60 (c and d) 27 and 28 March) and finally dispersing on 29 March (Figure 60 (d)). According to the NAAPS model a larger dust event was predicted when compared to the DREAM model in Figure 60. Figure 61 (a) indicates that dust was present in the atmosphere over Cork on 26 March. As time progressed the dust remained over the Irish Coast and the Atlantic Ocean to the North Sea (Figure 61 (b) and (c) 27 and 28 March). Figure 61 (d) indicates that the dust was dispersing over Northern Ireland and to the west of Ireland over the Atlantic Ocean on 29 March.

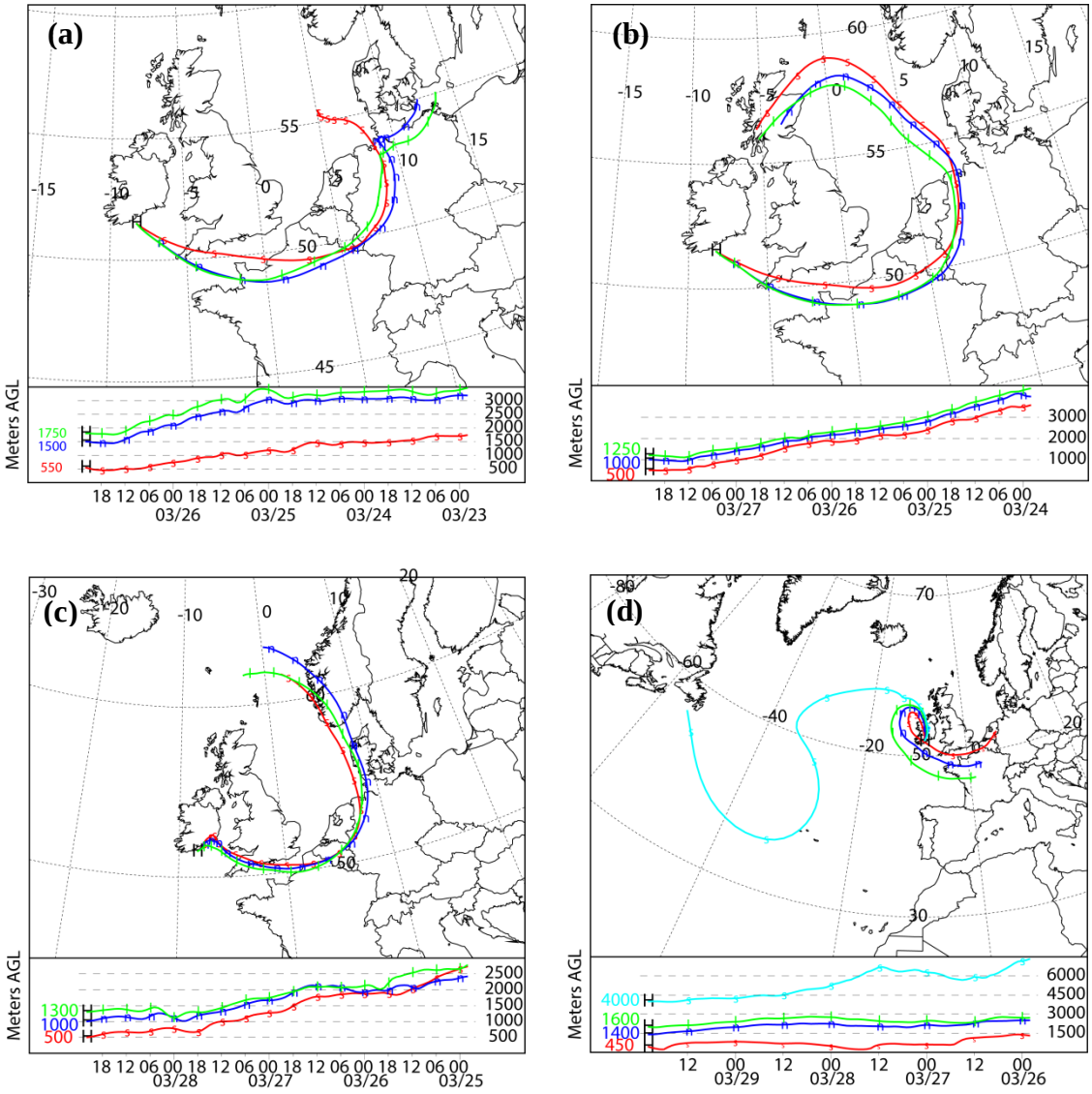


Figure 59. NOAA HYSPLIT model backward trajectories for four days before (a) 26 March, (b) 27 March, (c) 28 March and (d) 29 March. All trajectories indicate aerosol arrived at Cork from the north of central Europe and the North Sea.

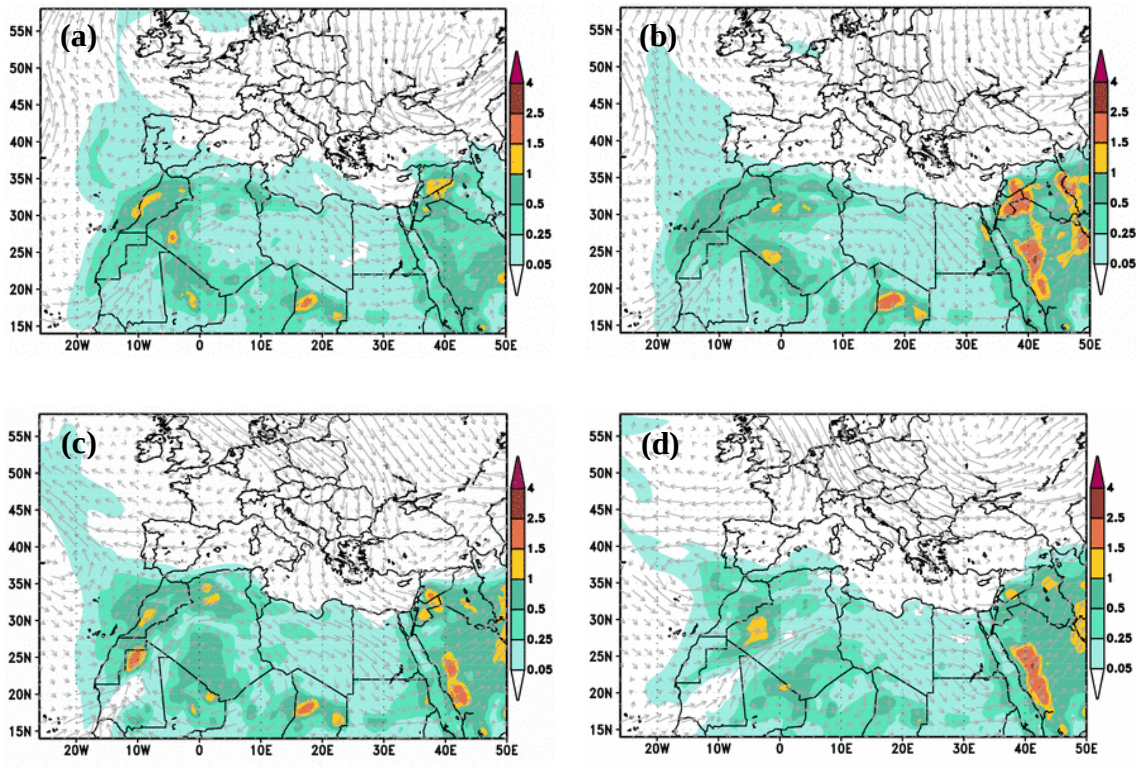


Figure 60. Dream model forecast for dust loading over North Africa, Middle East and Europe for (a) 26 March, (b) 27 March, (c) 28 March and (d) 29 March (colour-coded unit: g/m^2). Wind directions are also indicated. A dust event was predicted over (a) Spain and Portugal progressing north over the Atlantic Ocean (b – d) [132].

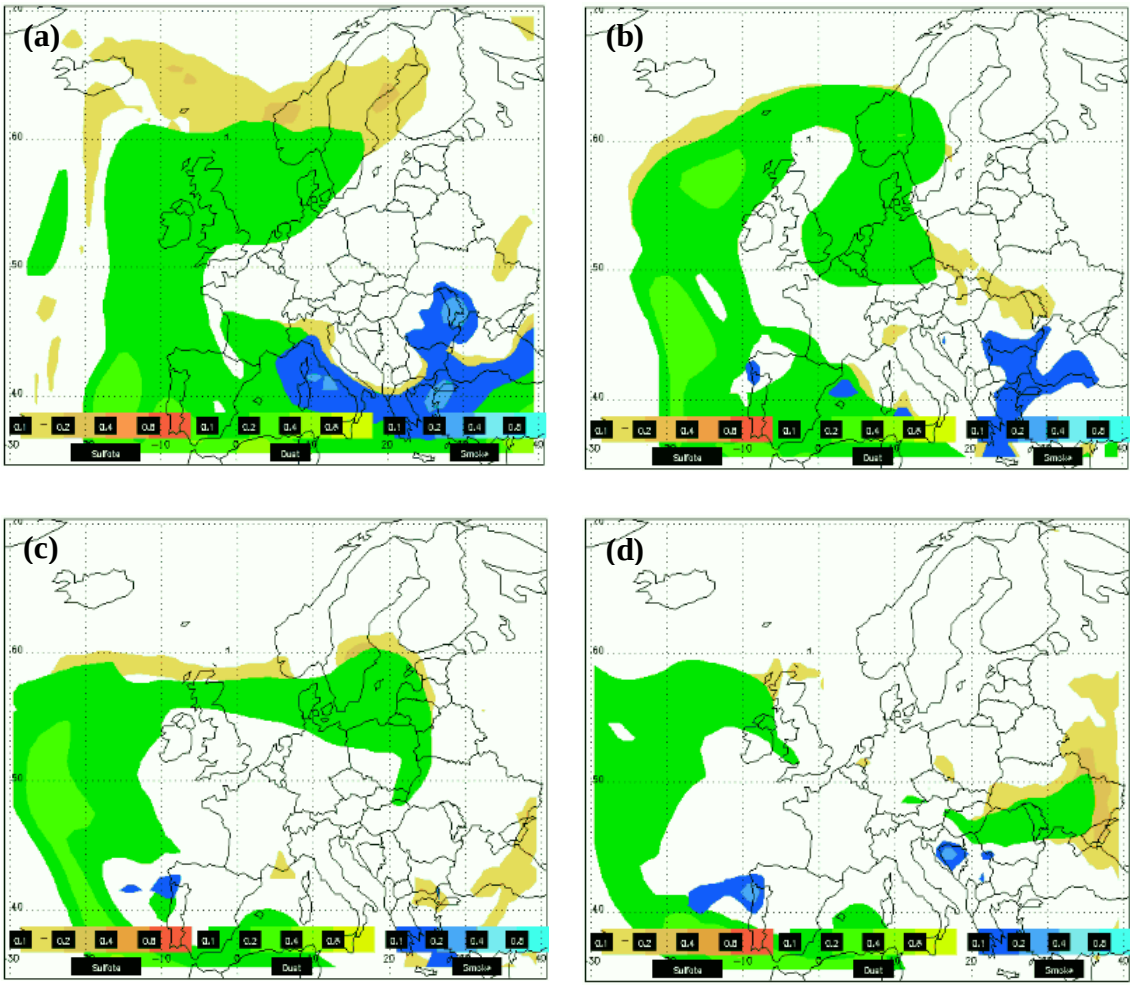


Figure 61. NAAPS Aerosol Model for (a) 26 March, (b) 27 March, (c) 28 March and (d) 29 March. The colour code for different aerosol particles are: sulphate - orange to red, dust - green to yellow and smoke - blue. The model predicts a larger dust event than the Dream model in Figure 60. Dust was predicted over Ireland (a) and continues to remain over the north of central Europe and the North Sea (b, c) and dispersing by 29 March (d) [131].

Figure 62 shows the orbital path of CALIPSO over Ireland for (a) 26 March, (b) 27 March and (c) 28 March, there is no CALIPSO overpass available for 29 March. The data presented on attenuated backscatter in Figure 63, Figure 65 and Figure 67 correspond to the times when CALIPSO passed over Ireland near Cork (green - day-time overpass and pink - night-time overpass) as shown in Figure 62, 26 March start time 13:22:42 UTC and end time 13:36:11 UTC, 27 March start time 02:59:18 UTC and end time 03:12:46 UTC, and 28 March start time 13:10:31 UTC and end time 13:23:59 UTC. The region in which data can be compared with those measured at the Cork site are ca. between lat 48.0^{o} N and 52.0^{o} N. Figure 64, Figure 66 and Figure 68 show the aerosol assignment type for 26 to 28 March.

Figure 55 (c) indicates the presence of dust over the Cork site on 26 March with a lidar ratio of 48 ± 2 sr between an altitude of 1.5 and 1.8 km, and 62 ± 2 sr between 1.8 and 2.0 km. Pisani et al. [136] report mean lidar ratios from dust to be between 46 sr (2.5 - 3.5 km height range) and 58 sr (3.5 - 5.0 km height range) and 77 sr (5.0 - 8.0 km height range) with a standard deviation < 10 sr. Similar to the event measured at the Cork site from 21 April 2011 (as discussed above - Figure 49), two layers were found to have different lidar ratios indicating a separation of pure dust and polluted dust (dust mixing with marine and anthropogenic particles). Computations by Dubovik et al. [137] show lidar ratios of about 70 sr (for a mean particle volume radius r_v = 5 μm), 55 sr (r_v = 2 μm), and 45 sr (r_v = 1 μm) for typical dust size distributions. Given the northerly wind direction (Figure 60), along with the predicted path of the dust from the DREAM and NAAPS models (Figure 60 and Figure 61) and that of the air mass heights at 500 m (red) not mixing with those at 1500 (blue) and 1700 m (green) would signify that the layer between 1.5 and 1.8 km (lidar ratio 48 ± 2 sr) is not influenced by continental aerosol particles. Since the altitude of the PBL height was low (465 ± 30 m) and due to the presence of a strong marine layer above the PBL at the time, the observed aerosol dynamics was likely to be governed by the settling of dust particles in dependence of the mean particle radius. Where the layer from 1.5 to 1.8 km and 1.8 to 2.0 km corresponds to a mean particle volume radius of r_v = 1 μm and r_v = 2 μm respectively. The data in Figure 64 confirmed the presence of dust between lat ~9^o N and 35^o N (over North Africa to North Spain). CALIPSO data in Figure 64 only detected marine particles close to the Cork site, thus it is likely that the dust plume had not advanced to Cork until the evening of 26 March.

For 27 March, there is an indication that air masses over Cork had the potential to mix from 500 m (red) to 1250 m (green) as seen in Figure 59 (b), whereas on the previous day (Figure 59 (a)) no mixing of the air masses at the PBL (ca. 500 m) and at 1500 m took place. The lidar ratio at the PBL height was 33 ± 1 sr. While below it between 135 and 495 m it was 46 ± 9 sr, and above 1000 m a lidar ratio of 48 ± 7 sr was found (see Figure 56 (c)). These lidar ratios indicate that the measured layers may be due to local anthropogenic (urban) aerosol from 135 to 495 m, polluted marine conditions from the PBL to 1000 m [99] and polluted dust from 1000 m onwards. The CALIPSO overpass for the 27 March (Figure 66) shows a region of polluted dust over Ireland (brown).

According to the NAAPS model, Figure 61 (c), the dust particles over Ireland was expected to decrease. This was confirmed with the measurement on 28 March (Figure 57) and the CALIPSO overpass which shows less polluted dust (brown) around Ireland and more marine aerosol particles (blue) (Figure 68). The lidar ratio, Figure 57 (c) at the PBL height was 18 ± 2 sr, 19 ± 3 sr from 75 to 1200 m, and 56 ± 2 sr from 1300 to 1400 m. A lidar ratio of 56 sr indicated that the layer observed between 1300 and 1400 m may have been due to dust particles, while a lidar ratio of 19 sr indicates marine aerosol particles.

The final measurement on 29 March is shown in Figure 58. A large aerosol layer was detected between 1.3 and 2.2 km, and cirrus clouds between 6.4 and 6.7 km and 10.5 and 11.0km. The lidar ratio at the PBL was 18 ± 1 sr, 19 ± 4 sr from 255 to 1200 m, 58 ± 6 sr from 1200 to 1500 m and 45 ± 5 sr from 1500 to 2300 m. The layer from 1200 m to 1500 m showed an increase in the measured lidar ratio for dust when compared with previous days. Mattis et al. [138] explains a similar increase of lidar ratios as follows: First, the long range transport of dust aerosol particles leads to an effective removal of coarse mode particles with diameters > 1 µm by gravitational settling. The lidar ratio increases as the ratio of fine to coarse-mode particles [139]. Second, the non-spherical shape of the particles may lead to a strong reduction of the backscattering efficiency compared with backscattering by surface-equivalent spheres [140, 141]. Comparing the backscatter profiles measured at Cork (Figure 55 to Figure 58), it is evident that there is a reduction in the backscatter coefficient from ca. 5 Mm sr^{-1} on 26 March to ca. 1 Mm sr^{-1} by 29 March; this indicates that the dust particles detected may have been non-spherical in shape.

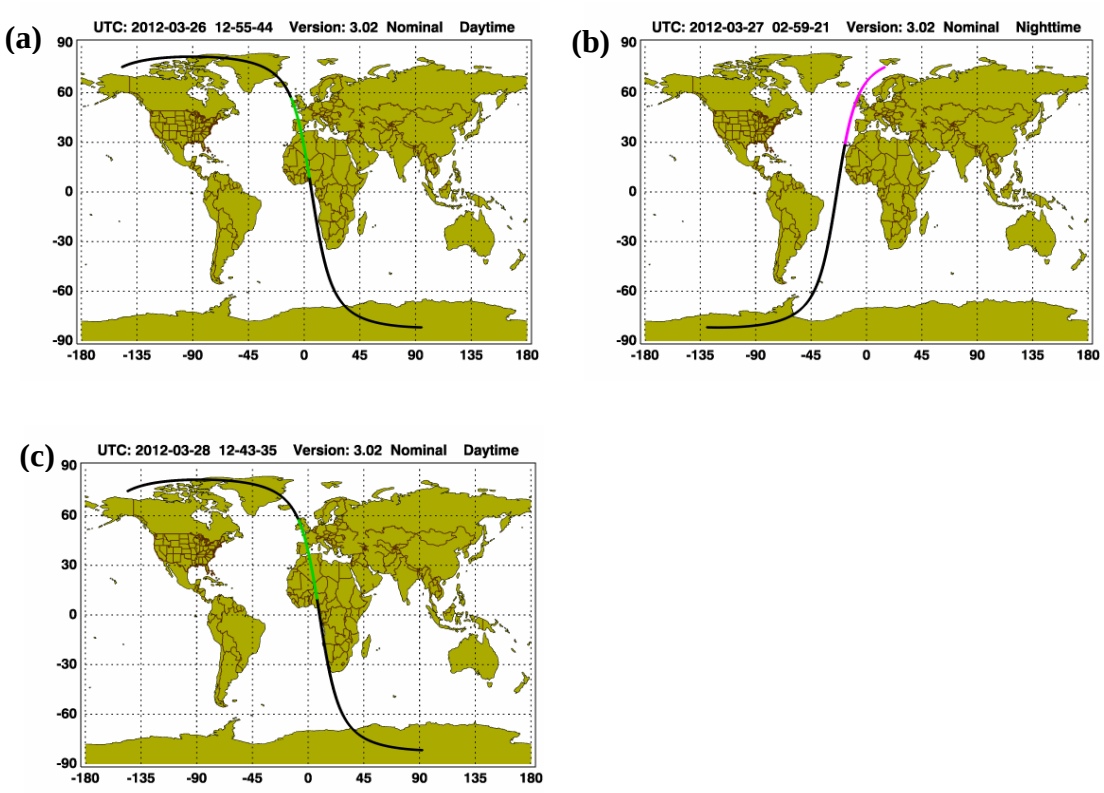


Figure 62. CALIPSO orbit projection for (a) 26 March, (b) 27 March and (c) 28 March are in green (day-time overpass) and pink (nigh-time overpass). The horizontal and vertical axes represent latitude (deg) and longitude (deg) respectively.

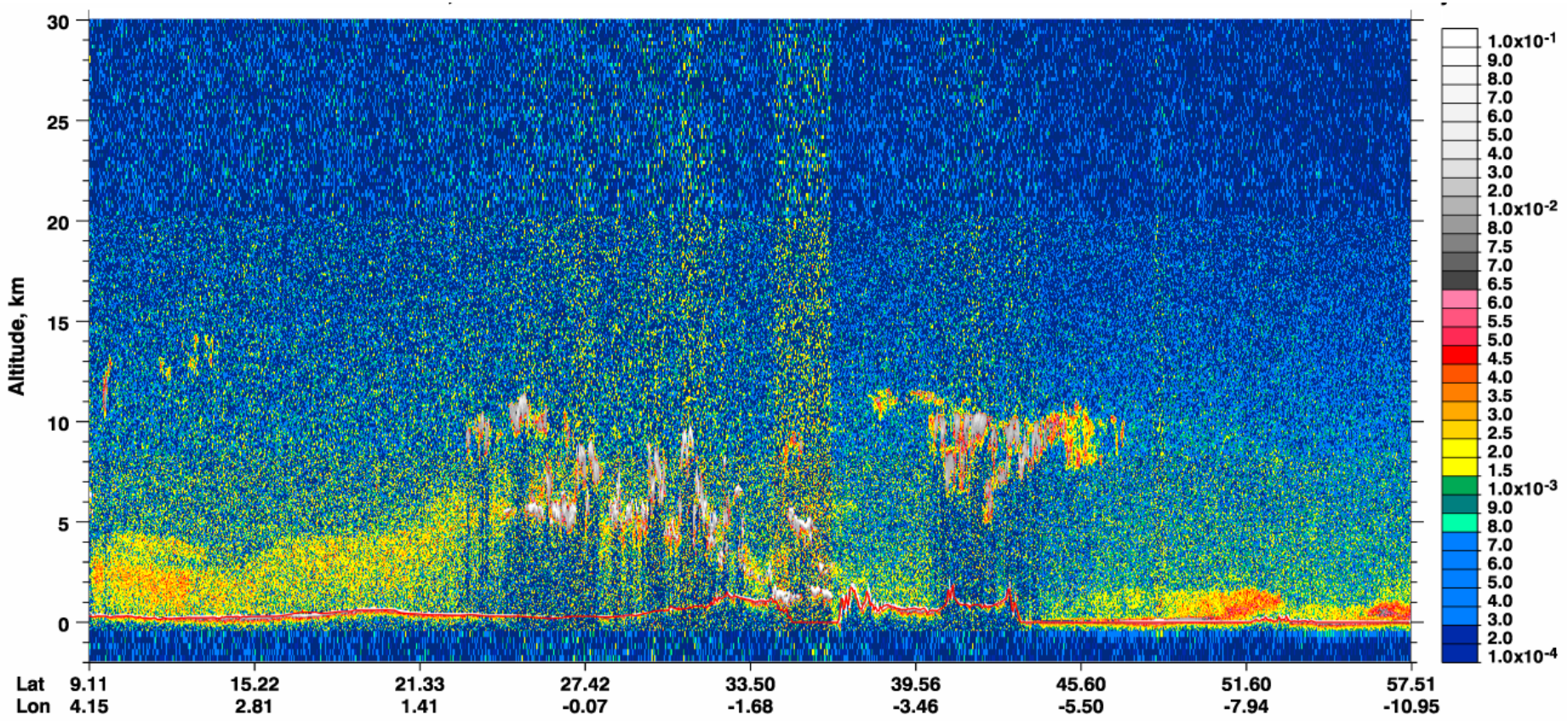


Figure 63. CALIPSO day-time colour-coded (unit: $km^{-1}sr^{-1}$) total attenuated backscatter, for 26 March 2012, start time 13:22:42 UTC and end time 13:36:11 UTC. An estimated surface elevation is derived from a digital elevation map and is displayed as a red line.

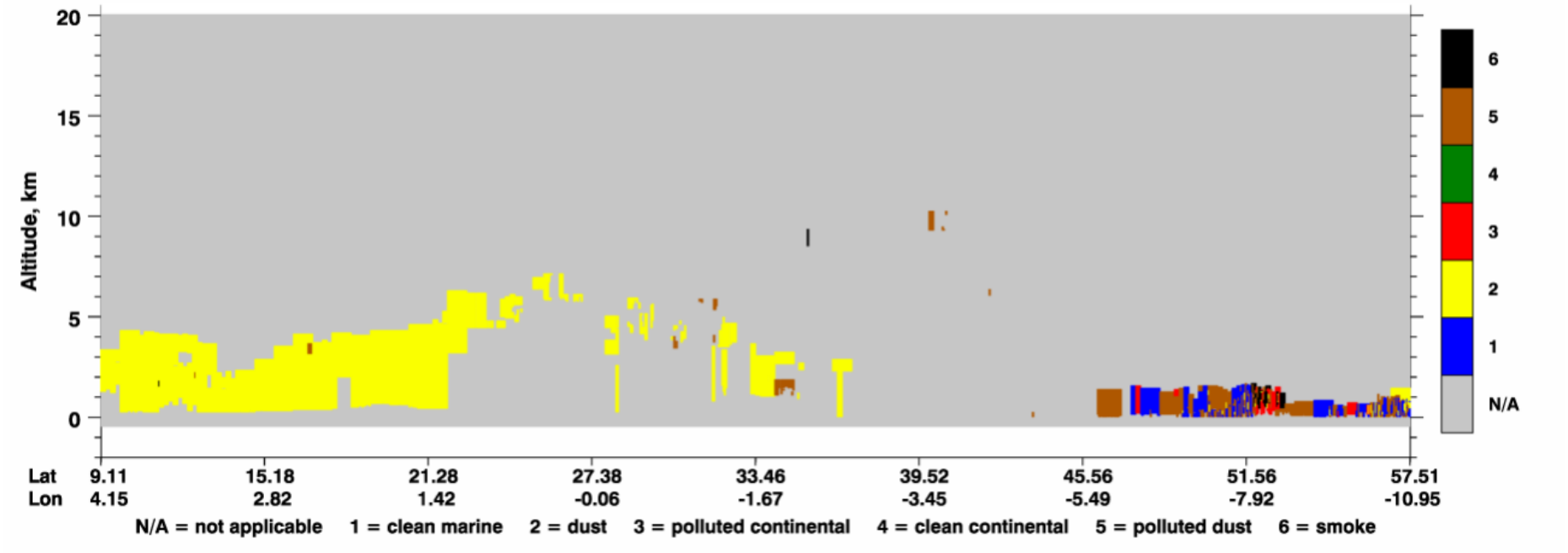


Figure 64. Colour-coded aerosol subtype analysis for the total attenuated backscatter shown in Figure 63: blue – clean marine, yellow - dust, red - polluted continental, green – clean continental, brown – polluted dust and black – smoke [135].

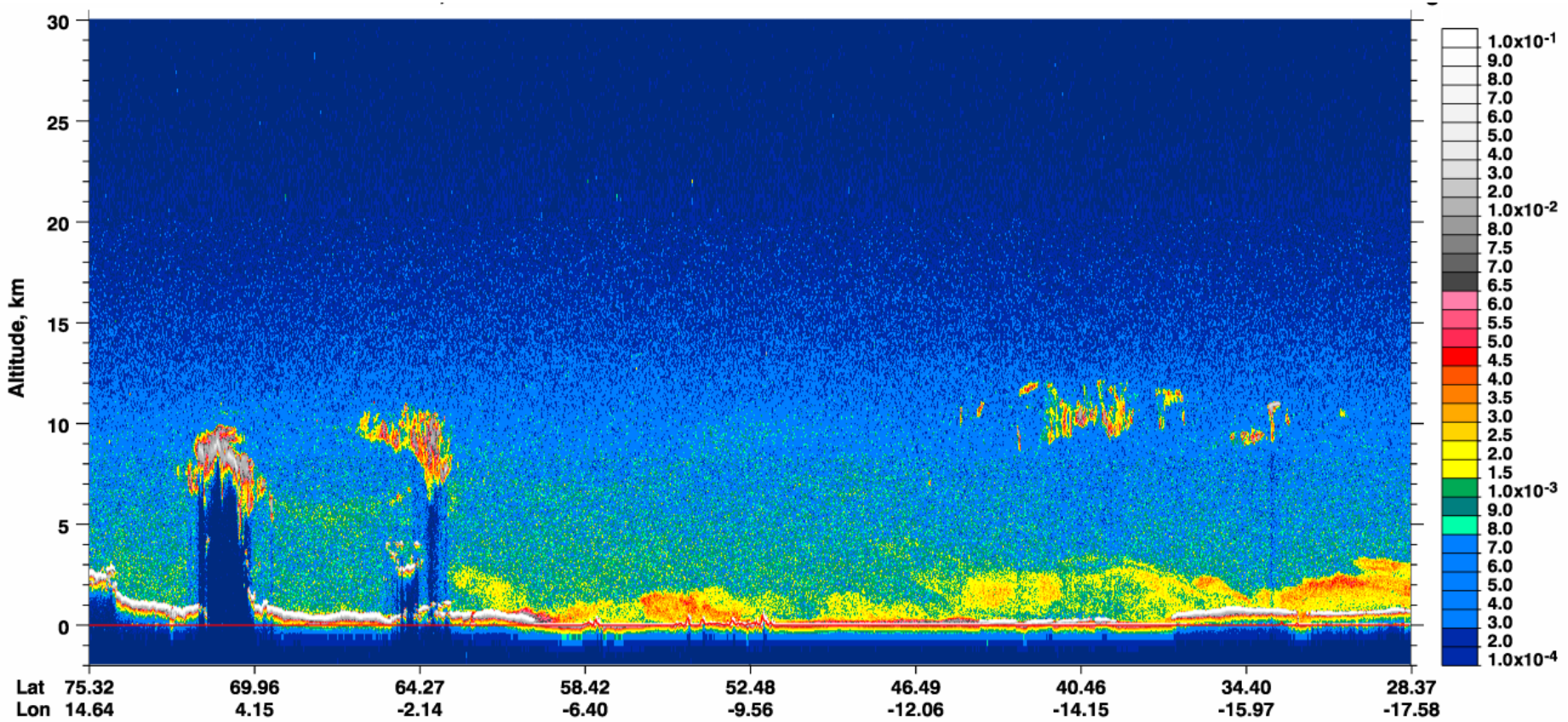


Figure 65. CALIPSO night-time colour-coded (unit: $km^{-1}sr^{-1}$) total attenuated backscatter, for 27 March 2012, start time 02:59:18 UTC and end time 03:12:46 UTC. An estimated surface elevation is derived from a digital elevation map and is displayed as a red line.

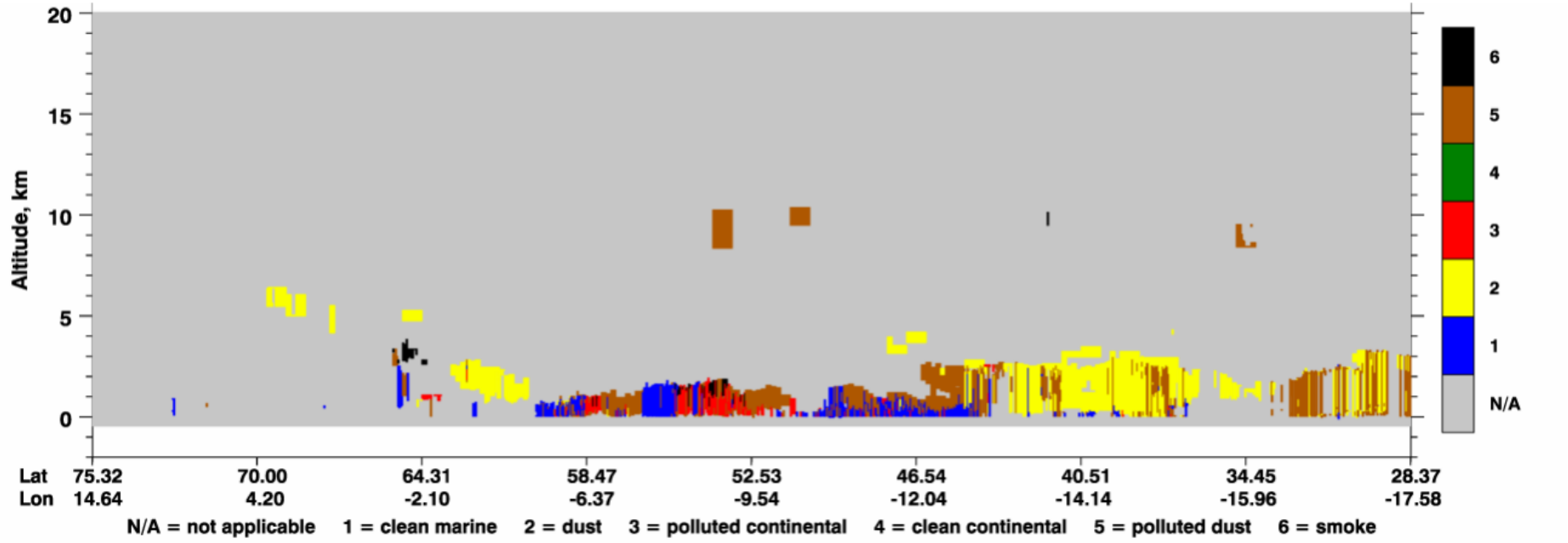


Figure 66. Colour-coded aerosol subtype analysis for the total attenuated backscatter shown in Figure 65: blue – clean marine, yellow - dust, red - polluted continental, green – clean continental, brown – polluted dust and black – smoke [135].

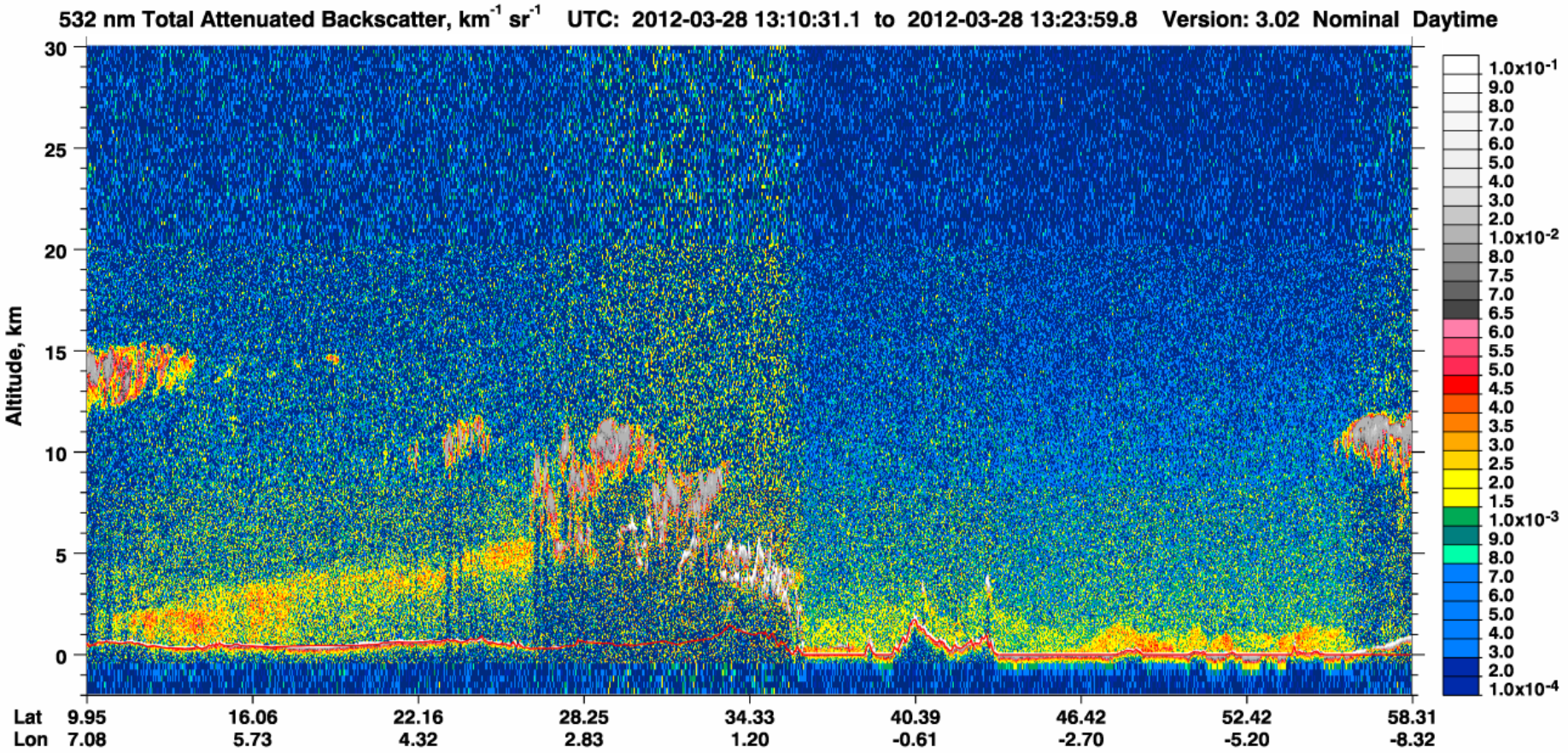


Figure 67. CALIPSO day-time colour-coded (unit: $km^{-1}sr^{-1}$) total attenuated backscatter, for 28 March 2012, start time 13:10:31 UTC and end time 13:23:59 UTC. An estimated surface elevation is derived from a digital elevation map and is displayed as a red line.

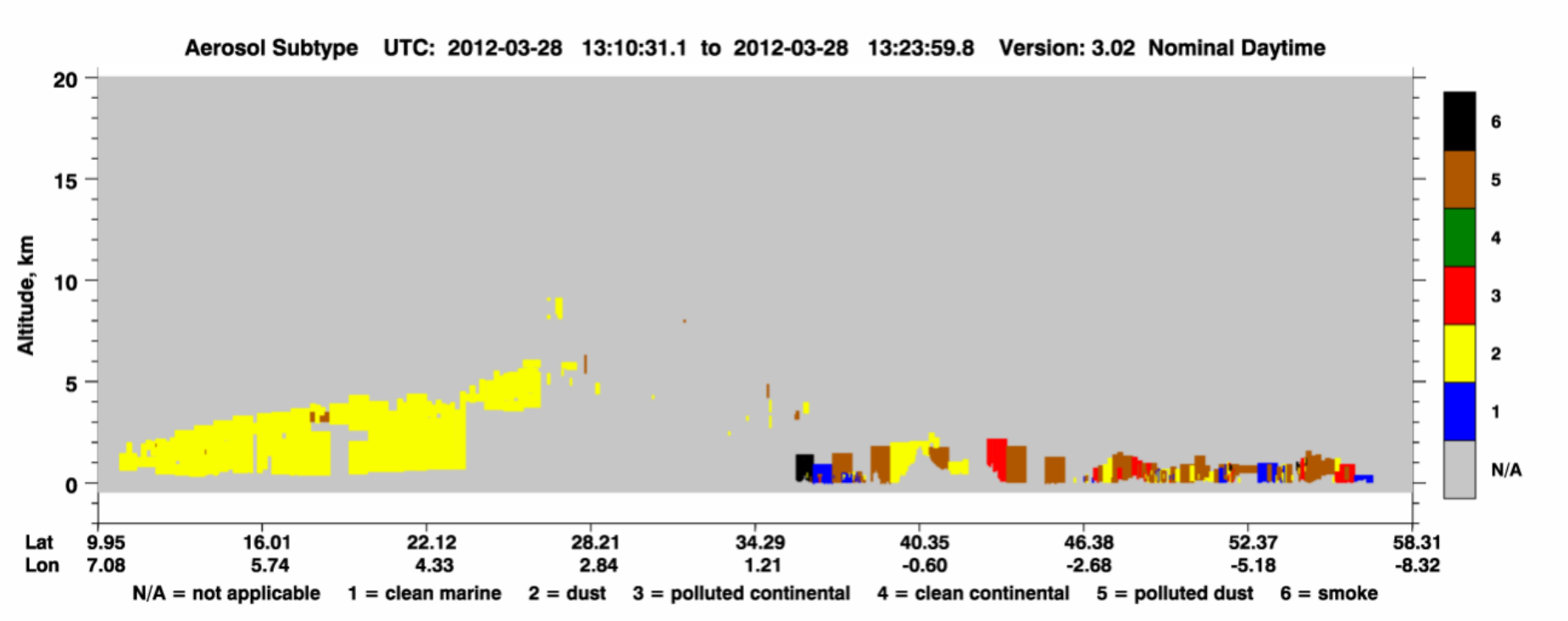


Figure 68. Colour-coded aerosol subtype analysis for the total attenuated backscatter shown in Figure 67: blue – clean marine, yellow - dust, red - polluted continental, green – clean continental, brown – polluted dust and black – smoke [135].

AOD analysis

Estimates of the AOD at 532 nm are obtained by vertically integrating the lidar profiles of the particle extinction coefficient. It should be noted that the minimum height for extinction lidar measurements can vary from 150 to 390 m depending on the overlap function and smoothing window lengths, which prevents obtaining reliable extinction estimates below this height. In order to improve the significance of the AOD estimates, the lidar extinction profiles were extrapolated to the surface by assuming that the lowest extinction value at the minimum height was constant down to ground level. Two AOD values are calculated for each measurement: (i) $AOD_{PBL,}$ from the ground level to the top of the PBL, and (ii) $AOD_{TOT,}$ from ground level to the top of the dust layer. It was expected that a significant number of measurements would have marine conditions in the PBL region. Table 9 shows the AOD for Cork for days were dust was measured and the lidar ratio up to the top height of the PBL (LR_{PBL}). With the exception of 27 March, the mean AOD_{PBL} for marine conditions (lidar ratio ca. = 20 sr) was 0.051 ± 0.01. The AOD_{TOT} for dust are in agreement with values reported in [142]. In addition, a decrease of ca. 60 % in the AOD_{TOT} was evident over 26 to 29 of March, confirming the decrease of dust over the Cork site.

Table 9. Lidar ratio (LR_{PBL}) averaged up to the top height of the PBL Aerosol optical depth at 532 nm (AOD_{PBL} - ground level to the PBL height and AOD_{TOT} - ground level to the top of the dust layer) for dust events at the Cork site. Errors show the uncertainty calculated by error propagation cause by photon noise.

Date	LR_{PBL}	AOD_{PBL}	AOD_{TOT}
8 April 2011	25 ± 3	0.053 ± 0.001	0.494 ± 0.120
21 April 2011	18 ± 3	0.054 ± 0.001	0.210 ± 0.022
26 March 2012	21 ± 1	0.063 ± 0.001	0.212 ± 0.053
27 March 2012	49 ± 9	0.127 ± 0.003	0.213 ± 0.043
28 March 2012	19 ±2	0.048 ± 0.001	0.084 ± 0.002
29 March 2012	20 ±3	0.036 ± 0.001	0.099 ± 0.012

5. Conclusion

A Raman lidar system operating at 532 nm with 150 mJ was established at University College Cork (51.3 N 8.29 W, 75 m asl) as part of EARLINET and GALION networks. The station has contributed Raman backscatter coefficients, extinction coefficients and lidar ratios to the EARLINT database since early 2010.

Analysis of vertical profiles of the aerosol backscatter and extinction coefficient derived from regular lidar measurements from April 2010 to May 2011 and February 2012 to June 2012 was carried out. The PBL height determined for Cork showed a seasonal and monthly dependence, in agreement with other European lidar stations. The arithmetic average of the PBL height was found to be 608 ± 138 m with a median of 615 m. The PBL height was much lower than other European stations but similar studies performed at Mace Head Atmospheric Research station observed similar PBL heights in comparisons to Cork. The average AOD at 532 nm between 0 to 2 km at the Cork site was 0.158 ± 0.074 and agrees well with AOD values from Aberystwyth. An estimated total AOD at 532 nm were found to be for clean marine air masses 0.119 ± 0.023 and for polluted air masses 0.170 ± 0.036. These values agree well with total AOD measurements performed at Mace Head. Lidar ratio values at the Cork site showed a seasonal dependence, with lower values found in winter and autumn (20 ± 5 sr) and higher during spring and winter (30 ± 12 sr). Winter and autumn lidar ratio values provide a good indication of a maritime condition, while spring and summer lidar ratio values indicate more frequent aerosol loads, such as continental aerosol particles and dust particles from the Saharan desert.

Aerosol backscatter profiles measured during the eruption of the volcano Eyjafjallajökull in Iceland between 21 April and 7 May showed a strong indication of volcanic particles in the troposphere above Cork. Using forecast models and back trajectories it was possible to confirm the presence of volcanic particles. The backscatter coefficient of the ash layer was measured to be ca. 3.5 $Mm^{-1}sr^{-1}$ for 21 April, 2.5 $Mm^{-1}sr^{-1}$ for 22 April and 3.5 $Mm^{-1}sr^{-1}$ for 7 May. Estimations of the AOD at 532 nm were calculated using a lidar ratio determined from Munich lidar station. The AOD were found to be 0.122 ± 0.400, 0.090 ± 0.038 and 0.215 ± 0.080 for 21 April, 22 April and 7 May, respectively. The AOD values estimated at the Cork site agree with values measured around Europe during different stages of the eruption. AOD values between

0.15 and 0.25 were measured in Southern Italy from 20 to 22 April while values over the Iberian Peninsula from 6 to 12 May showed AOD at 440 nm varied from 0.19 to 0.31.

Analysis of backscatter and extinction coefficients during Saharan dust events showed lidar ratios that agree well with those found in literature. Using prediction models and CALIPSO measurements to confirm the presence of dust, lidar ratio of the dust layers were determine to be between 45 and 77 sr. Total AOD at 532 nm during the dust events range between 0.84 to 0.494.

References

1. Solomon, S., et al., *Climate change 2007: The physical science basis*. 2005, Taylor & Francis.
2. Tregenza, P., *The daylight factor and actual illuminance ratios.* Lighting Research and Technology, 1980. 12(2): p. 64-68.
3. Menon, S., et al., *Climate effects of black carbon aerosols in China and India.* Science, 2002. 297(5590): p. 2250-2253.
4. Goodale, M. and R. Mansfield, *Climate Forcing by Antlropogenic Aerosols.* Neuropsychologia, 1987. 25: p. 97.
5. Pilinis, C., S.N. Pandis, and J.H. Seinfeld, *Sensitivity of direct climate forcing by atmospheric aerosols to aerosol size and composition.* Journal of Geophysical Research, 1995. 100(D9): p. 18739-18,754.
6. Charlson, R.J. and J. Heintzenberg, *Aerosol forcing of climate*. 1995: Wiley Chichester.
7. Buseck, P.R. and M. Pósfai, *Airborne minerals and related aerosol particles: Effects on climate and the environment.* Proceedings of the National Academy of Sciences, 1999. 96(7): p. 3372-3379.
8. O'Dowd, C.D., et al., *Marine aerosol, sea-salt, and the marine sulphur cycle: A short review.* Atmospheric Environment, 1997. 31(1): p. 73-80.
9. Blanchard, D. and A. Woodcock, *Bubble formation and modification in the sea and its meteorological significance.* Tellus, 1957. 9(2): p. 145-158.
10. Charlson, R.J., et al., *Climate Forcing by Anthropogenic Aerosols.* Science, 1992. 255(5043): p. 423-430.
11. Haywood, J. and O. Boucher, *Estimates of the direct and indirect radiative forcing due to troposheric aerosols: A review.* Reviews of Geophysics, 2000. 38: p. 513-543.
12. Jacobson, M.Z., *Strong radiative heating due to the mixing state of black carbon in atmospheric aerosols.* Nature, 2001. 409(6821): p. 695-697.
13. Myhre, G., et al., *Estimation of the direct radiative forcing due to sulfate and soot aerosols.* Tellus B, 1998. 50(5): p. 463-477.
14. Tegen, I. and I. Fung, *Contribution to the atmospheric mineral aerosol load from land surface modification.* J. Geophys. Res., 1995. 100(D9): p. 18707-18726.

15. Tegen, I., A.A. Lacis, and I. Fung, *The influence on climate forcing of mineral aerosols from disturbed soils.* Nature, 1996. 380(6573): p. 419-422.

16. Tegen, I., et al., *Contribution of different aerosol species to the global aerosol extinction optical thickness: Estimates from model results.* Journal of Geophysical Research, 1997. 102(D20): p. 23895-23915.

17. Sokolik, I.N. and O.B. Toon, *Direct radiative forcing by anthropogenic airborne mineral aerosols.* Nature, 1996. 381(6584): p. 681-683.

18. Perry, K.D., S.S. Cliff, and M.P. Jimenez-Cruz, *Evidence for hygroscopic mineral dust particles from the Intercontinental Transport and Chemical Transformation Experiment.* J. Geophys. Res, 2004. 109: p. D23S28.

19. Weitkamp, C., *Lidar: range-resolved optical remote sensing of the atmosphere*. 2005: Springer Science+Business Media.

20. Charlson, R., et al., *Perturbation of the Northern Hemisphere radiative balance by backscattering from anthropogenic sulfate aerosols,.* Tellus Series A-dynamic Meteorology and Oceanography, 1991. 43(4): p. 152-163.

21. Rivera-Carpio, C.A., et al., *Derivation of contributions of sulfate and carbonaceous aerosols to cloud condensation nuclei from mass size distributions.* J. Geophys. Res., 1996. 101(D14): p. 19483-19493.

22. Haywood, J.M. and K.P. Shine, *The effect of anthropogenic sulfate and soot aerosol on the clear sky planetary radiation budget.* Geophys. Res. Lett., 1995. 22(5): p. 603-606.

23. Haywood, J.M., et al., *General Circulation Model Calculations of the Direct Radiative Forcing by Anthropogenic Sulfate and Fossil-Fuel Soot Aerosol.* Journal of Climate, 1997. 10(7): p. 1562-1577.

24. *EU Air Quality Standards*. 2012; Available from: http://ec.europa.eu/environment/air/quality/standards.htm.

25. Clothiaux, E.E., et al., *An Evaluation of a 94-GHz Radar for Remote Sensing of Cloud Properties.* Journal of Atmospheric and Oceanic Technology, 1995. 12(2): p. 201-229.

26. Pérez, C., et al., *A long Saharan dust event over the western Mediterranean: Lidar, Sun photometer observations, and regional dust modeling.* J. Geophys. Res., 2006. 111(D15): p. D15214.

27. Emeis, S., et al., *Atmospheric boundary-layer structure from simultaneous SODAR, RASS, and ceilometer measurements.* Atmospheric Environment, 2004. 38(2): p. 273-286.

28. *NASA's MODIS Rapid Response*. Available from: http://earthdata.nasa.gov/data/nrt-data/rapid-response.

29. Bovensmann, H., et al., *SCIAMACHY: Mission objectives and measurement modes.* Journal of the Atmospheric Sciences, 1999. 56(2): p. 127-150.

30. Gottwald, M., et al., *SCIAMACHY: Monitoring the Changing Earth's Atmosphere*. 2006: DLR, Institut für Methodik der Fernerkundung (IMF).

31. Burrows, J.P., et al., *The global ozone monitoring experiment (GOME): Mission concept and first scientific results.* Journal of the Atmospheric Sciences, 1999. 56(2): p. 151-175.

32. Eberhard, W.L., R.E. Cupp, and K.R. Healy, *Doppler Lidar Measurement of Profiles of Turbulence and Momentum Flux.* Journal of Atmospheric and Oceanic Technology, 1989. 6(5): p. 809-819.

33. Frehlich, R., *Effects of wind turbulence on coherent Doppler lidar performance.* Journal of Atmospheric and Oceanic Technology, 1997. 14(1): p. 54-75.

34. De Tomasi, F. and M.R. Perrone, *PBL and dust layer seasonal evolution by lidar and radiosounding measurements over a peninsular site.* Atmospheric Research, 2006. 80(1): p. 86-103.

35. Schaap, M., et al., *Exploring the relation between aerosol optical depth and PM2. 5 at Cabauw, the Netherlands.* Atmos. Chem. Phys, 2009. 9: p. 909-925.

36. Rodríguez, S., et al., *Saharan dust contributions to PM10 and TSP levels in Southern and Eastern Spain.* Atmospheric Environment, 2001. 35(14): p. 2433-2447.

37. Querol, X., et al., *African dust contributions to mean ambient PM10 mass-levels across the Mediterranean Basin.* Atmospheric Environment, 2009. 43(28): p. 4266-4277.

38. Ancellet, G., et al., *Ground-based lidar studies of ozone exchanges between the stratosphere and the troposphere.* Journal of Geophysical Research, 1991. 96(22): p. 401-22.

39. Whiteman, D., et al., *Raman lidar measurements of water vapor and cirrus clouds during the passage of hurricane Bonnie.* Journal of Geophysical Research, 2001. 106: p. 5211-5225.

40. McAuliffe, M.A.P. and A.A. Ruth, *Typical tropospheric aerosol backscatter profiles for Southern Ireland: The Cork Raman lidar.* Atmospheric Research, 2013. 120-121(0): p. 334-342.

41. Matthais, V., et al., *Aerosol Lidar Intercomparison in the Framework of the EARLINET Project. 1. Instruments.* Appl. Opt., 2004. 43(4): p. 961-976.

42. Böckmann, C., et al., *Aerosol Lidar Intercomparison in the Framework of the EARLINET Project. 2. Aerosol Backscatter Algorithms.* Appl. Opt., 2004. 43(4): p. 977-989.

43. Pappalardo, G., et al., *Aerosol Lidar Intercomparison in the Framework of the EARLINET Project. 3. Raman Lidar Algorithm for Aerosol Extinction, Backscatter, and Lidar Ratio.* Appl. Opt., 2004. 43(28): p. 5370-5385.

44. Pappalardo, G., et al., *Four-dimensional distribution of the 2010 Eyjafjallajökull volcanic cloud over Europe observed by EARLINET.* Atmos. Chem. Phys. Discuss., 2012. 12(11): p. 30203-30257.

45. Kovalev, V.A. and W.E. Eichinger, *Elastic Lidar: Theory, Practice, and Analysis Methods*. 2004: John Wiley & Sons.

46. Ansmann, A., M. Riebesell, and C. Weitkamp, *Measurement of atmospheric aerosol extinction profiles with a Raman lidar.* Opt. Lett., 1990. 15(13): p. 746-748.

47. Browell, E.V., T.D. Wilkerson, and T.J. McIlrath, *Water vapor differential absorption lidar development and evaluation.* Appl. Opt., 1979. 18(20): p. 3474-3483.

48. Bowman, M.R., A.J. Gibson, and M.C.W. Sandford, *Atmospheric Sodium measured by a Tuned Laser Radar.* Nature, 1969. 221(5179): p. 456-457.

49. Marseille, G. and A. Stoffelen, *Simulation of wind profiles from a space-borne Doppler wind lidar.* Quarterly Journal of the Royal Meteorological Society, 2003. 129(594): p. 3079-3098.

50. Menzies, R.T. and R.M. Hardesty, *Coherent Doppler lidar for measurements of wind fields.* Proceedings of the IEEE, 1989. 77(3): p. 449-462.

51. Gentry, B.M., H. Chen, and S.X. Li, *Wind measurements with 355-nm molecular Doppler lidar.* Opt. Lett., 2000. 25(17): p. 1231-1233.

52. Flesia, C. and C.L. Korb, *Theory of the Double-Edge Molecular Technique for Doppler Lidar Wind Measurement.* Appl. Opt., 1999. 38(3): p. 432-440.

53. Frehlich, R., S.M. Hannon, and S.W. Henderson, *Coherent Doppler Lidar Measurements of Wind Field Statistics.* Boundary-Layer Meteorology, 1998. 86(2): p. 233-256.

54. Measures, R.M., *Laser remote sensing: fundamentals and applications*. 1984: Wiley.

55. Collis, R. and P. Russell, *Lidar measurement of particles and gases by elastic backscattering and differential absorption.* Laser monitoring of the atmosphere, 1976: p. 71-151.

56. Killinger, D.K. and A. Mooradian, *Optical and laser remote sensing.* Berlin, Springer-Verlag(Springer Series in Optical Sciences., 1983. 39.

57. Bösenberg, J., *Ground-Based Differential Absorption Lidar for Water-Vapor and Temperature Profiling: Methodology.* Appl. Opt., 1998. 37(18): p. 3845-3860.

58. Fiocco, G. and G. Grams, *Observations of the upper atmosphere by optical radar in Alaska and Sweden during the summer 1964.* Tellus, 1966. 18(1): p. 34-38.

59. Murayama, T., et al., *Ground-based network observation of Asian dust events of April 1998 in east Asia.* Journal of Geophysical Research, 2001. 106(D16): p. 18345-18360.

60. Poole, L.R. and M.P. McCormick, *Airborne lidar observations of Arctic polar stratospheric clouds: Indications of two distinct growth stages.* Geophys. Res. Lett., 1988. 15(1): p. 21-23.

61. Winker, D.M., et al., *Overview of the CALIPSO Mission and CALIOP Data Processing Algorithms.* Journal of Atmospheric and Oceanic Technology, 2009. 26(11): p. 2310-2323.

62. Liu, Z., et al., *CALIOP Algorithm Theoretical Basis Document, Part 3: Scene Classification Algorithms*. 2005. p. 56.

63. Young, S.A. and M.A. Vaughan, *The Retrieval of Profiles of Particulate Extinction from Cloud-Aerosol Lidar Infrared Pathfinder Satellite Observations (CALIPSO) Data: Algorithm Description.* Journal of Atmospheric and Oceanic Technology, 2009. 26(6): p. 1105-1119.

64. Mattis, I., et al., *EARLINET correlative measurements for CALIPSO.* 2007: p. 67500Z-67500Z.

65. Pappalardo, G., *EARLINET correlative measurements for CALIPSO: First intercomparison results.* J. Geophys. Res, 2010. 115(10.1029).

66. Giunta, A., et al., *Long-term aerosol and cloud database from correlative EARLINET-CALIPSO observations*, in *25th International Laser Radar Conference*. 2010: St. Petersburg. p. 1241-1244.

67. Holben, B.N., et al., *AERONET—A Federated Instrument Network and Data Archive for Aerosol Characterization.* Remote Sensing of Environment, 1998. 66(1): p. 1-16.

68. Ansmann, A., et al., *The 16 April 2010 major volcanic ash plume over central Europe: EARLINET lidar and AERONET photometer observations at Leipzig and Munich, Germany.* Geophys. Res. Lett., 2010. 37(13): p. L13810.

69. Ansmann, A., et al., *Ash and fine-mode particle mass profiles from EARLINET-AERONET observations over central Europe after the eruptions of the Eyjafjallajökull volcano in 2010.* J. Geophys. Res., 2011. 116: p. D00U02.

70. Müller, D., et al., *Saharan dust over a central European EARLINET-AERONET site: Combined observations with Raman lidar and Sun photometer.* J. Geophys. Res., 2003. 108(D12): p. 4345.

71. Müller, G., et al. (2011) *WMO Global Atmosphere Watch (GAW) Addendum for the Period 2012 - 2015 to the WMO Global Atmosphere Watch (GAW) Strategic Plan 2008 - 2015*. 57.

72. Banwell, C.N. and E.M. McCash, *Fundamentals of molecular spectroscopy*. 1995: McGraw-Hill.

73. Sneep, M. and W. Ubachs, *Direct measurement of the Rayleigh scattering cross section in various gases.* Journal of Quantitative Spectroscopy and Radiative Transfer, 2005. 92(3): p. 293-310.

74. She, C.Y., *Spectral structure of laser light scattering revisited: bandwidths of nonresonant scattering lidars.* Applied Optics, 2001. 40(27): p. 4875-4884.

75. Leonard, D.A., *Observation of Raman Scattering from the Atmosphere using a Pulsed Nitrogen Ultraviolet Laser.* Nature, 1967. 216(5111): p. 142-143.

76. Cooney, J.A., *Measurement of Atmospheric Temperature Profiles by Raman Backscatter.* Journal of Applied Meteorology, 1972. 11: p. 108-112.

77. Melfi, S.H., *Remote Measurements of the Atmosphere Using Raman Scattering.* Appl. Opt., 1972. 11(7): p. 1605-1610.

78. Inaba, H., *Detection of atoms and molecules by Raman scattering and resonance fluorescence*, in *Laser Monitoring of the Atmosphere*, E.D. Hinkley, Editor. 1976, Springer Berlin Heidelberg. p. 153-236.

79. Hollas, J.M., *Modern Spectroscopy*. 2004: Wiley.

80. Long, D.A., *The Raman Effect: A Unified Treatment of the Theory of Raman Scattering by Molecules*. 2002: John Wiley & Sons.

81. Bucholtz, A., *Rayleigh-scattering calculations for the terrestrial atmosphere.* Appl. Opt., 1995. 34(15): p. 2765-2773.

82. Klett, J.D., *Stable analytical inversion solution for processing lidar returns.* Appl. Opt., 1981. 20(2): p. 211-220.

83. Fernald, F.G., *Analysis of atmospheric lidar observations: some comments.* Appl. Opt., 1984. 23(5): p. 652-653.

84. Sasano, Y., E.V. Browell, and S. Ismail, *Error caused by using a constant extinction/backscattering ratio in the lidar solution.* Appl. Opt., 1985. 24(22): p. 3929-3932.

85. Wandinger, U. and A. Ansmann, *Experimental Determination of the Lidar Overlap Profile with Raman Lidar.* Appl. Opt., 2002. 41(3): p. 511-514.

86. McAuliffe, M.A.P., *Implementation of a backscatter and Raman LIDAR station for studying the vertical aerosol distribution over Southern Ireland*, in *Department of Physics*. 2008, University College of Cork: Cork. p. 119.

87. Cash, W.C., *IRT (interactive ray trace)*. 1994, Opensource: Colorado p. Raytracing program.

88. Freudenthaler, V. *The telecover test: A quality assurance tool for the optical part of a lidar system*. in *24th ILRC*. 2008. Boulder, Colorado, USA.

89. White, J.M., et al., *Importance of Using Observations of Mixing Depths in order to Avoid Large Prediction Errors by a Transport and Dispersion Model.* Journal of Atmospheric and Oceanic Technology, 2009. 26(1): p. 22-32.

90. Matthias, V., et al., *Vertical aerosol distribution over Europe: Statistical analysis of Raman lidar data from 10 European Aerosol Research Lidar Network (EARLINET) stations.* J. Geophys. Res., 2004. 109(D18): p. D18201.

91. Norton, E.G., et al., *Boundary layer structure and decoupling from synoptic scale flow during NAMBLEX.* Atmos. Chem. Phys., 2006. 6(2): p. 433-445.

92. Kunz, G.J., et al., *Lidar observations of atmospheric boundary layer structure and sea spray aerosol plumes generation and transport at Mace Head, Ireland (PARFORCE experiment).* J. Geophys. Res., 2002. 107(D19): p. 8106.

93. Pappalardo, G., et al., *EARLINET coordinated lidar observations of Saharan dust events on continental scale.* IOP Conference Series: Earth and Environmental Science, 2009. 7(1): p. 012002.

94. *Met Éireann*. Available from: http://www.met.ie.

95. Mulcahy, J.P., C.D. O'Dowd, and S.G. Jennings, *Aerosol optical depth in clean marine and continental northeast Atlantic air.* J. Geophys. Res., 2009. 114(D20): p. D20204.

96. Smirnov, A., et al., *Optical properties of atmospheric aerosol in maritime environments.* Journal of the Atmospheric Sciences, 2002. 59(3): p. 501-523.

97. Amiridis, V., et al., *Four-year aerosol observations with a Raman lidar at Thessaloniki, Greece, in the framework of European Aerosol Research Lidar Network (EARLINET).* J. Geophys. Res., 2005. 110(D21): p. D21203.

98. Matthias, V. and J. Bösenberg, *Aerosol climatology for the planetary boundary layer derived from regular lidar measurements.* Atmospheric Research, 2002. 63(3–4): p. 221-245.

99. Müller, D., et al., *Aerosol-type-dependent lidar ratios observed with Raman lidar.* J. Geophys. Res., 2007. 112(D16): p. D16202.

100. Wandinger, U., et al., *Air mass modification over Europe: EARLINET aerosol observations from Wales to Belarus.* J. Geophys. Res., 2004. 109(D24): p. D24205.

101. Sigmundsson, F., et al., *Intrusion triggering of the 2010 Eyjafjallajokull explosive eruption.* Nature, 2010. 468(7322): p. 426-430.

102. Rawluk, Z. and S. Mathur, *The Cause and Effect of the 2010 Eyjafjallajokull Eruption.* GLG216 Journal, 2011: p. 70.

103. Gislason, S., et al., *Characterization of Eyjafjallajökull volcanic ash particles and a protocol for rapid risk assessment.* Proceedings of the National Academy of Sciences, 2011. 108(18): p. 7307-7312.

104. Shapiro, M.A. and D.A. Keyser, *Fronts, jet streams, and the tropopause*. 1990: US Department of Commerce, National Oceanic and Atmospheric Administration, Environmental Research Laboratories, Wave Propagation Laboratory.

105. Gislason, S.R., et al., *Volcanic ash from the 2010 Eyjafjallajökull eruption.* Applied Geochemistry, 2011. 26, Supplement(0): p. S188-S190.

106. Schumann, U., et al., *Airborne observations of the Eyjafjalla volcano ash cloud over Europe during air space closure in April and May 2010.* Atmos. Chem. Phys., 2011. 11(5): p. 2245-2279.

107. Dacre, H.F., et al., *Evaluating the structure and magnitude of the ash plume during the initial phase of the 2010 Eyjafjallajökull eruption using lidar observations and NAME simulations.* J. Geophys. Res., 2011. 116: p. D00U03.

108. Campanelli, M., et al., *Monitoring of Eyjafjallajökull volcanic aerosol by the new European Skynet Radiometers (ESR) network.* Atmospheric Environment, 2012. 48(0): p. 33-45.

109. Matthias, V., et al., *The ash dispersion over Europe during the Eyjafjallajökull eruption – Comparison of CMAQ simulations to remote sensing and air-borne in-situ observations.* Atmospheric Environment, 2012. 48(0): p. 184-194.

110. Hervo, M., et al., *Physical and optical properties of 2010 Eyjafjallajökull volcanic eruption aerosol: ground-based, Lidar and airborne measurements in France.* Atmos. Chem. Phys., 2012. 12(4): p. 1721-1736.

111. Markowicz, K.M., et al., *Remote sensing measurements of the volcanic ash plume over Poland in April 2010.* Atmospheric Environment, 2012. 48(0): p. 66-75.

112. Bukowiecki, N., et al., *Ground-based and airborne in-situ measurements of the Eyjafjallajökull volcanic aerosol plume in Switzerland in spring 2010.* Atmos. Chem. Phys., 2011. 11(19): p. 10011-10030.

113. Mona, L., et al., *Multi-wavelength Raman lidar observations of the Eyjafjallajökull volcanic cloud over Potenza, southern Italy.* Atmos. Chem. Phys., 2012. 12(4): p. 2229-2244.

114. Lettino, A., et al., *Eyjafjallajökull volcanic ash in southern Italy.* Atmospheric Environment, 2012. 48(0): p. 97-103.

115. Toledano, C., et al., *Aerosol properties of the Eyjafjallajökull ash derived from sun photometer and satellite observations over the Iberian Peninsula.* Atmospheric Environment, 2012. 48(0): p. 22-32.

116. Papayannis, A., et al., *Optical properties and vertical extension of aged ash layers over the Eastern Mediterranean as observed by Raman lidars during the Eyjafjallajökull eruption in May 2010.* Atmospheric Environment, 2012. 48(0): p. 56-65.

117. Draxler, R.R. and G.D. Hess (1997) *Description of the HYSPLIT_4 modeling system.* NOAA Tech. Memo. ERL ARL-224, 24.

118. Jones, A., et al., *The U.K. Met Office's Next-Generation Atmospheric Dispersion Model, NAME III Air Pollution Modeling and Its Application XVII*, C. Borrego and A.-L. Norman, Editors. 2007, Springer US. p. 580-589.

119. Davies, T., et al., *A new dynamical core for the Met Office's global and regional modelling of the atmosphere.* Quarterly Journal of the Royal Meteorological Society, 2005. 131(608): p. 1759-1782.

120. Bösenberg, J. and V. Matthias, *EARLINET: A European Aerosol Research Lidar Network to Establish an Aerosol Climatology*. Report - Max-Planck-Institut fur Meteorologie, 2003. 348(1-191).

121. *Volcanic Ash Advisory Centres*. Available from: http://www.metoffice.gov.uk/aviation/vaac/.

122. Rolf, C., et al., *Lidar observation and model simulation of a volcanic-ash-induced cirrus cloud during the Eyjafjallajökull eruption.* Atmos. Chem. Phys. Discuss., 2012. 12(6): p. 15675-15707.

123. Flentje, H., et al., *The Eyjafjallajoekull eruption in April 2010- detection of volcanic plume using in-situ measurements, ozone sondes and lidar-ceilometer profiles.* Atmospheric Chemistry and Physics, 2010. 10(20): p. 10085-10092.

124. Perrone, M.R., et al., *Characterization of Eyjafjallajökull volcanic aerosols over Southeastern Italy.* Atmos. Chem. Phys. Discuss., 2012. 12(6): p. 15301-15335.

125. Marenco, F., et al., *Airborne lidar observations of the 2010 Eyjafjallajökull volcanic ash plume.* Journal of Geophysical Research, 2011. 116(null): p. D00U05.

126. Sicard, M., et al., *Monitoring of the Eyjafjallajökull volcanic aerosol plume over the Iberian Peninsula by means of four EARLINET lidar stations.* Atmos. Chem. Phys, 2012. 12: p. 3115-3130.

127. Winker, D., et al., *CALIOP observations of the transport of ash from the Eyjafjallajökull volcano in April 2010.* Journal of Geophysical Research, 2012. 117(null): p. D00U15.

128. Nickovic, S., et al., *A model for prediction of desert dust cycle in the atmosphere.* J. Geophys. Res., 2001. 106(D16): p. 18113-18129.

129. Maciszewska, A., K. Markowicz, and M. Witek, *A multiyear analysis of aerosol optical thickness over Europe and Central Poland using NAAPS model simulation.* Acta Geophysica, 2010. 58(6): p. 1147-1163.

130. Hogan, T.F. and T.E. Rosmond, *The Description of the Navy Operational Global Atmospheric Prediction System's Spectral Forecast Model.* Monthly Weather Review, 1991. 119(8): p. 1786-1815.

131. *NAAPS/NRL (Naval Research Laboratory)* Available from: http://www.nrlmry.navy.mil/aerosol/#currentaerosolmodeling

132. *BSC-DREAM8b (Dust REgional Atmospheric Model) model*. Available from: http://www.bsc.es/projects/earthscience/BSC-DREAM/.

133. Papayannis, A., et al., *Systematic lidar observations of Saharan dust over Europe in the frame of EARLINET (2000–2002).* Journal of Geophysical Research, 2008. 113(D10).

134. Masonis, S.J., et al., *A Study of the Extinction-to-Backscatter Ratio of Marine Aerosol during the Shoreline Environment Aerosol Study*.* Journal of Atmospheric and Oceanic Technology, 2003. 20(10): p. 1388-1402.

135. *Atmospheric Science Data Center: CALIPSO Data and Information*. Available from: http://eosweb.larc.nasa.gov/PRODOCS/calipso/table_calipso.html

136. Pisani, G., et al., *Characterization of Saharan dust layers over Naples (Italy) during 2000–2003 EARLINET project.* Atmospheric Research, 2011. 102(3): p. 286-299.

137. Dubovik, O., et al., *Application of spheroid models to account for aerosol particle nonsphericity in remote sensing of desert dust.* J. Geophys. Res., 2006. 111(D11): p. D11208.

138. Mattis, I., et al., *Dual-wavelength Raman lidar observations of the extinction-to-backscatter ratio of Saharan dust.* Geophys. Res. Lett., 2002. 29(9): p. 1306.

139. Ferrare, R.A., et al., *Raman lidar measurements of the aerosol extinction-to-backscatter ratio over the Southern Great Plains.* J. Geophys. Res., 2001. 106(D17): p. 20333-20347.

140. Mishchenko, M.I., et al., *Modeling phase functions for dustlike tropospheric aerosols using a shape mixture of randomly oriented polydisperse spheroids.* J. Geophys. Res., 1997. 102(D14): p. 16831-16847.

141. Barnaba, F. and G.P. Gobbi, *Lidar estimation of tropospheric aerosol extinction, surface area and volume: Maritime and desert-dust cases.* J. Geophys. Res., 2001. 106(D3): p. 3005-3018.

142. Di Girolamo, P., et al., *Raman lidar observations of a Saharan dust outbreak event: Characterization of the dust optical properties and determination of particle size and microphysical parameters.* Atmospheric Environment, 2012. 50(0): p. 66-78.